Chemical Solution Deposition of Oxide Buffer and Superconducting Layers for $YBa_2Cu_3O_7$ Coated Conductors

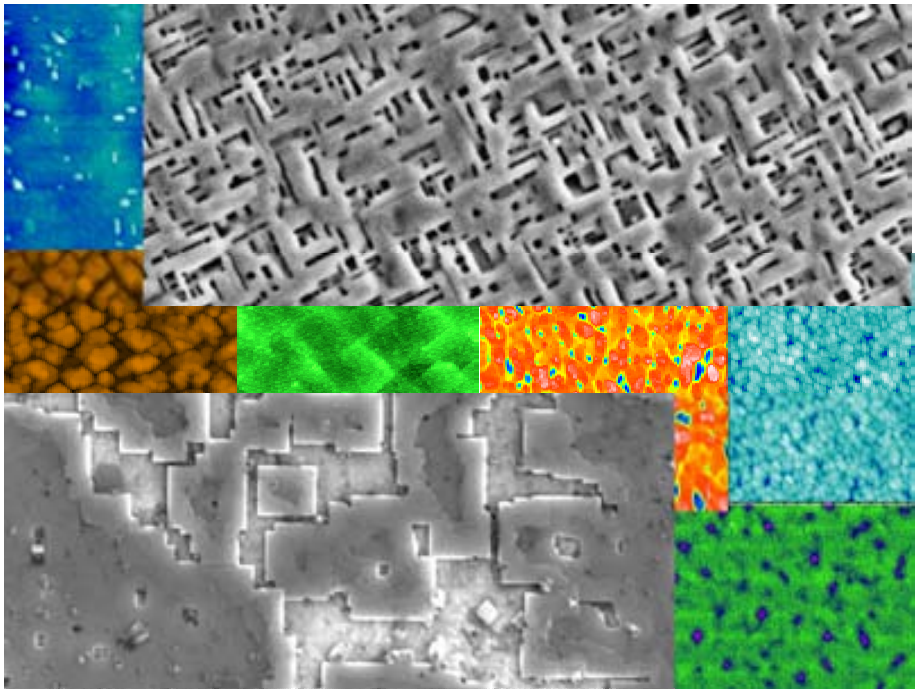

Mariona Coll Bau

2006

Chemical Solution Deposition of Oxide Buffer and Superconducting Layers for $YBa_2Cu_3O_{7-\delta}$ Coated Conductors

Mariona Coll Bau

Programa de doctorat en Ciència de Materials
Department de química de la Universitat Autònoma de Barcelona

Departament de Materials Magnètics i Superconductors
ICMAB-CSIC

Director: Prof. Xavier Obradors
Co-director: Dr. Teresa Puig
Tutor: Dr. Jaume Casabó

Memoria presentada per a l'obtenció del grau de doctor

Bellaterra, 2 de Novembre de 2006

Acknowledgments

The work described in this thesis would not have been possible without the help, knowledge and friendship of several people.

First, I would like to address a special thanks to my supervisors, Prof. Xavier Obradors and Dr. Teresa Puig for all the opportunities they have given to me, their helpful advises and for the time and trust they invested in me.

To Dr. J.M. Moretó and Dr. Susagna Ricart who introduced me to metalorganic chemistry, for the numerous discussions we had and the advises they gave to me.

To Dr. R. Feenstra, for his kind help, for the very creative scientific discussions we had during my short stay in Oak Ridge National Laboratory and for the samples he provided to me.

To Prof. A.R-González-Elipe and Dr. J.P. Espinós for all the time they dedicated to me when I was in the ICMSE. I also want to thank Dr.J.P.Espinós for his encouragement, helpfulness and for the XPS knowledge he sheared with me.

A valuable and beneficial collaboration with Dr.B.Holpzafel and Dr.R.Hühne from IFW Dresden provided the RHEED patterns and the PLD samples.

I am also grateful to ZFW-Gottingen, European High Temperature Superconductors (EHTS) Cryoelectra and Nexans SuperConductors GmbH (NSC)for providing metallic substrates.

To “Ministerio de Educación y Ciencia” for FPU fellowship.

To EU projects SOLSULET, SUPER3C and HIPERCHEM, to the Spanish Ministery (CICITY MAT02-02642 and MAT03-01584) and to the Generalitat de Catalunya (2001-SGR-00336 and CeRMAE) for the financial support.

Particular thanks must be given to those who provided invaluable technical assistance and bringing a level of expertise to particular area of the work that I could never have hoped to match in the available time. Dr.A. Pérez who provided the excellent AFM images of the samples, J.M. Pérez and J.Gutiérrez for uncountable inductive J_c measurements, J.Oró and A.M. Bea for TGA measurements, J.C. González for micro-Raman measurements, N.Romà for viscosity measurements, Dr. A.Pomar for electrical resistivity measurements, J. Bassas for all the time they dedicated to me for XRD texture analysis, J.Gàzquez for TEM images as well as numerous XRD measurements, to Serveis de Microscòpia Electrònica, UAB and UB, for the use of SEM-EDX and TEM facilities.

I would like to express my appreciation to people from computing and workshop and sustenance teams for disposition to help me at any time.

Particular thanks must be given to Llibertat for the pleasant and supportive working environment

I would also like to address a heartfelt thanks to people from ICMSE for the exceptional welcome they gave me, for every discussion we had and the time we spent together in Sevilla. Specially Ana, Carmen, Ángel, Katina, Vanda, Victors, Jose, Diego and Marcela.

I would like to thank people both past and present in the Superconductivity Group that made my work easier and pleasant.

Special thanks go to friends and family, for their unconditional and continuous support throughout the last four years. Last but not least, to Jaume for his ‘take it easy Mariona’.

Motivation

Since the discovery of high-temperature superconductivity (HTS) in cuprate materials, substantial efforts have focused on developing a high-current superconducting wire technology to fully exploit their fundamental current-carrying capability. $YBa_2Cu_3O_7$ (YBCO) is the most promising material for HTS wires (second-generation coated conductors) because it has a very high potential to carry high currents at high magnetic fields operated with liquid nitrogen cryogenics (65-77K).

One crucial requirement for the preparation of YBCO coated conductors with high critical current densities is the elimination of weak links between YBCO grains. Weak links in the high temperature superconductors are produced by grain boundaries that lead to a weak coupling between the superconducting grains and consequently to a reduction in the critical current density. Thus, the key is to prepare a textured substrate adequately buffered with oxide layers which transmit, totally or partially, the underneath structure to the superconducting layer. Presently, there are two main techniques for textured template fabrication: Rolling Assisted Biaxially Textured Substrates (*RABiTS*) and Ion Beam Assisted Deposition (*IBAD*). Among the various process used to prepare YBCO and buffer layers films, metalorganic decomposition (MOD) has recently emerged as a very competitive approach to cost-effective manufacturing process that allow to easily control precursor chemistry maintaining high electrical performance in the superconducting layer. In particular, in 2001 the Superconductivity group at ICMAB, starting from scratch, took the challenge to produce all-chemical solution deposited (CSD) YBCO coated conductors with high critical current density in the scope of an European Project called SOLSULET.

The aim of this Thesis, performed halfway between SOLSULET and a more recent European Project called HIPERCHEM, is to fabricate all-chemical YBCO multilayered system, using trifluoroacetates (TFA) precurors for YBCO, with high critical current density to be further transferred on metallic substrates. It requires a tight control of the interface quality in the multilayered architecture, i.e. between a substrate, one or several buffer layers and the superconducting layer itself. Although the film and the substrate have similar structure, the film can undergo a temperature-induced morphological instability due to the interfacial strain associated to the lattice parameter misfit. Simple analysis of surface free energy for YBCO films on different substrates have allowed to predict the equilibrium conditions to avoid dewetting of YBCO thin films.

The optimum oxide buffer combination depends on the nature of the metallic substrate. In the present work the search for YBCO buffer layers has centered on $SrTiO_3$ with perovskite and CeO_2 with fluorite structure since they have been successfully used in the literature by vacuum techniques as the first approach to medium cost coated conductors. To obtain high quality TFA-YBCO films on those buffer layers it is required a good knowledge of the multilayer growth conditions of these oxides based on CSD, to optimize the underlying cap layer quality and to determine the parameters that influence the subsequent YBCO final texture and superconducting properties.

This Thesis is divided into nine chapters. The properties of high temperature superconductors and especially of YBCO are reviewed in chapter 1, including an overview of the chemical solution deposition route and a brief summary of the TFA-YBCO process. In Chapter 2 the experimental techniques used for the structural, microstructural, morphological, chemical characterization of superconducting and buffer layers are presented. Superconducting and electrical resistivity measurements for YBCO films are also described. The experimental description with the different steps and parameters that are required for the preparation of YBCO films by trifluoroacetate route (TFA), as well as the preparation of $SrTiO_3$, $BaZrO_3$ and CeO_2 buffer layers by metalorganic decomposition are described in Chapter 3. Chapter 4 contains the study of the spontaneous generation of strain-induced surface structures in TFA-YBCO films epitaxially grown on different types of single crystals ($LaAlO_3$, $SrTiO_3$) or oxide buffer layers with modified lattice mismatch values ($BaZrO_3$).

Chapter 5 describes the influence of perovskite multibuffered architecture quality ($SrTiO_3$ and $BaZrO_3$) on the epitaxial growth of TFA-YBCO film.

In chapter 6 we analyse the influence of processing atmosphere on CeO_2 film morphology, chemistry and texture when deposited by sputtering on YSZ single crystal. We have described the optimal CeO_2 surface morphology for subsequent TFA-YBCO growth. Most favourable conditions are then applied to CeO_2 deposited on YSZ/Ni and on YSZ/SS substrate. Finally buffer layer quality is correlated with YBCO critical current density.

In chapter 7 we present a complete analysis of CeO_2 and doped-CeO_2 buffer layer fabricated by the MOD route on YSZ single crystal as a model system. Analysing morphology, texture, microstructure and chemistry of undoped and doped MOD-CeO_2 films we have identified the optimal conditions to obtain highly textured CeO_2 films. Results are discussed in terms of atomic mobility in MOD-CeO_2 films. We establish a correlation between CeO_2 properties (morphological, structural) and quality of TFA-YBCO film.

PLD-YBCO film quality on MOD-CeO_2 and doped-CeO_2 films is described in chapter 8. We compare PLD-YBCO films with optimized TFA-YBCO films on doped-CeO_2 films, analysing in particular the quality of cap layer and the role of interface reaction between YBCO and CeO_2 on the final superconducting film quality. Furthermore we carry out an optimization of TFA-YBCO growth parameters. Finally in chapter 9 general conclusions are drawn.

CHAPTER 1

Introduction

1.1 High temperature superconductivity: $YBa_2Cu_3O_{7-\delta}$

Superconductivity is a phenomenon displayed by some materials when they are cooled below a transition temperature, T_c, known as critical temperature. Below T_c, superconducting materials exhibit two characteristic properties: (1) lose of the electric resistance and (2) expulsion of the applied magnetic field (the Meissner effect) [1].

After the discovery of superconductivity in mercury at 4K by Kamerling Onnes in 1911 the search for new superconducting materials led to a linear increase of T_c with time over decades, reaching a plateau at 23K with the discovery of the superconductivity of Nb_3Ge by Gavaler [2]. These superconducting materials, considering its T_c, are named superconductors of low critical temperature (LTSC). The theory developed by J.Bardeen, L.Cooper and J.Schrieffer (BCS) has been very successful in describing LTSC, assuming that electrons are coupled via electron-phonon interaction to form Cooper pairs [3,1]. After 13 more years, the path to radically higher transition temperatures started by the discovery in 1986 of superconductivity at 35K in a mixed valence oxide of lanthanum, barium and copper by Bednorz and Müller [4], a high temperature superconductor (HTSC).

Another big jump to T_c ~90K followed quickly, with the discovery of the '123' class of materials, exemplified by $YBa_2Cu_3O_7$ (YBCO) [5]. This new superconductor, being the first material with a critical temperature above liquid nitrogen temperature, drastically reduced the cost of cryogenics involved, making feasible its technological application. Subsequently several compounds with T_c above 92K were found, $Bi_2Sr_2Ca_2Cu_3O_{10}$ (120K) [6], $Tl_2Ba_2Ca_2Cu_3O_{10}$ (127K) and $HgBa_2Ca_1Cu_2O_8$ (134 K) [7]. In HTSC, in contrast to LTSC, the phenomenon of superconductivity could not be explained by conventionally BCS theory. Different theories have been proposed but this is still an open issue.

The discovery of high temperature superconducting materials brought great promise and optimism for their rapid usage in technological applications, but significant market penetration of HTSC devices requires HTSC wires that fully exploit their fundamental current-carrying capability. Currently, industry and the scientific community are working in close cooperation to improve and develop techniques for the production of high quality YBCO tapes and their implementation in power application devices (transmission cables, motors, generators, transformers and fault current limiters) where high magnetic fields are present.

1.1.1 Structural properties of $YBa_2Cu_3O_7$

HTSC have a perovskite structure with Cu-O planes lying normal to the crystallographic c-direction. This is a common feature of these materials, therefore they are often referred to as cuprates. One of the most actively studied HTSC materials is YBCO. It is widely utilized in various fields of research because it has a very high potential to carry high currents in high magnetic fields operating at liquid nitrogen temperature (65-77K).

Fig. 1-1 shows a sketch of the unit cell of YBCO structure. The Cu-O planes are separated by charge-reservoir interleaved layers allowing a change in the carrier density available in the Cu-O planes. For YBCO, these interleaved layers contain CuO chains in the b direction which contain free carriers and contribute to the normal conductivity. Therefore, the current that can flow parallel to Cu-O plains (a-b planes) is much higher than the current flowing through the c axis. So that, current has to flow through the a-b plane direction in order to get the maximum critical current density. The critical current density, J_c, is then defined by the maximum current that these materials can carry without dissipation, above this value they stop being superconductors.

In fact, all cuprates have this anisotropic layered structure which place fundamental restrictions on their properties especially in polycrystalline form. In particular, for superconducting films the *c* axis has to be oriented perpendicular to the substrate, so that high currents can be applied along the a-b planes.

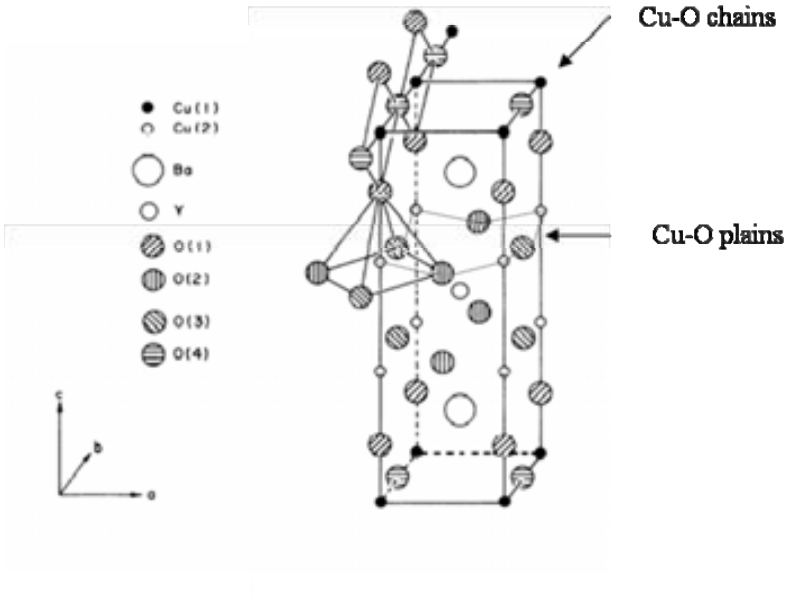

Fig. 1-1 Crystallographic structure of $YBa_2Cu_3O_{7-\delta}$ [8]. Representative lattice parameters for the orthorhombic phase of $YBa_2Cu_3O_7$ are *a*=3.827 Å, *b*=3.882 Å and *c*=11.682 Å

Essentially, YBCO consists of three perovskite units $BaCuO_3$, $YCuO_2$, and CuO_2 which stack vertically forming the superconducting unit cell with some oxygen atoms missing. Indeed, the oxygen content will determine its crystallographic structure and the mobile charge carrier concentration in the Cu-O planes. Considering $YBa_2Cu_3O_x$ notation, for an oxygen content x=6 the compound is in the tetragonal phase and it is an insulator. Increasing the oxygen content up to x=6.6, the compound undergoes a phase transition from tetragonal to orthorhombic being only superconducting in the latter. Finally, raising x to 6.94, T_c approaches its maximum value (91K). Above x=6.94 the compound is overdoped and T_c drops (see Fig. 1-2).

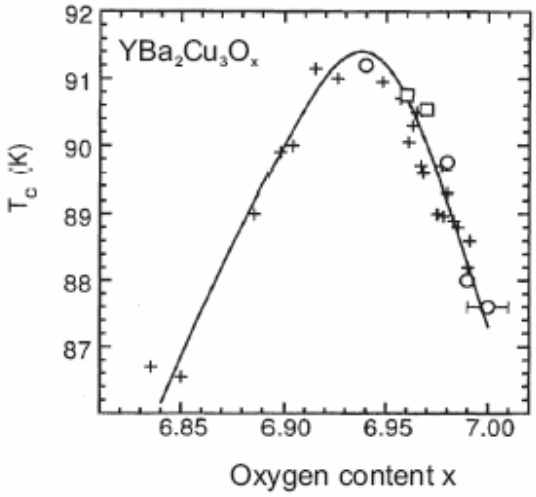

Fig. 1-2 Variation of T_c with oxygen content for $YBa_2Cu_3O_x$ [9].

1.1.2 Physical properties of $YBa_2Cu_3O_{7-\delta}$

YBCO is classified as type II superconductor [1]. It is characterized by its gradual transition from the superconducting to normal state. In comparison to the sharp transition of a Type-I superconductor, Fig. 1-3(a), a type II superconductor has two critical magnetic fields. Above the lower critical magnetic field, $H_{c1}(T)$, the magnetic flux from external field is no longer completely expelled, and the superconductor exists in a mixed state. Above the higher critical magnetic field, H_{c2} (T), the superconductivity is completely destroyed, and the material exists in a normal state, see Fig. 1-3 (b).

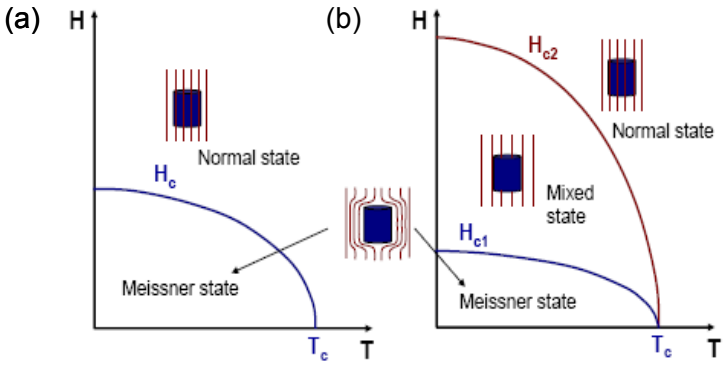

Fig. 1-3 Magnetic phase diagram for a type I (a) and type II (b) superconductors

YBCO is capable of carrying bulk super current at high fields which can exceed of 100T (H_{c2}). However, applications are limited by a lower characteristic field, the irreversibility field, H*(T), at which critical current density (J_c) vanishes. Fig. 1-4 presents the magnetic field-temperature (H-T) phase diagram for the three actual (Nb-Ti, Nb_3Sn and $Bi_2Ca_2Cu_2O_3$ (Bi-2223)) and two potential (YBCO and MgB_2) conductor materials. Their different phase diagrams result from their distinctly different physical parameters and crystal structures, in short, their anisotropy. Anisotropy, described by the parameter γ, has values of 1 for Nb-Ti, 7 for YBCO and 50-200 for Bi-2223[10].

Strongly anisotropic Bi-2223 exhibits an enormous suppression of H*(77K) to the very low value of 0.2T. This irreversibility field prevents use of Bi-2223 at 77K, although at low temperature are possible, and proves one of the key arguments for developing a second generation HTSC technology based on YBCO, for which H*(77K) ~7T.

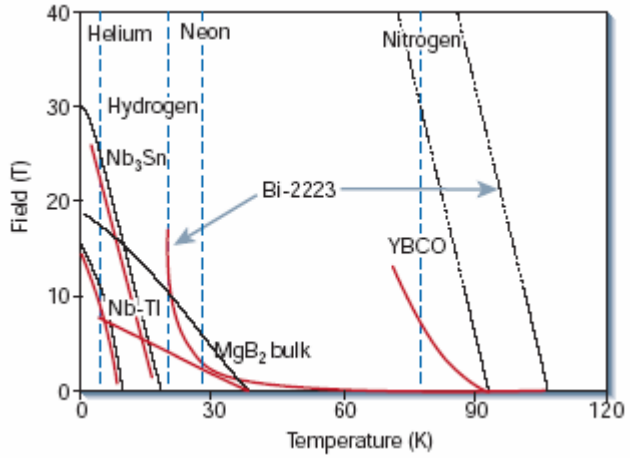

Fig. 1-4 Magnetic field-temperature diagram for several type II superconductors. The upper critical field at which bulk superconductivity is destroyed is indicated in black, while the irreversibility field H* at which the bulk critical current density goes to zero is indicated in red. [11]

1.2 Coated conductors: a developing application of high temperature superconductivity

Today there are two basic architectures for HTS wires, a multifilamentary or first generation conductor (1G) [13] and a coated conductor (CC) or second-generation conductor (2G) [14,15], see Fig. 1-5. Each type of advanced wires achieves high power density with minimal electrical resistance, but differs in the superconductor materials that make it up, how it is manufactured, and, in some instance, it end-use applications. Such wires must have sufficient strength to withstand the fabrications process, device winding, cool-down and electromagnetic stress, and be capable of being made or dabbled to sufficient size to carry operating currents from hundred to thousands of amperes at costs comparable to Cu.

Both architectures will be described in the next section, focusing in the 2G since the aim of this Thesis is to produce a feasible multilayered system for coated conductors.

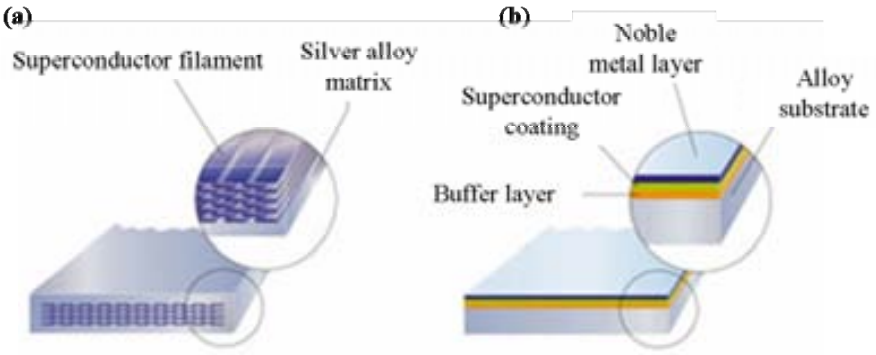

Fig. 1-5 (a) First-generation superconductive wire based on Bi-2223 superconductive filaments in a silver matrix (b) Second-generation (2G) YBCO-coated conductor [12].

1.2.1 Grain boundaries and epitaxy

Large devices need kilometres of polycrystalline conductors, however, early investigations of HTSC materials revealed a vexing feature: polycrystalline samples have typical J_c values of a few hundred A cm^{-2} at 4.2K, while single crystalline samples have values in the range of MA cm^{-2} at 77K. Grain boundaries induce structural disorder strongly blocking the critical current density across a grain boundary. J_c has been shown to decrease exponentially with the misorientation angle between adjacent grains orientations, θ, Fig. 1-6. This extreme sensitivity to misorientation, coupled with the intrinsic anisotropy of the HTSC compounds, dictates the need to adjoin HTSC grains in a practical wire or tape to be closely aligned crystallographically and achieve high levels of current conduction with low dissipation [16].

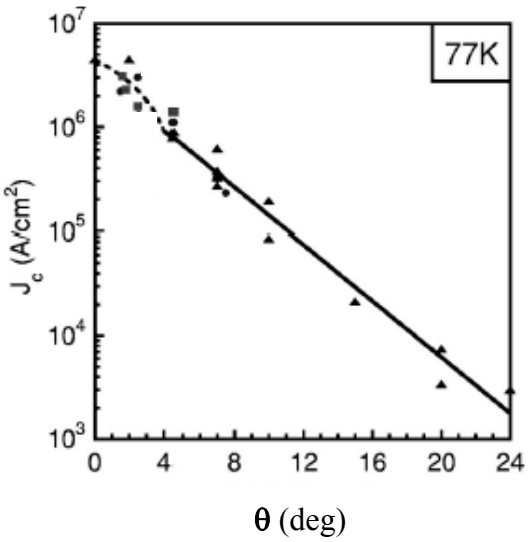

Fig. 1-6 Critical current density in $YBa_2Cu_3O_7$ films as a function of the misorientation angle [16] .

The first generation of HTSC wire is made from Bi-2223 superconductor, a family of HTSC that has plate-like grains that align easily by what is commonly referred to as the oxide powder-in tube (PIT) process. By means of thermo-mechanical deformation, one obtains an uniaxial texture since all the crystals are oriented along the substrate normal but they do not have a preferred orientation in the substrate plane, Fig. 1-7(a) [13]. However, Bi-2223 is by no means an ideal material, since it carries little current when used at 77K in high magnetic fields, as we earlier saw in Fig. 1-4. Therefore, researchers have continued to search for other forms of wire using HTSC materials such as YBCO.

The YBCO compound has the unfortunate problem that does not readily form wire like Bi-2223, grains are difficult to align. The key is to prepare a substrate, or template material that provide in-plane and out-of-plane crystallographic texture, i.e. biaxially textured (see Fig. 1-7(b)). Then, it is required that the orientation of underlying template or substrate could be transferred to YBCO film and thus, YBCO film grow in near single-crystal orientation (epitaxial growth). This represents one potential solution to the shortcoming to fabrication of long length YBCO wires, referred to as second generation (2G) YBCO wires as we previously mentioned.

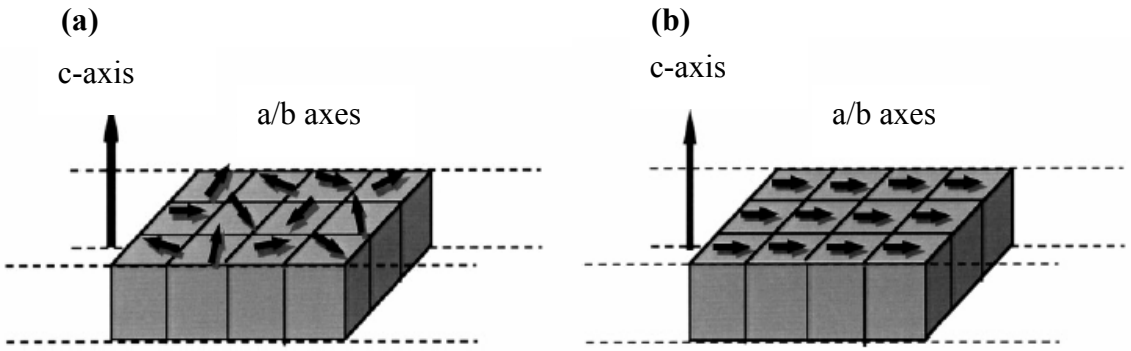

Fig. 1-7 Schematic diagrams for crystalline alignment structures (a) uniaxially aligned (b) biaxially aligned. [17]

1.2.1.1 Types of epitaxy and lattice mismatch

Depending on the nature of film and substrate as well as the lattice matching between them, two types of epitaxy can be distinguished and each has important scientific and technological implications. Homoepitaxy refers to the case where the film and substrate are the same material. The second type of epitaxy is known as heteroepitaxy and refers to the case where films and substrates are composed of different materials. Heteroepitaxy is the more common phenomenon and YBCO coated conductors are based on heteroepitaxial film structures.

Differences between the two basic types of epitaxy are schematically illustrated in Fig. 1-8. When the epitaxial layer (epilayer) and substrate crystal are identical, the lattice parameters are perfectly matched and there is no interfacial-bond straining, Fig. 1-8 (a) .

Lattice mismatch strain, ε_m, is then calculated according to the relation [18]:

$$\varepsilon_m = \frac{a_s - a_b}{a_b} \qquad \text{Eq. 1-1}$$

where a_b is the bulk lattice parameter of the film material and a_s is the lattice parameter of the substrate. Because the lattice parameter difference is normalized by the film lattice

parameter, ε_m corresponds directly to the strain experienced by an epitaxial film, assuming no relaxation mechanisms exist. If the film lattice parameter is larger than that of the substrate, ε_m is compressive.

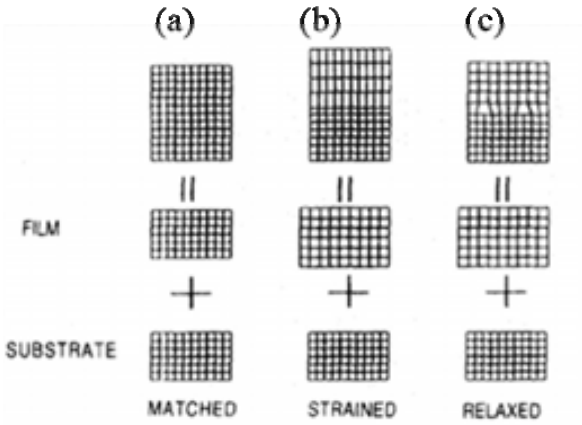

Fig. 1-8 Schematic illustration of lattice-matched, strained, and relaxed heteroepitaxial structures.

In heteroepitaxy the lattice parameters are necessarily unmatched, and depending on the extend of the mismatch ε_m, we can envision three distinct epitaxial regimes.

If the lattice mismatch is very small, then the heterojunction interfacial structure is essentially like that for homoepitaxy. However, differences in film and substrate chemistry and coefficient of thermal expansion can strongly influence the electronic properties and perfection of the interface.

When the film and substrate lattice parameters differ more substantially, we may imagine the other cases in Fig. 1-8 (b-c). Either the two lattice strain to accommodate their crystallographic differences or, if this is not possible, dislocation defects form at the interface (relaxed epitaxy). It usually occurs between film-substrate pairs composed of dissimilar materials which have the same crystal structure. The theory predicts that any epitaxial layer having a lattice-parameter mismatch with the substrate of less than ~ 9% would grow pseudomorphically, i.e., initially, very thin films strain elastically to have the same interatomic spacing as the substrate, making the interface coherent with atoms on either side lining up. With increasing film thickness the rising total elastic strain energy will eventually exceed the energy associated with a relaxed structure consisting of an array of misfit dislocations separated by wide regions of relatively good fit [19].

Here below they are summarized the structural properties of the main buffer layers and substrates used for YBCO coated conductors fabrication.

Table 1-I Structural properties of buffer layer materials and YBCO

Material	Structure	Lattice parameter (Å)	Lattice mismatch to YBCO(%)
$LaAlO_3$	Cubic, perovskite	3.79	-1.84
$SrTiO_3$	Cubic, perovskite	3.91	1.53
$BaZrO_3$	Cubic, perovskite	4.19	8.11
CeO_2	Cubic, fluorite	5.41	-0.52
$YBa_2Cu_3O_7$	Orthorhombic, perovskite	3.83 x 3.88	-
Ni	FCC	3.52	-8.57
MgO	Cubic, rock-salt	4.21	8.55
YSZ	Cubic, fluorite	5.16	-5.71
NiO	Cubic, rock-salt	4.17	7.67

The lattice parameters were obtained form the International Center for Diffraction Data, Powder Diffraction Files [20].

1.2.2 Approaches for coated conductors

It has proven that any manufacturing method for YBCO conductors relies on the epitaxial deposition of YBCO onto a textured substrate that provides strength and flexibility. In order to match lattice parameters and minimize any chemical interaction between the metal substrate and the oxide superconductor, epitaxial buffer layers are necessary [12].

Today, there are two principal approaches for achieving long length biaxially-textured coated conductor tape which are currently being developed for commercialization by several industries worldwide. One substrate technology, called rolling-assisted, biaxially textured substrates (RABiTS), was invented by Oak Ridge [21], while another, ion-beam assisted deposition (IBAD) was pioneered by Fujikura [22] and then substantially improved upon by the Los Alamos group [23] to the point where world wide interest in YBCO was re- ignited. Both architectures are briefly described in section 1.2.2.1 and 1.2.2.2.

Alternative approaches to texture buffer layers is through self-oxidation epitaxy (SOE) [24] or the so-called inclined substrate deposition (ISD) [25] where a single textured buffer layer is vacuum deposited in a polycrystalline substrate and the texture is achieved as a consequence of the higher growth rate of a given crystallographic orientation.

An appropriate YBCO-buffer-substrate architecture can be made by vacuum-deposition techniques (pulsed laser deposition (PLD)[26,27], sputtering [28], PVD BaF_2 process[29], metalorganic chemical vapor deposition (MOCVD)[30]) and/ or non vacuum techniques like liquid phase epitaxy [31] and chemical solution deposition (CSD)[32,33,34]. The chemical solution deposition route to epitaxial films has received the most attention and will be the focus of this Thesis, and thus we will describe it in more detail (1.2.3).

Additionally, a brief description of PLD and PVD BaF_2 process will be given because they have been used to fabricate YBCO films presented in this Thesis (1.2.3.2).

1.2.2.1 Rolling Assisted Biaxially Textured Substrates

In the technique known as RABiTS (Rolling Assisted Biaxially Textured Substrates), the substrate metal or alloy is biaxially textured by special thermo-mechanical processing procedures, providing an oriented template for the subsequent epitaxial deposition of buffer layer and YBCO coatings. The RABiTS architecture most commonly used consists of a CeO_2(sputtered)/YSZ(sputtered)/Y_2O_3(e-beam)/Ni-W alloy [14]. However simpler architectures based on two effective Ni diffusion barriers such as (La,Sr)MnO_3 and $La_2Zr_2O_7$ with an optional cap layer of CeO_2 or alternatively MgO are already developed in short length [35].

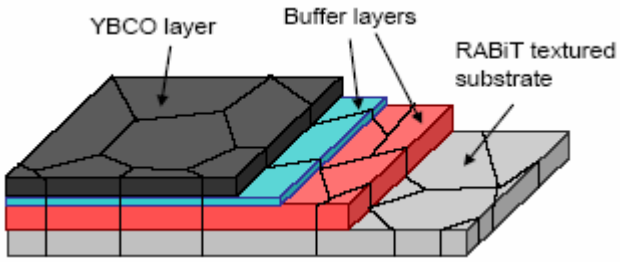

Fig. 1-9 A cross-sectional sketch of a coated conductor, based on the 'RABiTS' technology. A biaxially textured metal substrate is coated with buffer layers of various oxides to serve as a diffusion barrier to substrate atoms and to replicate the template, on which $YBa_2Cu_3O_7$ is deposited with biaxial texture.

1.2.2.2 Ion Beam Assisted Deposition

Another approach uses Ion Beam Assisted Deposition (IBAD), where an energetic ion beam irradiates the substrate at a particular angle during the deposition of an oxide buffer layer (yttrium-stabilized zirconia (YSZ)[36], $Gd_2Zr_2O_7$[15] or MgO[37]) onto a non textured metal tape (stainless steel, hastelloy or similar alloys). Additionally, some extra buffer layers can be grown between the IBAD-textured layer and the YBCO in order to enhance crystallographic

coupling between different layers and avoid chemical reactivity. CeO_2 has been successfully deposited epitaxially. Additionally, $BaZrO_3$, $SrRuO_3$, $SrTiO_3$ have been also tested.

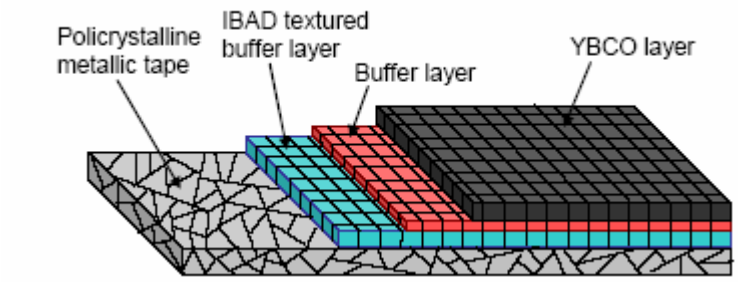

Fig. 1-10 Sketch of the IBAD approach for the production of $YBa_2Cu_3O_7$ coated conductor.

1.2.2.3 Buffer layer architecture

Buffer layers play a key role in YBCO 2G wire technology transferring the biaxial texture from the substrate to the YBCO layer. In addition, dense buffer layers are used to provide a good barrier for cation and oxygen diffusion. Aside from the poisoning of YBCO by cations from the substrate, the control of oxygen diffusion is a second major function of the buffer layer. Another essential role of the buffer layer(s) is that should be chemically stable and non-reactive with the YBCO, nonporous and strongly bonding. To date, no single buffer layer material has been found that meets all of these needs, and great effort is being devoted to find simple multi-layer architectures that function well.

Many materials have been proposed and demonstrated as buffer layer for YBCO films, but most have met with limited success [12]. In general, the search for buffer layer that can support the growth of YBCO film has centered on materials having a perovskite (ABO_3), fluorite-like (MX_2) or pyrochlore ($A_2B_2O_7$) crystal structure. In this work we have focused on the study of perovskite and fluorite structures fabricated by chemical solution deposition (chapters 5, 6 and 7).

In the *fluorite* structure, CeO_2 has proven to be one of the most effective cap layer (with vacuum technologies) due to it has a good lattice match to YBCO, see Table 1-I [38,39,40,41,42,43]. Presently, the preparation of CeO_2 buffer layer by CSD technique is in development, and first results have been obtained [38,44].

Perovskite is the other common cap layer structure for YBCO coated conductors. $SrTiO_3$ (STO) is a very attractive material for its excellent lattice match (see Table 1-I) and chemical compatibility with YBCO and is known to support the growth of high-quality superconducting films[45,46]. Many groups are pursuing the growth of perovskite buffer layers via CSD, onto

metal substrate for the development of an inexpensive, all sol-gel coated conductor [47,48,49,50].

1.2.3 Preparation routes

1.2.3.1 Chemical Solution Routes to Single-Crystal Thin Films

Chemical solution deposition (CSD) is now a well established discipline which has reached a wide use for the production of materials with high performance such as nanoparticles, bulk ceramics, hybrid materials, mesoporous solids, coatings, etc. [51,52]. Chemical solution deposition has recently appeared as a low cost alternative for the fabrication of 2G coated conductors. The main advantage of this methodology is that low capital investment and supply costs are envisaged, thus becoming a competitive alternative to vapor deposition techniques these requiring of vacuum systems. Other advantages are the high degree of compositional control inherent with the solution synthesis of multielement, inorganic materials.

A range of requirements must be fulfilled by the solution chemistry, substrates, and processing conditions for successful implementation of the CSD technique [53]: (1) sufficient solubility of the precursor in the solvent to form a stable coating solution,(2) synthesis of precursors that decompose or may be pyrolyzed without undesirable residues during thermal processing (3) acceptable wetting of the substrate,(4) no crack formation or compositional non uniformities during pyrolysis or crystallization.

The general principle involved in the solution deposition is to prepare a homogeneous solution of the necessary cation species that may later be applied to a substrate. The fabrication of thin films by this approach involves four basic steps (i) synthesis of the precursor solution, (ii) deposition by spin coating [54], spraying [55] dip-coating [51] or slot die coating, where drying process usually begin depending on the solvent, (iii) low-temperature heat treatment for drying, pyrolysis of organic species (typically 300-400ºC) and formation of an amorphous film, and (iv) higher-temperature heat treatment for densification and crystallization of the coating into the desired oxide phase.

(i) Solution preparation routes

A variety of precursor chemicals that include metal organic molecules, metal salts, and polymers can be pyrolyzed to synthesize oxides, carbides, nitrides and certain metals at modest temperatures.

The requirements of appropriate solubility combined with pyrolysis that leaves solely the cations (and oxygen) as a residue, represent an especially significant limitation regarding the

choice of precursors. Usually, metal-organic compounds are suitable, due to the fact that their solubility in polar or non-polar solvents can be tuned by modifying the organic part of the molecule, and because the organic moiety pyrolyzes in oxidizing ambient atmosphere without residue [51,56]. One of the most common precursors are carboxylates (R-COOH, where R represents an alkyl group) which can normally be dissolved in their own (parent) carboxylic acids, and for short alkyl chain salts, some solubility in water and other highly polar solvents is typically observed due to the polar nature of the salt. Alkoxides $(M\text{-}OR)_x$, β-diketonates (organic molecules with two keto groups separated by one methylene group ($-CH_2$)) and mixed ligand precursors are also frequently employed in CSD processing.

In addition to precursor properties, solvent choice is also an important consideration for control of film gelation and processing behaviour. The solvent that is selected must be suitable not only for the particular precursor system, but other solvent characteristics, such as evaporation rate, which can drive gelation, and surface tension characteristics, which can dictate substrate wetting behaviour.

To control precursor species characteristic, reaction conditions, viscosity, solute concentrations and solvent system must also be adjusted at this stage for the coating technique that will be employed and the type of substrate [57].

The various chemical routes utilized for thin film growth can be grouped into three principal categories:

● sol-gel process that use alkoxide precursor that undergo primarily hydrolysis and polycondensation. This process is the most frequently used for silica [58].

● metal organic decomposition (MOD) routes that utilize carboxylate precursors that do not undergo significant condensation reactions during either solution preparation or film deposition. In this thesis we have synthesized YBCO and buffer layer films (CeO_2,$SrTiO_3$,$BaZrO_3$) by MOD route and thus below we will describe meticulously this category.

● hybrid routes that exhibit condensation reactions at several process stages, frequently, this route is used for preparation multicomponent oxide films [59].

Other processes that have also been studied for the deposition of other perovskite thin films are : Pechini [60], citrate [61] and nitrate processes [62].

(ii) Coating techniques

Once the precursor solution has been prepared, films are typically formed by spin coating. Excess solvent removed during coating forms a solid or gel precursor film. At the laboratory scale, spin deposition is usually achieved with a spinner and the substrate is typically a planar single crystal oxide. The substrate is held in place on the spinner and the wafer is then accelerated rapidly to 1000 to 6000 rpm. The angular velocity and the spinning time, together with the solution viscosity, can be used to control the thickness of the wet film. This

characteristic and the solute concentration will, in turn, determine the thickness of the final ceramic film.

(iii-iv) Pyrolysis and heat treatment

To complete the transformation of the as-deposited film into the crystalline ceramics, two approaches are commonly used: one-step process, in which organic removal and crystallization are accomplished in the same processing step, which is carried out at temperatures sufficiently high to induce crystallization of the oxide. Two-step process, the removal of (at least most of the) organic constituents is carried out in a separate processing step at lower temperatures (200-400ºC) prior to a high- temperature crystallization step.

It is important to remark that the organic removal characteristics and the pathway by which the crystalline phase evolves are dependent on the precursor chemistry employed, the material chemistry, heating rate and temperature.

1.2.3.1.1 Metalorganic decomposition (MOD)

This solution-synthesis approach has historically used large carboxylate compounds. The basic approach consists of simply dissolving the metal-organic compounds in common solvent, and combining the solutions to yield the desired stoichiometry. Since most of the starting compounds are water-insensitive, they do not display the oligomerization behaviour and the precursor species that exist in solution retain a strong resemblance to the starting molecules.

While the MOD procedure is straightforward, it possesses a number of limitations. First, the large organic ligands may cause cracking during thin film processing due to the excessive weight loss and shrinkage that can occur. To circumvent this, control of solution concentration and thermal processing is required. Alternatively, short chain carboxylate (e.g., acetate, propionate) and strongly chelating β-diketonate (e.g., acetylacetonate acac-type) compounds can be used. The use of chelating ligands such as acac can lead to the formation of monomeric compounds and the lower organic content of the precursors reduces film shrinkage after deposition, decreasing problems with film cracking.

In this work CeO_2, $SrTiO_3$ and $BaZrO_3$ buffer layers have been prepared by this route and its detailed synthesis are described in chapter 3. By contrast, YBCO film has been synthesized by a modified route using trifluoroacetates as precursors. This alternative approach is called TFA-YBCO and is briefly described below.

1.2.3.1.2 Metalorganic decomposition by Trifluoroacetate route

Conventional carboxylic or alkoxide metal-organic precursors can be often used to prepare buffer layer oxides, as already described above. However, its use to grow YBCO films has been limited because they lead to the formation of $BaCO_3$ which requires high temperatures to decompose and then the final microstructure is considerable degraded [63].

Gupta and co-workers [32], firstly demonstrated the possibility to use a modified metalorganic decomposition (MOD) approach using trifluorinated (TFA) salts as a versatile route for achieving epitaxial YBCO layer with high critical current. TFA precursors lead to BaF_2 as a final product after the decomposition of the metal-organic precursors and avoid the formation of $BaCO_3$. The growth of superconducting epitaxial YBCO layers follows a complex process based on the as-presented for CSD films which involve three different stages: the pyrolysis step, the growth process, and finally the samples are subjected to an oxygenation annealing step. We explain the detailed procedure to prepare TFA-YBCO films in Chapter 3, however, in section 1.2.3.1.3 we describe a general outline of the TFA- YBCO process.

Presently, TFA-YBCO process is a well-established CSD route for the coated conductor development and it has been successfully transferred to industry. Recent studies performed by Xu and coworkers [64] show a novel processing method using fluorine-free precursors obtaining J_c over 1 MA cm^{-2} at 77K on YSZ substrates. Even though this new approach avoids HF reaction product, it hinders the control of YBCO growth rate (see 1.2.3.1.4.1) and therefore, fluorine precursors are still preferred.

1.2.3.1.3 Film crystallization in CSD: fundamental aspects.

In this section, some of the underlying thermodynamic aspects of the processes that affect thin film microstructure will be briefly discussed [65,66]. The theoretical description for nucleation and growth in solution-derived films is analogous to that used extensively to describe crystallization in traditional glasses.

Nucleation of a new phase requires creation of an energetic interface, and this represents a large energy barrier [67]. The diagram shown in Fig. 1-11 demonstrates the differences in free energy (ΔG_v) between the solution-derived amorphous film and the crystalline ceramic phase. While this diagram does not necessarily provide insight into the transformation pathway the film undergoes, it is useful in understanding the role that driving force, ΔG_v, can have on the transformation process, and thus, the final microstructure of the ceramic film.

Consideration of driving force is important since it influences the barriers for nucleation of the crystalline phase at different locations (substrate interface, surface, bulk) within the film, as well as nucleation rate [68].

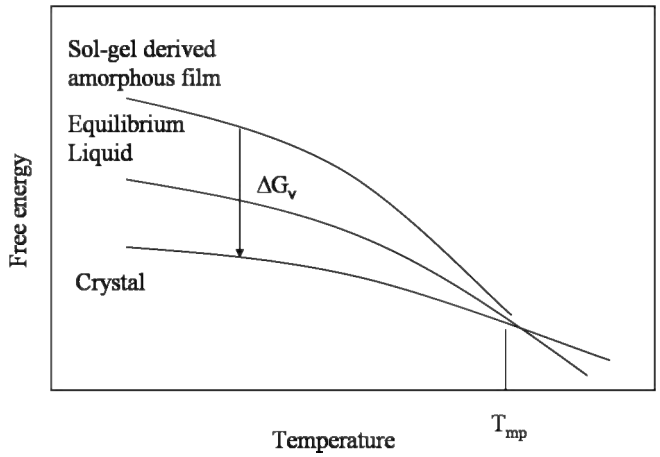

Fig. 1-11 Schematic diagram of the free energies of a CSD derived amorphous film, the ideal suprcooled liquid, and a crystalline perovskite phase[66].

The energy barriers for homogenous nucleation (crystals nucleate distributed through the bulk of the film because activation energy is nearly the same for all points of the amorphous film) and heterogeneous nucleation (crystals originate at the film/substrate interface) and their dependence on driving force are described below:

$$\Delta G^{*}_{\mathrm{hom}o} = \frac{16\pi\gamma^{3}}{3(\Delta G_{v})^{2}} \qquad \text{Eq. 1-2}$$

$$\Delta G^{*}_{hetero} = \frac{16\pi\gamma^{3}}{3(\Delta G_{v})^{2}} f(\theta) \qquad \text{Eq. 1-3}$$

$$f(\theta) = (2 - 3\cos\theta + \cos^{3}\theta)/4 \qquad \text{Eq. 1-4}$$

The difference in barrier heights depends on the interfacial energy, γ, driving force for crystallization, ΔG_v, and the contact angle, θ. Finally, $f(\theta)$ is a function related to the contact angle, θ, according to Eq. 1-4.

The thermal energy available (via heat treatment during the crystallization anneal) to surmount these different nucleation barriers defines which nucleation events take place, and thus, the resulting film microstructure. Rapid thermal processing to a temperature close to the melting point, where AG_v is too small to overcome homogeneous nucleation barriers, can be used to promote interfacial nucleation and therefore columnar final microstructure.

Unless rapid thermal processing techniques are used, film crystallization usually begins during heating to the anneal temperature. Therefore, as the temperature of the sample is increased, more thermal energy becomes available to surmount the barriers for nucleation events that are not necessarily the most favourable energetically. This can lead to film microstructures defined by nucleation and growth processes associated with more than one nucleation event.

The competition between homogeneous and heterogeneous nucleation is especially important in cases where a particular orientation of the crystal is required, as in films studied in this thesis (CeO_2, $SrTiO_3$, $BaZrO_3$, YBCO).

In this way, epitaxial films by CSD, where nucleation occurs under very high undercooling, are obtained by promoting secondary grain growth within a nanostructured matrix of those oriented grains heterogeneously nucleated on the substrate [69]. The elimination of grain boundaries in the initial polycrystalline film is the apparent free energy driving the epitaxial grain growth phenomenon. This will be the scenario found for MOD-CeO_2 films [38,70].

Conversely, YBCO nucleation mechanism from trifluoroacetate precursor is still not clear at the present. However, a microstructural scenario consisting in a competitive nucleation growth between heteroepitaxial YBCO and bulk $Y_2Cu_2O_5$ has been recently proposed in our group through TEM and XRD investigations [71].

Interestingly, these particular features of CSD deposition offer the possibility to generate specific film nanostructures by properly tuning the evolution from the nanostructured to epitaxial forms by playing with sintering conditions or chemistry precursors [72,73].

1.2.3.1.4 TFA-YBCO process

The demonstration of the possibility to use trifluoroacetate (TFA) precursors leading to BaF_2 (rather than the detrimental $BaCO_3$) as a final product after the decomposition of the metal-organic precursors and finally to epitaxial thin films must be considered as a very significant step towards the achievement of a reliable methodology of low cost production of chemically based coated conductors [33,74].

1.2.3.1.4.1 Precursor study of YBCO films

Interestingly, TFA and PVD BaF_2 ex-situ processes displays a very similar growth mode due to components of pyrolyzed film are the precursors partially oxidized of BaF_2 process [75]. However, there are still many issues in the process which are poorly understood and which are essential for achieving high rates of production of high-performance coated conductors. It is particularly important to understand YBCO conversion pathway. Many authors have focused

their studies on the pyrolysis step in order to elucidate the nature of the intermediate phases [76,77,78]. They identified by XRD analysis BaF_2, Y_2O_3 and CuO nanocrystals embedded in an amorphous matrix. Contrasting with these results, in our group, by TEM, XRD and μ-Raman investigations it has been found a slighltly different scenario. It has been identified CuO nanoparticles and $Ba_{1-x}Y_xF_{2+x}$ (BYF) solid solution in a quasi-amorphous matrix as a resulting product [71]. Studies on the fluorine content in the precursor film are still matter of debate. In fact, Wong–Ng and Yoshizumi [79,80] found that the reaction path taken upon conversion of ex situ films is not a simple single reaction but consists of multiple steps. Excess fluorine in the form of YF_3 is decomposed by reaction with water at low temperature leading to BaF_2-YF_3 alloy [81]. On the other hand, while in films synthesized by PVD BaF_2 ex-situ process, an oxyfluoride melt during the conversion process has been detected, recent studies performed in our group have confirmed that TFA-YBCO does not [71]. Indeed we have found that the microstructural evolution of the precursor is driven by the reduction of the solid solubility of Y in the BYF solid solution and then, Y is released in the form of Y_2O_3 which can react with CuO to form $Y_2Cu_2O_5$. In particular, the formation of this latter oxide is particularly relevant because it occurs at temperatures very close to the epitaxial nucleation of YBCO, and therefore both processes may constitute competitive phenomena thereof affecting the kinetics of the conversion process.

Since YBCO pathway conversion can take place through different scenarios which are not well understood its hard to define a single chemical reaction. Therefore, we have proposed the following flow chart,

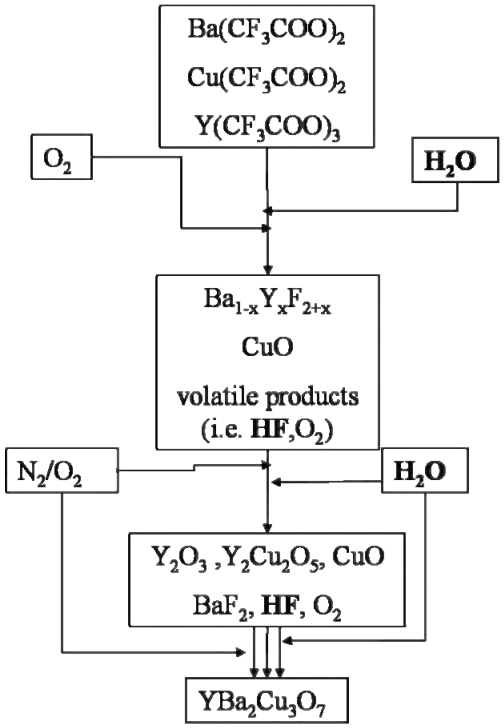

Fig. 1-12 Flow chart of the path reaction of YBCO film from $Cu(CF_2CCO)_2$, $Ba(CF_3COO)_2$ and $Y(CF_3COO)_3$.

1.2.3.1.4.2 Kinetics of YBCO film growth

Concomitantly with the compositional study, kinetics of the precursor decomposition has to be known precisely in order to obtain an homogeneous film as will be shown further on in this thesis (chapter 3) [82,83,84].

The determination of the optimal growth conditions of the TFA-YBCO films has been widely investigated (still controversial), but it has been shown that a close relationship exists between temperature, water partial pressure ($P(H_2O)$), gas flow and oxygen partial pressure ($P(O_2)$) since they control the nucleation and growth rate of YBCO and determine its microstructure, see Fig. 1-13.

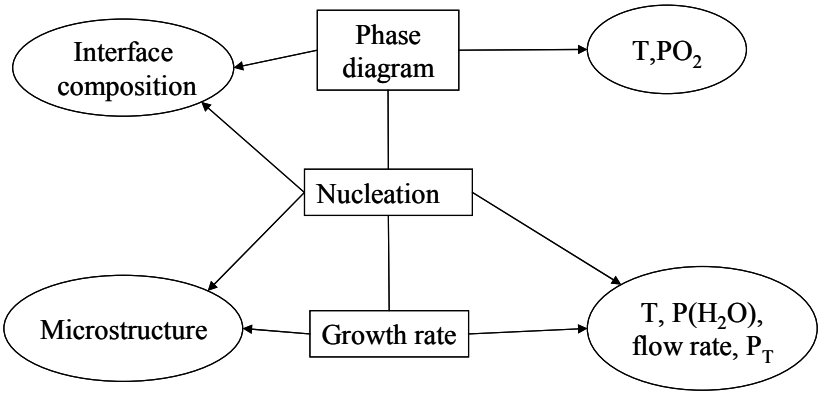

Fig. 1-13 Flow chart of the $YBa_2Cu_3O_7$ layer growth process and the parameters controlling the growth rate and the microstructure

Honjo and coworkers reported a theoretical analysis proved experimentally of the TFA-YBCO growth rate [85] . For this analysis, they have defined the scenario of reaction in three regions (1) YBCO film, (2) precursor film and (3) a stagnant gas boundary layer surrounding the precursor film. Fig. 1-14 shows the physical image of this model. An essential consideration is that the reaction involves an exchange with the gas-solid phase because the water vapour must reach the film interface where the reaction occurs and the HF must be evacuated in order to avoid a stagnant proves that would locally block the advancement of the reaction. It is very important then to have a laminar gas flow which assures that reaction of YBCO conversion proceeds.

To carry out this analysis they have assumed that the YBCO growth rate (R) was independent of the oxygen partial pressure during processing [86]. Therefore, it has been analyzed the mass transfer of H_2O and HF gases, which in equilibrium conditions are related by K_e [85],

$$K_e = \frac{a_{HF}^2}{a_{H_2O}} \qquad \text{Eq. 1-5}$$

Experimental results showed that R was independent of film thickness and proportional to the square root of the water partial pressure. Considering that the water vapour pressure used in their experimental study is high enough, the mass transfer in the gas boundary layer limit the growth rate. Consequently, this dependence can be written as follows,

$$R = \frac{V_{YBCO}}{2V_{gas}} J_{H_2O} = \frac{V_{YBCO} D_g \sqrt{K_e X_{H_2O}}}{4 V_{gas} \delta_g} \qquad \text{Eq. 1-6}$$

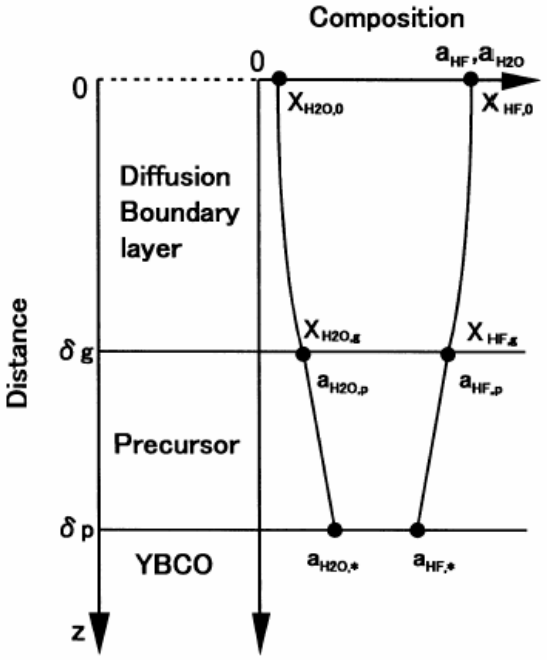

Fig. 1-14 Sketch of the mass transfer model for the TFA-YBCO growth. a_{HF} and a_{H2O} are the activities of HF and H_2O . δ_g and δ_p are the boundary layer and precursor layer thickness respectively [85].

where V_{YBCO} and V_{gas} are the molar volume of the YBCO crystal and that of gas, respectively and X_{H2O} is the molar fraction of H_2O. D_g is the mass diffusivity in the gas film, $K_e = (a_{HF})^2/a_{H2O}$, and finally δ_g the gas boundary layer thickness. Similar dependence was also observed earlier in YBCO film grown by PVD BaF_2 ex-situ process [87].

Moreover, it was suggested that processing parameters such as diffusivity (which is in inverse proportional to P_t) and the gas flow rate (which is in proportional to V_g) also could affect the growth rate from the above analysis, Eq. 1-6. Indeed, by investigating P_t and V_g

dependences on the YBCO growth rate, R, it was confirmed that the higher R could be achieved by higher $P(H_2O)$ values as exposed above, higher D_g and higher V_g [88,89],

$$R = B\frac{\sqrt{P_{H_2O}}}{P_{total}^{n}} \qquad \text{Eq. 1-7}$$

where B is a constant and n≈1.

Consequently, the effective indications have to be considered to design and to fabricate YBCO thin film on single crystal substrate as model systems and of course to realize a long-tape fabrication equipment.

1.2.3.1.4.3 Phase formation of YBCO film

While the kinetics of gas exchange likely control certain aspects of the YBCO growth, other parameters related to phase formation such as transitory oxygen concentration involves a good knowledge of the PO_2-1/T YBCO phase diagram. It is important to distinguish the role of oxygen during the initial high-temperature crystallization of tetragonal YBCO from those occurring at lower temperatures in a later stage of the synthesis process. Unfortunately, the latter has been scarcely studied in thin films specimens.

For over ten years it has been known that the growth of high-quality epitaxial YBCO thin films may be performed under conditions near the stability line (indicated by *YBCO unstable* in Fig. 1-15), i.e., low processing temperatures and low $P(O_2)$. Feenstra and coworkers [90] observed a systematic in YBCO surface morphology which reflected a dependency of epitaxial growth properties on both temperature and oxygen pressure. Similar study was performed in our laboratory for TFA-YBCO films on different substrates [91]. Independently of the underlying substrate, three film morphologies were distinguished. In Fig. 1-15 it has been presented the morphology distribution for TFA-YBCO/LAO system. At highest temperatures and highest $P(O_2)$, films are unstable. This phenomenon will be discussed in detail in Chapter 4. At low $P(O_2)$ and intermediate-low temperatures, films are predominantly ***c*** oriented. Finally at intermediate $P(O_2)$ and intermediate-low temperatures films exhibited enhanced tendency for formation of *a*-grains.

The diagram in Fig. 1-15 also contains the CuO-Cu_2O-O equilibrium line, originally proposed by Bormann and Nötling as the common decomposition line of YBCO [92]. Despite the decomposition line has been shifted to lower oxygen pressures and temperatures renamed to as YBCO unstable, it provided a useful starting reference for subsequent investigations. The

tetragonal to orthorhombic transition, during the oxidation step, often applied at 101 kPa and temperatures 400 and 550ºC is also represented in the diagram by the data of Specht [93].

Despite this diagram was originally designed for samples grown *in-situ*, it has been corroborated that it has a general validity and modifying these parameters allows us to tailor the microstructure of YBCO films.

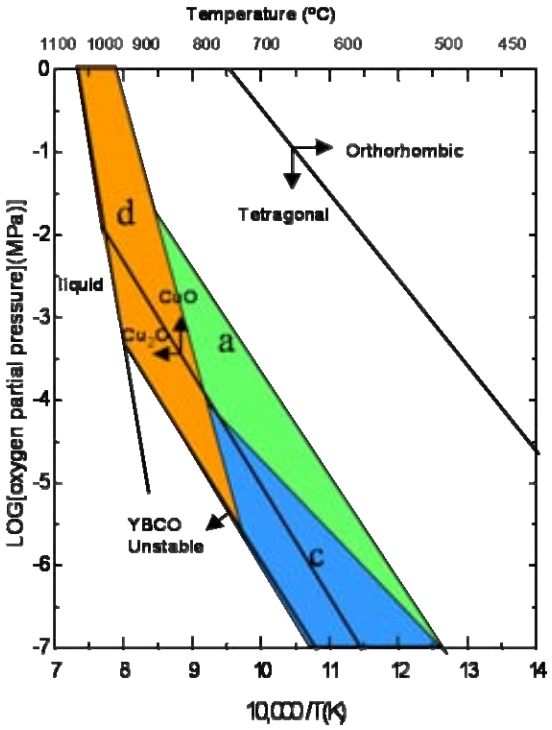

Fig. 1-15 Oxygen partial pressure versus temperature diagram showing conditions explored in TFA-YBCO/LAO system. Annealing conditions yielding films predominantly c-oriented are denoted by **c** and blue coloured. Annealing conditions yielding films predominantly a-oriented are denoted by **a** and green coloured. Finally annealing conditions leading to instability are denoted by **d** and orange coloured [91].

1.2.3.2 Physical routes

In this section are described two alternative techniques that have been used to grow YBCO films for a comparative study. Pulsed laser deposition (PLD) and physical vapour deposition (PVD) BaF_2 ex-situ.

1.2.3.2.1 PVD BaF_2 ex-situ

YBCO films were synthesized by PVD BaF_2 ex-situ process at Oak Ridge National Laboratory (ORNL), Tennessee-USA, in the group of Dr.R.Feenstra during my stay of two month.

PVD BaF_2 ex-situ process is a two-step process [94]. First involves a low temperature deposition of precursor layers formed by simultaneous evaporation from electron-beam Y, BaF_2, and Cu sources in a stainless-steel vacuum chamber. The film composition is controlled by three separate e-beam sources and by carefully positioning the substrate (or moving the substrate) to achieve the required flux balance [90]. Immediately following deposition, small amounts of O_2 were dosed into the vacuum chamber to partially oxidize the deposit and minimize the reduction of substrate CeO_2 buffer layers. The precursor film is thought to be purely nanocrystalline.

The precursor film is subsequently reacted to form YBCO in a separate heat treatment step in a tubular furnace, similarly to the high temperature step in TFA-YBCO route. The furnace is equipped to operate with flowing gas mixtures of He/O_2. The high-temperature hold is performed entirely under wet conditions needed to decompose BaF_2 precursor and results in conversion into YBCO through oxyfluorite $Ba(O_xF_y)$ superlattice [95]. At 500-550ºC the argon flow was stopped and the oxygen pressure increased to 101.3 kPa for a 15-30 minutes at 450ºC.

For standard growth, maximum temperatures during annealing reached 750ºC and the flow rate was 0.1 ms^{-1} for thickness value of 210 nm. The oxygen partial pressure was fixed at 0.02kPa and the water partial pressure at ~1.3 kPa [90].

We have deposited YBCO films on MOD-$BaZrO_3$/LAO substrate from ICMAB and on STO single crystal and on CeO_2/YSZ/Y_2O_3/Ni-W substrates from ORNL. The success of this method is largely determined by the annealing procedure, while relatively simple deposition technique may be used for the synthesis of the precursor film.

1.2.3.2.2 Pulsed Laser Deposition

Pulsed laser deposition (PLD)-YBCO samples analyzed in this thesis were grown at the IFW in Dresden (Germany) by Dr. R.Hühne during my short stay of two weeks. In this case YBCO films were deposited on MOD-CeO_2/YSZ and MOD-doped CeO_2/YSZ substrates from ICMAB.

PLD is one of the most convenient methods to obtain thin films of YBCO with high critical current density (J_c), as reported in [26,27]. PLD process takes place in a controlled environment and deposition regime. During PLD process, highly compacted pellet of stoichiometric YBCO

powder (target) is subjected to a KrF exicmer laser beam and a luminous cloud (the plasma plume) is formed along the normal of the target which contains thermally emitted ions, electrons, neutral atoms and molecules in a vapour phase. It is done in such a way that the tiny amounts of vaporized material are deposited stoichiometrically on the substrate situated in front of the plume [96,97]. In order to obtain a uniform target erosion and consumption, the target is rotated and wobbled simultaneously during the deposition process. The interaction of the laser beam with the target material is affected by a number of parameters like the absorption coefficient and the reflectivity of the target material, the pulse duration, and the energy of the laser beam.

For the preparation of the 300 nm-thick YBCO films studied in this thesis, it was used a standard PLD geometry using a KrF-excimer (Lambda Physik LPX305i) laser running at 5Hz with a deposition rate of about 1Å/pulse. The chamber was equipped with a turbo molecular pump, a gas-flow system with two different gas channels, and a butterfly valve that was connected to a vacuum gauge to control the gas flow into the chamber.

The deposition was carried out in an oxygen atmosphere, $P(O_2)$=0.03 kPa with a substrate temperature of 810ºC. After deposition, the samples were cooled in 40 kPa O_2 [98].

It is worth noting that traditionally PLD technique has large impact on the morphology of the sample and droplets of submicrometre size are difficult to be avoided on the surface of the deposited film unless off-axis deposition is used. On the other hand, one of the most important problems of conventional PLD, is that it is limited to small areas because of its low-volume deposition speed (under 2nm m^2 h^{-1}). However, Usoskin and coworkers [27,36] have developed an advanced deposition method for reproducible manufacture of high-performance YBCO coated conductors using High-Rate Pulsed Laser Deposition (HR-PLD). This process allows both increase of deposition speed by an order of magnitude and large area deposition. Moreover, with carefully chosen processing parameters, it also allows to obtain several micrometers thick YBCO without an appreciable deterioration of microstructure (J_c >1.4 MA cm^2 for >3 mm-thick films) [36].

Contrasting with MOD-TFA route (section 1.2.3.1.4) in which the quality of YBCO film is principally governed by growth temperature, water partial pressure, oxygen partial pressure and gas flow rate [99], in PLD technique the quality of the growing film is controlled by laser energy density on the target, frequency of the laser pulses, substrate temperature, and gas pressure in the chamber during deposition. In addition, if we also take into consideration that the starting materials to obtain YBCO thin film for MOD-TFA route (precursor solution that evolutes to nanoparticles embedded in a amorphous matrix) is completely different from PLD process (stoichiometric YBCO pellet that is atomizated keeping the original stoichiometry), it is clear that YBCO growth mechanism will strongly differ [100,71].

CHAPTER 2

Experimental techniques

In this chapter we will describe the techniques that we have directly used in this Thesis for the characterization of $YBa_2Cu_3O_7$ (YBCO) films and buffer layers ($SrTiO_3$, $BaZrO_3$ and CeO_2) as well as precursor solutions.

X-ray diffraction analysis has been performed at 'Institut de Ciència de Materials de Barcelona (ICMAB)' by specialized technician and at 'Serveis-Científico Tècnics de la Universitat de Barcelona (SCT-UB)'.

Atomic Force Microscopy (AFM) analysis has been carried out at ICMAB by specialized technician.

Scanning Electron Microscopy images have been registered at ICMAB and at 'Serveis de Microscòpia Electrònica de la UAB (SME-UAB)'.

TEM images have been carried out by other members of the group at SCT-UB and SME-UAB.

RHEED measurements have been performed at Leibniz-Institut für Festkörper-und Werkstofforschung Dresden in collaboration with Dr.R.Hühne and B.Holzapfel during my short stay of two weeks.

XPS analysis was done at 'Instituto de Ciencia de Materiales de Sevilla (ICMSE)' during my stay of two month, thanks to the collaboration with Dr. Juan Pedro Espinós and A.R. González-Elipe.

Additionally, a brief description of DC-magnetometry and electrical resistivity performed at ICMAB by other members of the group will be presented.

Micro-Raman spectroscopic studies were performed by other members of the group at the Raman laboratory located at the Universitat Autonoma de Barcelona (UAB).

Finally, TGA and ICP analysis will be described to provide a complete understanding of the different techniques presented in this Thesis. TGA analysis has been carried out in Solid State Chemistry laboratory at ICMAB and ICP analysis was performed by technicians from the Chemistry department 'Centre Grup de Tècniques de Separació en Química (GTS)' (UAB).

2.1 Surface film characterization

2.1.1 Atomic Force Microscopy (AFM)

Images were measured in a Microscopy PicoSPM (Molecular Imagine) system in tapping mode imaging. Standard NCL triangular contact mode tips (k=30-70 Nm^{-1}) were used with the total interaction force kept as low as possible. The images were processed with the software package WSxM from Nanotec Electronica S.L. (http://www.nanotec.es) and PicoScan Version 5.3.3 Molecular Imaging.

The principles on how the AFM works are very simple [101,102]. An atomically sharp tip is scanned over a surface with feedback mechanisms that enable the piezo-electric scanners to maintain the tip at a constant force (to obtain height information), or height (to obtain force information) above the sample surface.

A major advantage of detecting forces rather than current is that all kinds of material surface including metals, semiconductors, and insulators are imageable. There are three basic modes of operation depending on the tip force and tip-specimen separation. When the tip and specimen are widely separated, van der Waals forces cause then to weakly attract: non contact AFM mode. But when they draw too closely together, their electron clouds overlap and electrostatic repulsive forces physically push them apart: contact AFM mode.

The images captured for this Thesis have been registered in *tapping* mode where the cantilever is oscillated at its resonant frequency (often hundreds of kilohertz) and positioned above the surface so that it only taps the surface for a very small fraction of its oscillation period. This is still in contact mode, but the very short time over which this contact occurs means that lateral forces are dramatically reduced as the tip scans over the surface. When imaging poorly immobilised or soft samples, tapping mode may be a far better choice than contatct mode.

By using PicoScan software package it has been systematically visualized and analysed the captured images. First of all it has been applied a Levelling Operator to remove the general slope of a surface. This slope can be the result of a measurement that was not strictly horizontal. Subsequently it has been applied Line by Line Correction Operator which helps to reduce the defects generated by the AFM instrument.

Then, we have evaluated the rms roughness surface in 20 x 20 μm and 2 x 2μm area scan from our films. If the measured surface topography is represented as a surface profile z(x), the rms roughness is defined as the root mean square of the deviations of the surface profile z(x) from the mean line.

We have also studied the topography of our films through profile analysis. It consists in measurements of heights along a line on a surface. From this analysis we studied the shape of the surface grains: rounded or flat, the grain size and also its height.

Concomitantly, software package MountainsMap SPM-Image 4.1 allowed us to perform a quantitative estimation of the atomically flat surface on buffer layer films. To perform this quantification, after applying the as-mentioned line by line correction, we defined a height threshold value, i.e. ~1.8 nm, to identify an atomically flat surface, see Fig. 2-1(b). In order to count the area occupied by flat grains we applied the binarization operator which considers as background higher contribution to the fixed threshold value. It results a binary image like the one presented in Fig. 2-1 (c). Blue area corresponds to atomically flat grains, in black it is visible the background (points above a threshold). Finally, from the binary image it has been performed a statistics over all grains selected to obtain the percentage of atomically flat area, as is shown in Fig. 2-2.

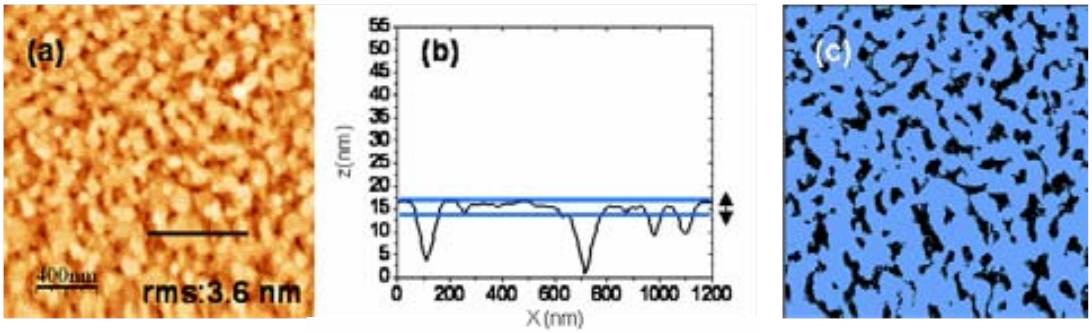

Fig. 2-1 (a) AFM topographic image of MOD-CGO film (b) profile scan performed on the AFM topographic image shown in (a), (c) Binary image resulting from the quantification of the atomically flat area.

Mean parameters on 678 grains

Total area occupied by the grains: 3.08 µm2 (76.9 %)
Density of grains: 169 grains / µm2.

Area	=	4538 nm2	+/- 116742 nm2
Perimeter	=	139 nm	+/- 3364 nm

Fig. 2-2 Mean parameters computed on the Binary image shown in Fig.2-1(c)

Subsequently, to confirm that the 'window' selected is indeed less than the fixed threshold value, a binary masking operator has been applied on the original AFM topographic image resulting a 3D image of only the atomically flat area, Fig. 2-3(a). Then, on this 3D image it can be computed several amplitude parameters to characterize the distribution of heights, Fig. 2-3 (b). Among them, we are interested in *Sq* which is the efficient value for the amplitudes of the surface (rms) and therefore, it is very useful to verify that selected area is atomically flat.

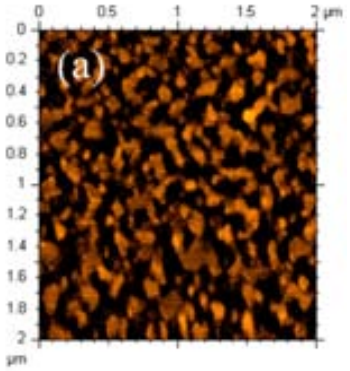

(b)

Sz, Sds and Ssc parameters are defined according to EUR15178N report.

Amplitude Parameters

Sa	=	1.33 nm
Sq	=	1.63 nm
Sp	=	11.7 nm
Sv	=	1.74 nm
St	=	13.4 nm
Ssk	=	0.918
Sku	=	3.98
Sz	=	12.6 nm

Fig. 2-3 (a) 3D image of the area selected (b) parameters calculated on the surface displayed in (a).

When the surface includes local structures for example outgrowth, see Fig. 2-4, the levelling will be affected by these structures. In this case, it is possible to extract this outgrowth by applying a binary masking operator beforehand. Then it is followed the as-described procedure to finally obtain a binary image (see Fig. 2-5)

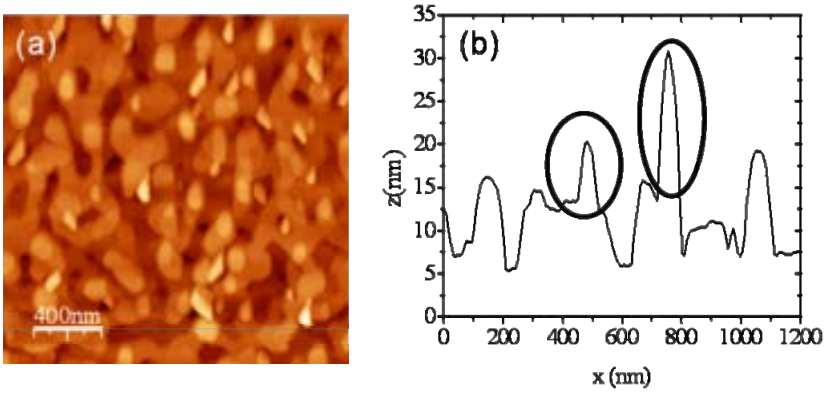

Fig. 2-4 (a) AFM topographic image of CGO film on YSZ single crystal (b) its corresponding height profile analysis where it is marked with a circle outgrowth contribution.

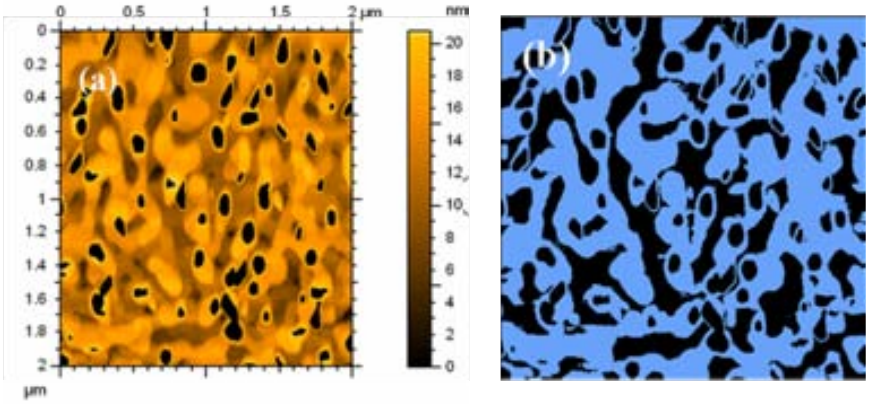

Fig. 2-5 (a) AFM image after applying a binary masking operator to eliminate outgrowth contribution in the estimation of atomically flat area (b) Binary image from (a).

2.1.2 Reflection high-energy electron diffraction (RHEED)

RHEED measurements have been carried out in a system from STAIB Instruments. RHEED provides information about the periodic arrangement of the surface atoms and, therefore, it is often used for the investigation of the surface structure and morphology during

thin film growth. However, in this Thesis it has been used to investigate surface texture and morphology of as-grown and processed CeO_2 films.

An electron beam of energy 30 keV, is directed at a glancing angle of 0.5-2.5º at sample held in the centre of an ultra-high vacuum chamber. We used beam currents <100μA. To estimate the depth sensitivity of RHEED in our CeO_2 films we have to refer to the mean free path (λ) curve [103]. At 30keV the mean free path normal to the surface is λ sin γ where γ ~ 0.5-2.5º is the glancing angle. The result is about 8-10 nm. Diffracted electrons fall on a CCD camera on the other side of the chamber giving a typically diffraction pattern characteristic for the analyzed surface. The simplicity and robustness of the technique is immediately apparent.

The area that can be examined by RHEED is quite imprecise in the direction of the beam due to the glancing nature of RHEED, of order of 1 mm. Thus, in our films, it has been examined different area from the same sample in order to obtain a representative pattern.

An analysis of the intensity distribution along the (00) and its neighbouring diffracted dots or streaks (see Fig. 2-6) is used to obtain information about the surface roughness. The RHEED pattern from a perfectly ordered flat surface consists of sharp spots aligned on arc called Laue circles Fig. 2-6(a-b). For a surface with domains, e.g., terraces, the spots on the arcs are elongated into streaks perpendicular to the shadow edge, Fig. 2-6(c). In case of a rough surface, the e-beam can penetrate through surface islands. In this case, the electrons produce 3D Bragg diffraction pattern and the streaks are replaced with points. Results are then spotty RHEED patterns that look like an image from a transmission electron microscope, Fig. 2-6(d). Furthermore, it is evident that diffraction from an amorphous surface gives no diffraction pattern at all, and only a diffuse background will result.

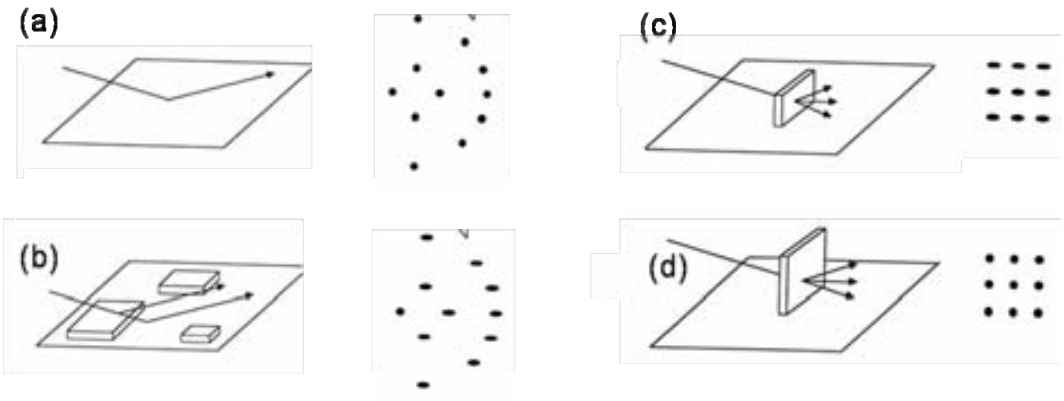

Fig. 2-6 Sketch of different surface morphology and its characteristic RHEED pattern.

2.1.3 X-Ray Photoelectron Spectroscopy (XPS)

XPS measurements were performed with an X-ray photoelectron spectrometer (ESCALAB 210) at a base pressure < 10^{-10} mbar Eclipse software was employed for instrumental control, data collection and spectra processing.

The detection and energy analysis of photoelectrons produced by radiation whose energy exceeds their binding energies is the subject of an extensively used technique known as Photoelectron (PE) Spectroscopy. When x-rays are employed, it is termed X-ray Photoelectron Spectroscopy (XPS). XPS is also known as electron spectroscopy for chemical analysis (ESCA) in order to emphasise the presence of both photo- and Auger electron peaks in the XP spectrum.

The main advantages of XPS are its ability to provide vital chemical information, simple quantitative information, low sample damage and the fact that it can be used to study insulating materials. The only major disadvantage of XPS is its relatively poor lateral resolution which has been improved in recent times.

2.1.3.1 XPS spectrum

An XP spectrum is generated by plotting the measured photoelectron intensity as a function of Binding Energy (BE). The BEs of these lines are characteristic for each element, and are a direct representation of the atomic orbital energies. Published tables of photoelectron BEs for all elements can be used to assist in the assignment of peaks in XP spectra [104,105].

In this Thesis XPS measurements were used to study the surface chemical composition of differently processed CeO_2 films on YSZ single crystal substrates.

Survey spectra were firstly recorded in the range of binding energy of 1200-0 eV, to identify the elements present in each sample (see Fig. 2-7). Then the photoelectron peaks of O(1s), C(1s) and Ce(3d) were recorded with higher resolution, all measured with unmonochromatized Mg K_α X-rays (20mA, 12 kV) with the hemispherical electron energy analyzer working in the constant pass energy mode, at ΔE=50eV, and a step size of 100meV. Gd-doped CeO_2 films will be also registered by Al K_α X-rays source (1486.6 eV). Gd(3d) emission spectra appears at a binding energy higher than 1200 eV and MgK_α is not sufficiently energetic (1253.6 eV).

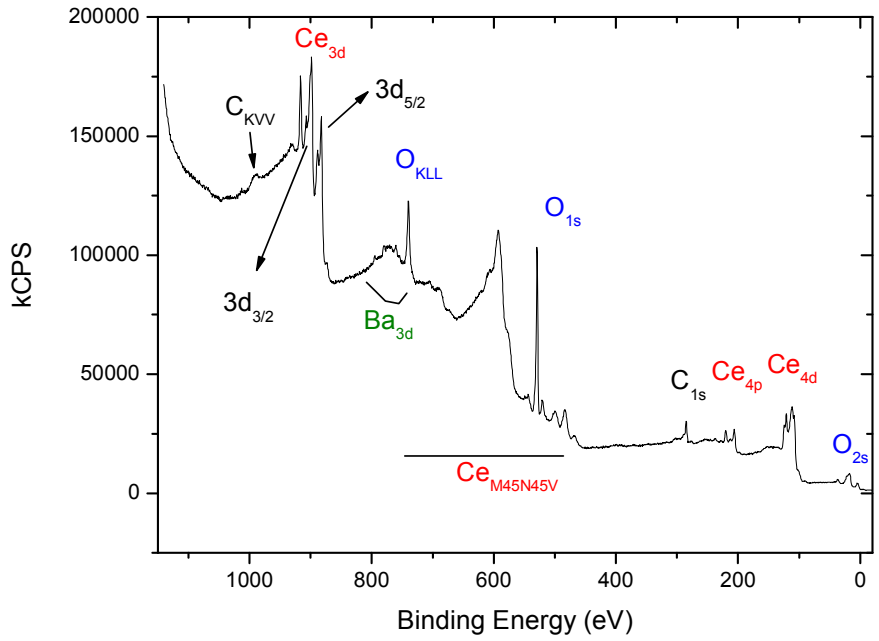

Fig. 2-7 Typical general XPS spectrum of sputtering-CeO_2 film on YSZ (100) single crystal.

All photoemission peaks were recorded many times, to improve the signal to background ratio.

The interpretation of the Ce(3d) photoemission spectra is not straightforward. Multielectronic process in Ce^{4+} and Ce^{3+} states could yield to photoemission spectra with more than 10 peaks. This produces an extremely complicated spectrum with overlapping peaks if both oxidation states are present, shown in Fig. 2-8. Fig. 2-8(a) describes the features for a CeO_2 fully oxidized, while Fig. 2-8 (b) shows the characteristic features for a fully reduced ceria, which corresponds to a Ce_2O_3-like composition. Thus, the assignments of Ce(3d) peaks and the reference values for their binding energies have been a subject of intense research [106,107].

It has been reported in the literature that x-ray induced reduction of CeO_2 after long exposure to the X-ray source of spectrometer [108]. However, in our experiments, spectra were always acquired within the minimum time required to get an optimum signal to noise ratio and no change in the shape of the spectra was observed during the acquisition time.

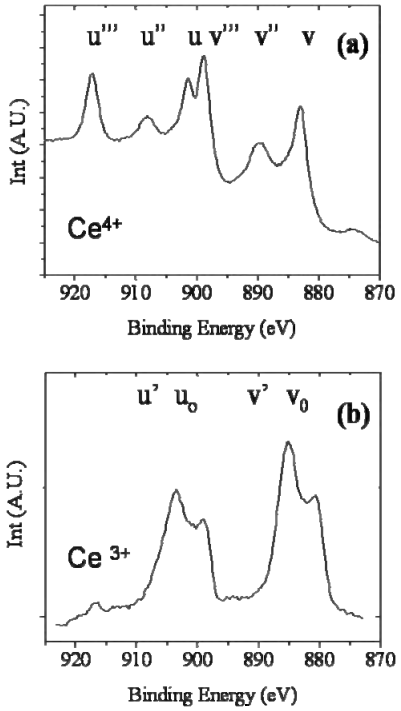

Fig. 2-8 (a) Ce3d spectrum of well- oxidized ceria close to CeO_2. (b) Ce3d spectrum of reduced ceria, close to Ce_2O_3 [109]

2.1.3.1.1 Sample charging

When insulating materials are irradiated by X-rays they quite often develop a static charge due to their inability to replace the photo emitted electrons. This charging can be substantial, say 2-5 eV, but it is always positive and quite small in comparison to electron – induced Auger Electron Spectroscopy (AES) where charging can be of the order of several hundred eV. In our samples surface charging occurred during the photoemission process, and calibration of the binding energy scale had to be made in all cases.

For this purpose, in our CeO_2 samples, the highest binding energy satellite of the $Ce(3d)_{5/2}$ spectra, the peak singed u''' according with the nomenclature of Burroughs et al. [110], has been located at 917.0 eV (BE). This peak, which is due to Ce^{+4} oxidation state, has been chosen for energy calibration because it is present in all the spectra of the studied series of samples, and it is quite symmetric and narrow.

2.1.3.1.2 Chemical shifts

As with a technique such as nuclear magnetic resonance (NMR), XPS can distinguish between particular elements in different environments. This is due to the fact that placing a particular atom in a different chemical environment, or a different oxidation state, or in a different lattice site, etc., gives rise to a change in BEs of the core-level electrons. This BE variation is called the chemical shift, and appears as a shape modification of the elemental peak in the XP spectrum. These will be of substantial aid in determining the chemical environment of an element from a given XP spectrum.

2.1.3.1.3 Quantitative analysis

One of the major advantages of XPS is the ease with which quantitative data can be routinely obtained. This is usually performed by determining the area under the peaks and applying previously-determined sensitivity factors.

In this Thesis we have studied the chemical surface composition of CeO_2 system with the aim to quantify Ce^{3+} and Ce^{4+} content. Due to the complexity of the Ce(3d) spectra, it is difficult to determine by simple area inspection the percentage of Ce^{3+} involved in each sample. Several methods have been proposed for an accurate quantification of the percentage of each species [111,112]. For our aim, we used a quantitative approach in which all necessary basic data are integrated peak areas.

The first step of this analysis was to select a reference spectrum and normalize the intensity of all the spectra of these series of samples (and for the three spectral regions: Ce3d, O1s and C1s) to the area of the u‴ satellite peak of Ce3d from the reference spectra. Note that, as the u‴ signal is only due to Ce^{+4} species (see Fig. 2-8), its numerical treatment has normalized the spectra to the content of Ce^{+4} in each sample. Then, pure Ce^{4+} spectra has been subtracted at each normalized spectra resulting Ce^{3+} contribution. Finally, Ce^{3+} is given respect of the total cerium (Ce^{3+}+Ce^{4+}) from the reference spectrum.

It has been also estimated the atomic composition of other elements present in our samples, i.e. C, O, Ce and eventually Zr and Gd. Since for these elements the spectrum is not as complex as Ce3d, its quantification can be done by determining the area under the peaks as we mentioned above. The first step in quantifying a spectrum is defining the energy regions of the elements that will be studied. The positioning of the cursor to select the energy regions have to be identical for each sample. Then using a Shirley base line and the following sensitivity factors (for MgK_α source): Zr3d:1.70, Gd3d5/2: 12.93, Ce3d:12.06, O1s: 0.66 and C1s=0. 25, software package Eclipse calculates the relative percentage of atomic concentration of elements selected.

If one element has different environments, the peak structure will be multicomponent. Fig. 2-9 shows C1s XPS spectrum which exhibits three components: carbonate, hydrocarbons and carbide. Fitting these components using Gaussian-Lorentzian mixed function it is a useful tool to determine the ratio of each component present in our sample.

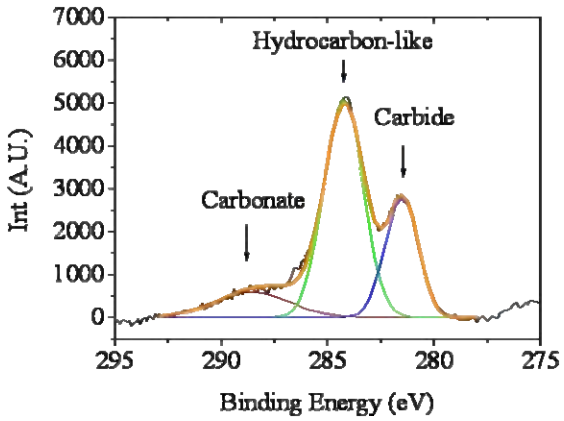

Fig. 2-9 C1s XPS spectrum after curve fitting.

2.1.4 Scanning electron microscopy (SEM)

SEM images were made using a JEOL JSM-6300 SEM in the 'Servei de Microscopia Electrònica' at UAB. Attached to JEOL SEM there is an energy-dispersive X-ray diffraction (EDX) from LINK ISIS-200 of the Oxford Instruments company. A PC interface allows the instrument to be easily operated.

For routine analysis, I have used the Philips-SEM 515 located at 'Institut de Ciència de Materials de Barcelona' ICMAB.

The standard SEM is the most useful electron optical system for surface imaging, and will be applied routinely to characterize all surfaces of YBCO film fabricated in this thesis.

The energy of the incident electrons can be as low as 100 eV or as high as 30 keV. The beam can be focused to a final probe diameter around 10 nm. We have worked in four magnifications - 503×, 2020×, 6200× and 10000×. No sample preparation is required in our case since the YBCO films once oxygenated are electrically conducting. So the films were just placed in the specimen stage of the SEM. In the case of some bad conducting films, it would be necessary to coat them with a thin conductive layer such as gold.

When an electron is incident on the surface of a thick specimen *t*, several signals can be detected. The primary electron results in ionization of atoms along its path in the solid, which in turn can result in the ejection from the surface of secondary electrons, very close to the incident beam position. These have energies from 0-20eV, and can be attracted to a positively charged detector with high efficiency.

Secondary electron images have been obtained identifying surface features. Despite the considerable depth of penetration of the incident primary electron beam, the re-emitted electrons (as secondary and backscattered electrons) come from mean depths of 50nm-0.5μm depending on the density of the material. The surface features in this size range include extensive faceting, phase separation, morphology of crystals, precipitates and pores [113].

2.1.4.1 Energy dispersive X-ray spectrometry (EDX)

Most X-rays energy dispersive analysis systems are interfaced to SEMs where the electron beam serves to excite characteristic X-rays from the probed area of the specimen. Peaks at energies characteristic of the elements within that area can be identified and the concentrations of the elements can be calculated. Thus the bulk composition of the sample and of the individual grains in a polycrystalline sample can be determined for comparison with surface analytical data.

The dimension of the interaction volume depends on the mean atomic number and the density of the material, and on the beam energy and the emitted X-ray energy. Diameters range from 30nm to several μm [114]. Thus conventional EDX spectrometry will not reveal compositional changes due to surface segregation. It is possible however, by analyzing point at several different beam energies, to determine the thicknesses and composition of layers on substrates. And hence determine the composition of this surface layers [115]. However, quantitative analysis of an element in a multicomponent matrix is a complicated matter yield.

2.2 Film characterization

2.2.1 X-ray diffraction analysis (XRD)

Rigaku Rotaflex RU-200BV diffractometer with Cu-K_α λ =1.5418Å was used to carry out ordinary θ-2θ and ω-scan analysis at ICMAB whereas four circle diffractometer Philips PW 3710 MRD Control diffractometer with Cu-k_α λ= 1.5418 Å located at the 'Serveis Científico Tècnics de la Universitat de Barcelona' was used for texture analysis.

Pole figure images presented in this Thesis were registered in IFW-Dresden using Philips X'Pert PW3040 with Cu-k_α radiation.

This is a very important experimental technique to address all issues related to the crystal structure including lattice constants and crystallography, identification of unknown materials, orientation of single crystals and preferred orientation of poylcrystals defects, stresses, etc.

A given crystal can be decomposed into any number of different plane configurations separated by a constant parameter *d* (Bragg plane), due to the periodicity of the crystal lattice. It was found that in these crystals, as a response of X-ray radiation for certain incident angles, intense peaks of reflected radiation were produced if these reflections interfered constructively. This gives the formula for what is known as the Bragg condition or Bragg's law:

$$2d\sin\theta = n\lambda \qquad \text{Eq. 2-1}$$

where *d* is the spacing of the atomic layers of the crystal, n is the period, λ is the wavelengthand θ the angle of the incoming x-ray beam.

The pattern obtained when the Bragg law is fulfilled can be identified by comparing it with an internationally recognized data base powder diffraction file (PDF) reference patterns.

For the X-ray measurements there exist typically two sorts of machines: the two-circle and the four-circle diffractometers. Depending on the kind of diffractometer, one can vary different angles of the sample and so one can get different information. A schematically view and the nomenclature of the angles can be seen in Fig. 2-10. θ, as already described, denotes the angle of the incoming X-ray beam and ω the one of the outgoing beam. ϕ denotes a rotation around the normal of the sample surface and Ψ is a rotation around an in-plane axis of the film.
The experimental X-ray measurements used in this Thesis are :
– θ-2θ scan was performed in the normal Bragg-Brentano geometry in a maximum range from 20 to 80 degrees. The 2θ angle of each diffraction peak of the XRD pattern is characteristic of the interplanar distance *d* in the material, and therefore, the diffraction pattern generated allows determining the chemical compound or phasing composition of the film, the texture of the film (preferred alignment of crystallites), the crystallite size and presence of film stress. In this Thesis we also used XRD θ-2θ scan to quantify phases or epitaxial fractions, since peak intensity of 2θ reflection depends on the volume of phase fraction. To do that, we have calculated the peak area of the reflection in 2θ scan corresponding to the phase we are interested in, and then, it has been compared to reference specimen.

-rocking curve (ω-scan) measurements were made by doing a θ-scan at a fixed 2θ angle. It measures a single Bragg reflection, for example (005) for $YBa_2Cu_3O_7$ film,(200) for CeO_2 film., (200) for $SrTiO_3$ and (200) for $BaZrO_3$ film. This measurement gives valuable information about the orientation spread of the sample. The FWHM permits to detect the degree of out-of-plane texture of the sample.

-phi-scan (ϕ–scan) provides information about the in-plane texture of the film. The relation between the peaks appearing for the substrate and the film shows the in-plane epitaxy of the film.

-pole-figure measurements allow to determine the orientation distribution of crystalline grains in one crystallographic direction. A pole figure is measured at a fixed scattering angle and consists of a series of ϕ-scans (in-plane rotation around the center of the sample) at different tilt or -Ψ angles. Since the pole figure is often plotted in polar coordinates, can reveal oriented crystalline populations not seen in θ-2θ scans as well as the fraction of randomly arranged crystallites. A material is termed textured if the grains are aligned in a preferred orientation along certain lattice planes.

- area scan: the motion of the detector (2θ) and the rotation of the goniometer (ω) angles are scanned. Both angles, θ and ω are then swept within a given range. From this measurement we obtain information about in-plane parameters without the need of moving the Ψ circles.

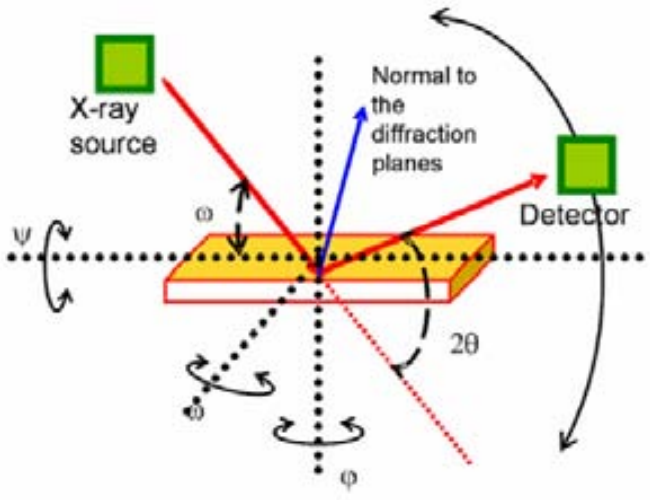

Fig. 2-10 Schematic view of the goniometer and the four angles [116].

2.2.2 Transmission Electron Microscopy (TEM)

The TEM images and electron diffraction patterns were made by using a Philips CM30 TEM while HRTEM images patterns were made by using a JEOL 1010 electron microscopes operated at 200kV (point to point resolution 0.19 nm) equipped with a Gatan Image Filter 2000 EELS spectrometer with an energy resolution of 0.8 eV in the 'Serveis Científico-Tècnics de la Universitat de Barcelona'. The EELS spectrometer allowed us to perform quantitative element analysis.

TEM has been the technique most widely used to study the internal microstructure and crystal structure of samples (YBCO, CeO_2, STO and BZO) as well as for the observation of dislocations and other crystal defect. TEM is applicable to a wide range of materials, subject only to the conditions that specimens can be prepared in very thin section and that they remain stable when exposed to a beam of high-energy electrons within a high vacuum [117].

With transmission electron microscopy (TEM), a thin (< 100 nm) sample is bombarded by a highly focused beam of single-energy electrons. The beam has enough energy for the electrons to be transmitted through the sample. The transmitted electron signal is greatly magnified by a series of electromagnetic lenses up to atomic resolution. The magnified transmitted signal can be observed in two ways, through electron diffraction or direct electron imaging. Electron diffraction patterns were used to determine the crystallographic structure of material phases. Direct electron images yield information about the microstructure of these phases, their grain orientation and size [118].

2.2.3 Superconducting and electrical properties

2.2.3.1 SQUID magnetometer

Critical current density of our TFA-YBCO films was measured with two Quantum Design SQUID (Superconducting Quantum interference Device) magnetometers provided with a 5.5T and 7T superconducting coils. Most of the analysis has been done by determining the temperature dependence of J_c. For that purpose we saturate the magnetic moment of the sample at 5K by applying a constant magnetic field (3T) that is then removed in order to measure the remanent magnetic moment at different temperatures (from 5 to 93K). J_c values at zero applied field are obtained by applying the Bean Model [119],

$$J_c = \frac{3M}{R} \qquad \text{Eq. 2-2}$$

where M is the value of magnetization and R the radius of the sample.

2.2.3.2 Electrical resistivity

The most common method of measuring the thin film resistivity is with the four-point probe. The sample resistance has been determined by measuring the voltage drop when a given current flows in the film. To avoid the patterning of the film we have performed the measurements by using the van der Pauw method [120]. Resistivity measurements were performed by lifting the sample holder away from the liquid nitrogen surface. Sample temperature is continuously monitorized and a measurement event is triggered if the temperature has changed within a given ΔT. We have kept $\Delta T < 0.1$K to ensure that the measurement is performed in a warming up mode.

The measurements require that four ohmic contacts be placed on the sample: P, O, M, N, see Fig. 2-11.

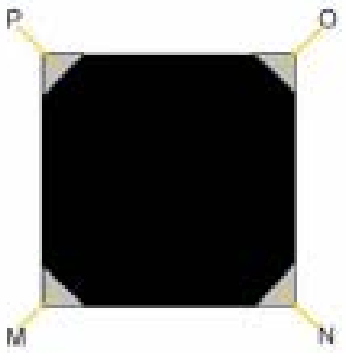

Fig. 2-11 Sketch of one possible contact placement to use the van der Pauw method.

It can be demonstrated that exist a relationship between Eq. 2-3 and Eq. 2-4 given in Eq. 2-5.

$$R_a = \frac{V_p - V_o}{i_{mn}} \qquad \text{Eq. 2-3}$$

$$R_b = \frac{V_m - V_p}{i_{no}} \qquad \text{Eq. 2-4}$$

$$\exp\left(-\frac{\pi d}{\rho} R_a\right) + \exp\left(-\frac{\pi d}{\rho} R_b\right) = 1 \qquad \text{Eq. 2-5}$$

where R is the resistance, V the voltage and i the injected current. Since d (film thickness) is know, Eq. 2-5 can be easily solved and we figure out the resistivity value (ρ).

2.2.4 μ-Raman Spectroscopy

Micro-Raman measurements were carried out using the 5145 Å line of an Argon-ion laser from Spectra Physics at room temperature with a Jovin-Yvon T-64000 Raman spectrometer attached to an Olympus microscope and equipped with a liquid-nitrogen-cooled CCD detector. The used laser spot size on the sample was ~ 1 μm. Raman spectra were recorded in backscattering geometry.

The Raman scattering is the inelastic scattering of electromagnetic radiation (photons) creating (Stokes process) or annihilating (anti-Stokes process) an elementary excitation in the solid. The anti-Stokes process can occur only if the crystal is initially in an excited state. The elementary excitations can, among others, be phonons, plasmons, excitons or spin fluctuations. It therefore provides a fingerprint by which the molecule can be identified. This technique allowed us to identify secondary phases present in YBCO film as well as the fracion of c-axis oriented YBCO grains [121]. The spectral range used for the characterization of YBCO films was between 200–600cm^{-1}. This spectral range was enough to characterize, analyze and study YBCO films by the phonon Raman modes of O(2, 3) and O(4) oxygen atoms. O(2,3) mode is related to the oxygen content in Cu-O planes whereas O(4) mode is related to the apical oxygen (See Fig.1-1).The ratio between those modes is a function of c-axis fraction of YBCO grains.

2.2.5 Inductively coupled plasma (ICP)

ICP measurements were performed in a Thermo Elemental (model PQEXcell, Windsford, UK) located at the 'Universitat Autònoma de Barcelona'.

The stoichiometry of the YBCO precursor solution is a parameter that should be controlled since it can dramatically influence the final superconducting and microstructural properties of the film. ICP allowed us to obtain a quantitative determination of multi-elements at trace and ultra-trace concentration levels.

Samples submitted to ICP analysis must be fully prepared and should match the acidity and background matrix of the calibration standards. Indeed, our original solution which is estimated to be 1.5M has to be diluted in order that the final metal concentration is in the range of 0-100 ppm.

2.3 Precursor solution characterization

2.3.1 Thermal gravimetric analysis (TGA)

These measurements were performed using a Thermobalance Perkin Elmer TGA7 with a sensibility of 0.1 μg. The experiments have been carried on in alumina crucible under a flux of 7.5 $x10^{-2}$ l min^{-1} of oxygen or Ar/H_2 atmosphere.

Thermal analysis, in particular, thermogravimetric analysis (TGA)[122], allowed us to obtain information about weight changes in sample materials as a function of temperature or time.

We performed this analysis on buffer layer precursors in order to optimize the heating profile to obtain crack-free and homogeneous films in a relatively short time. Through a computer controlled graphics we could calculate weight percent losses of a dry precursor solution with increasing temperature in either Ar/H_2 or O_2 atmosphere.

For this particular instrument, the specimen should be powder as dry as possible and samples containing fluorine are not accepted.

CHAPTER 3

Experimental procedure

In this chapter we describe the preparation of $YBa_2Cu_3O_7$ (YBCO) films and $BaZrO_3$ (BZO), $SrTiO_3$ (STO) and CeO_2 buffer layers by chemical solution deposition. Among the different chemical methods to fabricate 'all-chemical' coated conductors, YBCO and buffer layers were prepared by the metal organic decomposition method (MOD). This method has demonstrated major advantages, taking into account its versatility and low cost, as mentioned in section 1.2.3.1. In particular, YBCO films preparation is based on trifluoroacetate (TFA) precursors (1.2.3.1.2).

Understanding and controlling the deposition of the metalorganic precursor and its conversion to YBCO are critical to reproducibly manufacture uniform, high-performance, HTS wires required for commercial applications. This chapter describes the preparation procedure followed to obtain both high quality YBCO and buffer layer film carried out on single crystalline substrate as a model system.

When YBCO or buffer layers growth are carried out on different substrates or buffer layers, modified conditions are explicitly described in the corresponding chapters.

3.1 YBCO superconducting layer preparation by the TFA route

As we introduced in Chapter 1 there are many process for making YBCO superconducting films (see 1.2.2). Among them, TFA-YBCO appears to have a very high potential for achieving the required goals in terms of cost and performance for coated conductor applications [12,123]. Metalorganic decomposition of YBCO films involves four steps: (1) precursor solution synthesis, (2) coating, (3) decomposition, and (4) growth. The final films must meet stringent requirements, including high critical current, uniformity across the width and along the length of the textured substrate. In order to achieve these properties the development of a metalorganic precursor that produces an intermediate BaF_2-based film, which in turn is converted to a high-quality YBCO films after a growth process, has been required in the scientific community.

3.1.1 YBCO Precursor solution

In the MOD methods, various precursors such as acetates, citrates, oxalates, neodecanoates, trifluoroacetates, halides, acetylacetonates, and naphtalenates have been described in the literature to fabricate YBCO films [124,125,126,127,128]. To date, best results have been obtained using trifluoroacetates precursors and therefore, in this thesis we have investigated two routes to obtain TFA-YBCO precursor solution.

Firstly, we prepared a TFA-precursor solution starting from the separate metal-salts. This is a long procedure and can lead often to a non stoichiometric final solution because of problems with solubility and contamination (i.e. substantial amounts of water (>2% in weight)). As a result, it gives final oxide films with a substantial decrease in superconducting properties. To overcome these problems, it was developed an improved and purified route starting from commercial stoichiometric YBCO powder. Moreover, this process allowed us to considerably reduce the length of the precursor preparation process.

3.1.1.1 Preparation method of TFA solution from separate salts

The preparation of YBCO precursor solution was carried out at room temperature, using as starting materials $CuCl_2$ (RP), $BaCO_3$ (Diopma, 99.9% purity) and commercial $Y(CF_3COO)_3$ (Aldrich).

$Cu(CF_3COO)_2$ solution was prepared by reacting $CuCl_2$ partially hydrated powder with NaOH 1M forming $Cu(OH)_2$. This gel is repeatedly washed with de-ionized water to clean trapped chlorides from the starting material. $AgNO_3$ was added in the washings to verify that chlorides have been completely eliminated. Finally, the gel was washed with dry methanol and dissolved with small amount of trifluoroacetic acid (TFAH),

$$CuCl_{2(s)} + 2\ NaOH_{(aq)} \rightarrow Cu(OH)_{2(s)} + 2NaCl_{(aq)} \qquad \text{Eq. 3-1}$$

$$Cu(OH)_{2(s)} + CF_3COOH_{(l)} \rightarrow Cu(CF_3COO)_{2(l)} + H_2O_{(l)} \qquad \text{Eq. 3-2}$$

It is important to keep an acid pH, otherwise $Cu(CF_3COO)_2$ easily forms insoluble basic salts. Therefore an acid was added to $Cu(OH)_2$. This reaction can be schematized as follows,

$$Cu\ (CF_3COO)_{2\ (l)} + CH_3OH_{(l)} \rightarrow CF_3CO_2CH_{3(l)} + CF_3\ CO_2\text{-}Cu\text{-}OH_{(s)} \qquad \text{Eq. 3-3}$$

For the $Ba(CF_3COO)_2$ precursor, $BaCO_3$ was dissolved in a mixture solution of de-ionized water and CF_3COOH (1:2) after stirring and heating a couple of hours.

$$BaCO_{3(s)} + CF_3COOH_{(l)} + H_2O_{(l)} \rightarrow Ba(CF_3COO)_{2\ (l)} + CO_{2\ (g)} + H_2O_{(l)} \qquad \text{Eq. 3-4}$$

Finally, to obtain $Y(CF_3COO)_3$ precursor solution, $Y(CF_3COO)_3$ commercial powder was dissolved in acetone.

Then, the appropriate volume of the three metal TFA precursor solutions were mixed to give a final blue precursor solution with total metal ion concentration of 1-1.5 M. This solution was kept in sealed vials, in an inert atmosphere. The flow chart of synthesis of precursor Cu, Ba and Y TFA salts is presented in Fig. 3-1. From inductively coupled plasma analysis (ICP) a defect of copper content was detected. Then, in the group an alternative route starting from stoichioimetric powder was developed to improve this one.

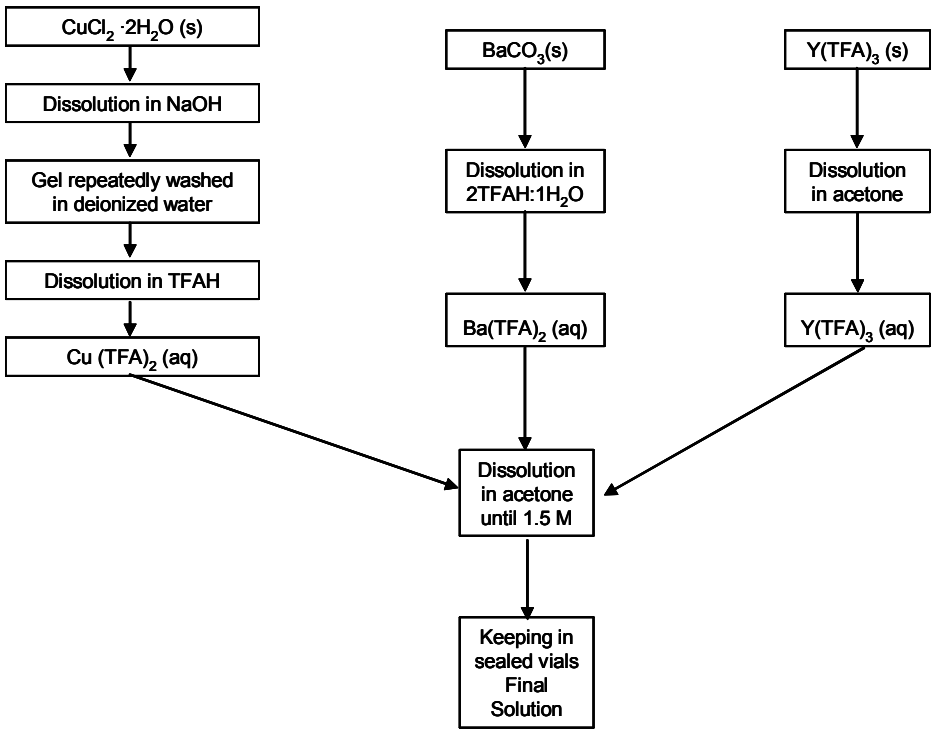

Fig. 3-1 Flow chart of synthesis of YBCO precursor solution with $CuCl_2$, $BaCO_3$, $Y(CF_3COO)_3$ as starting reactants.

3.1.1.2 Preparation method of TFA solution from stoichiometric YBCO powder

The preparation of YBCO precursor solution was performed in an inert atmosphere. It consists of the dissolution of YBCO powder (yttrium barium copper oxide, Solvay) in an excess of TFAH (Aldrich 99%), as solvent. The mixture was stirred and heated at 50ºC for 72 h. The resulting solution is filtered and evaporated under vacuum. The mixture of TFA salts ($Ba(CF_3COO)_2$, $Cu(CF_3COO)_2$ and $Y(CF_3COO)_3$) was then dissolved in sufficient anhydrous methanol (Aldrich 99.8%) or distilled acetone to give a blue solution with total metal ion concentration of 1.5M. However, the synthesis of the trifluoroacetate salts from trifluoroacetic acid produced substantial amounts of water which results in a significant decrease in their superconducting properties. It has been suggested that fluorine atom from trifluoroacetates, which has a strong electronegativity, forms a strong hydrogen bond with hydrogen atom from water. Therefore, it was required a repetitive and long purification process [129,76].

Then, as an alternative route to reduce water content of the precursor solution in the above described preparation method, trifluoroacetic acid was replaced by trifluoroacetic anhydride (TFAA), because it gives highly stable solution and with very low water content (less than 100 ppm of water (0.01% in weight))[130].

This solution is kept in sealed vials, in an inert atmosphere. Fig. 3-2 shows a diagram of the steps to be followed for the synthesis of the TFA solution. The metal stoichiometry was checked

by ICP analysis. The metals were present in the following ratio (Y:Ba:Cu) (1:2 ± 0.05:3 ± 0.05).The viscosity of the 'anhydrous' solution (3.5 ± 0.5 mPa s) was controlled and its stability was demonstrated by viscosity measurements over time.

With 'anhydrous' TFA solutions it is possible to notably reduce the required purification time and these purified solutions also allow shortening the pyrolysis time very significantly (from 24h down to 1.5h) to achieve high quality superconducting films [34] .

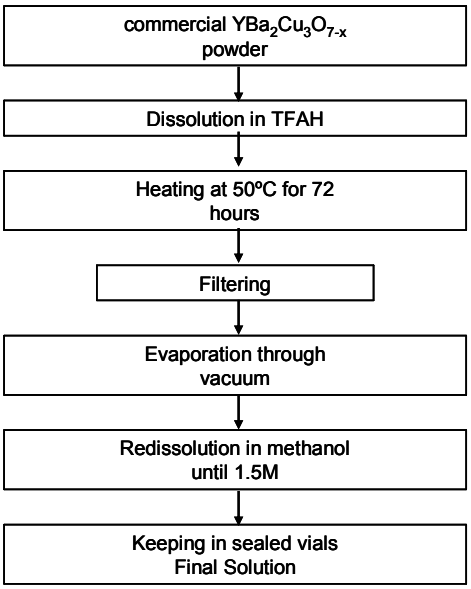

Fig. 3-2 Flow chart of synthesis of YBCO precursors from stoichiometric powder.

3.1.2 Gel deposition

Substrates were cleaned in successive ultrasonic baths of acetone and metanol lasting 10 minutes. The substrates were quickly dried with compressed pure nitrogen.

14 μl of the precursor solution were disposed on the underlying layer by a Pyrex microsyringe.

The spin rate is ramped from zero revolutions per minute (rpm) to 6000 rpm in about 1 second. This spin rate is held for 2 minutes and then is decreased to zero rpm. Spin coating was performed at ambient temperatures in the range 18-23ºC and relative humidity between 27-37% which corresponds to an absolute humidity below 9 gm^{-3}. Deposition step has to be well controlled in terms of atmosphere to avoid any inhomogeneities in the layer otherwise superconducting properties are dramatically affected. Then, the samples were fired in two stages

(pyrolysis and high temperature heat treatment) in a tubular furnace. The quartz tube has a diameter of about 25 mm.

3.1.3 Pyrolysis

Pyrolysis is performed to remove excess solvent (e.g., water and methanol) and carbon content from the as-deposited film and to decompose the metalorganic molecules to form nanocrystalline CuO and Ba-F-Y matrix [71].

Pyrolysis parameters were optimized for each TFA-YBCO precursor solution. For separate salts precursor solution the films were pyrolysed by the well established long process (~ 24h) described by Gupta et al. [32] (see Fig. 3-3 (a)). On the other hand, for stoichiometric anhydrous TFA solution a short process lasting only 1.5 h was developed, Fig. 3-3 (b). We have not detected any film property degradation when this process is shortened [130,84].

Most of the samples presented in this Thesis have been pyrolysed following the short process. In it, the as-deposited film was slowly heating to ~ 300-400ºC, in a humid oxygen atmosphere to suppress the sublimation of Cu trifluoroacetate [131]. The flow of humid oxygen was injected into the furnace once the furnace temperature reached 100 to 120ºC to prevent the gel film from absorbing humidity, which would deteriorate the film integrity. Humid oxygen was maintained until the temperature reached the set temperature at which point, set temperature was held for 30 minutes and then slow cooling down to 150ºC where furnace power were shut off and dry oxygen was injected to room temperature.

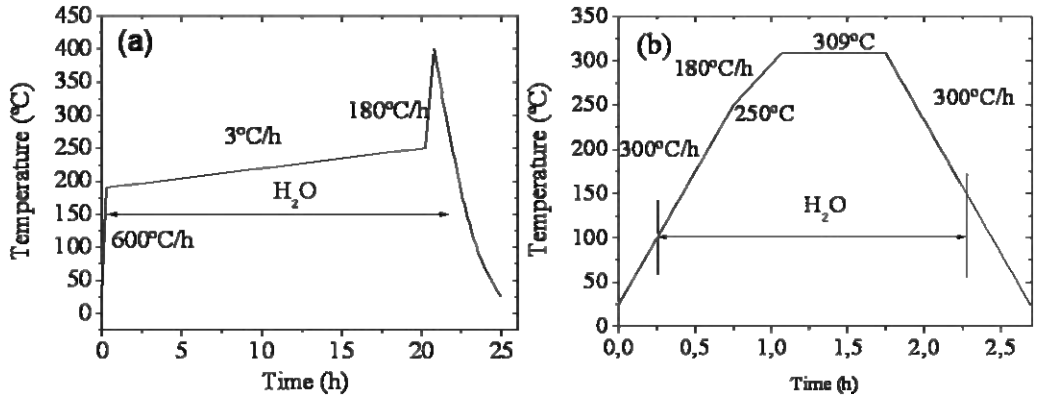

Fig. 3-3 Heating profile for the initial calcinations used to decompose the metal TFA precursor films synthesized (a) by separate salts (b) by stoichiometric YBCO powder. Dry gas is introduced below 100ºC to avoid adsorption of water vapour into gel film. Humidified gas above 100ºC partially hydrolyzes Cu trifluoroacetates to avoid its sublimation.

Humid oxygen gas flow was obtained by passing dry ultrahigh-purity oxygen through de-ionized water contained in two large flasks in series, prior to entering the furnace. The two large flasks were contained in a water bath at 20ºC to obtain the desired 2.2 kPa water partial pressure. The water level in the flasks was maintained at approximately two-thirds full.

Oxygen was injected into the flasks at a flow rate in the range of approximately 0.085-0.1 $lmin^{-1}$ using gas dispersion tubes.

Pyrolysis process has to be well controlled in terms of atmosphere, temperature rates, and time to avoid any inhomogeneities in the layer (cracks, buckling) [34]. Recently, in our group it has been widely investigated this complex process combining FTIR, TGA and film thickness evolution measurements [84]. It has been identified three different characteristics temperature regions: low temperature (T<200-250ºC) where TFA gelified film is transformed through a drying-sintering process but the TFA precursors are essentially not decomposed. An intermediate temperature region (T~250-310ºC) where TFA precursors are decomposed and most of the film shrinkage occurs (final film thickness ~30% of the initial one) through a viscoelastic process which strongly hardens the film and thus generates a strong in-plane tensile stress. Temperature ramp and external gas flow have been modified in order to achieve a smooth stress relief resulting a final pyrolysed film shown in Fig. 3-4(a). Otherwise if film shrinkage process is too fast the films turn out to be buckled and these anomalous structures strongly degrade the film epitaxy and the superconducting properties after high temperature growth. Fig. 3-4(b) shows a buckled film pyrolysed under too high temperature rate. It is important to remark that pyrolysis conditions have to be readjusted depending on the underlying buffer layer or substrate.

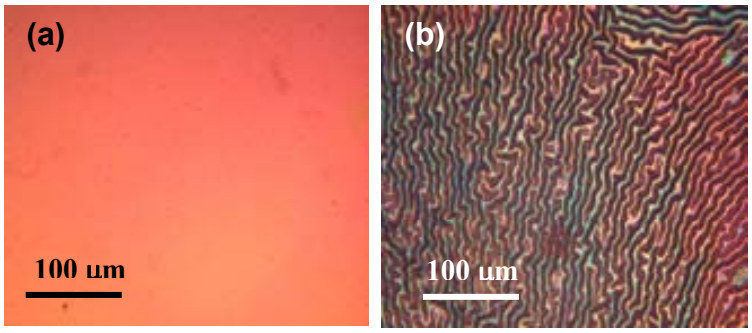

Fig. 3-4 Optical micrographs of calcined films after a short pyrolysis process for (a) film which has been preserved their homogeneity (b) a buckled film.

3.1.4 High temperature heat treatment

In a second step the metastable state created after the pyrolysis is converted to superconducting YBCO film following the heating profile proposed by McIntyre et al. [132], and optimized by us [99], see Fig. 3-5.

Initial dry purge was performed to eliminate gas impurities inside the furnace near the sample. Pyrolysed films were heated to 700-800ºC at 1500ºC/h, in humid N_2 gas mixed with 0.1-0.02kPa oxygen, and was held at that temperature 3 hours (2.5 hours in humid atmosphere and half an hour in dry atmosphere). Then, it was annealed at 450ºC with dry oxygen for 3.5 hours to form YBCO with superconducting properties. Furnace atmospheres used for annealing the YBCO thin films were saturated at 0-25ºC dew point ($P(H_2O)$= 0.6-2.2kPa). Water vapour was introduced into the furnace at 100ºC by bubbling the incoming gas through an attached reservoir, consisting of a two flasks connected in serie of de-ionized water or ice, depending on the run dew point.

Low oxygen partial pressure furnace atmosphere for the high-temperature heat treatments were prepared using mass flow controllers to mix ultrahigh-purity nitrogen with analyzed oxygen/nitrogen gas mixtures.

The total flow rate of gas through the furnace was kept in the range of 0.6 $lmin^{-1}$, while the total pressure can be 1.01x 10^5 Pa.

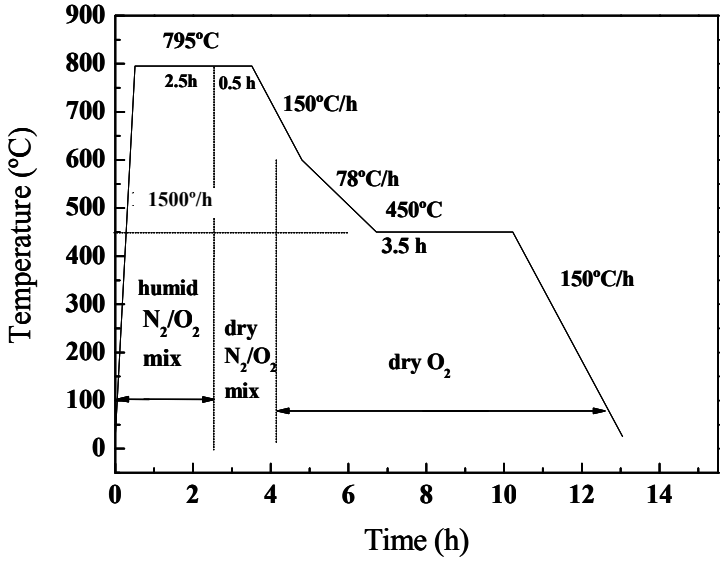

Fig. 3-5 Heating profile for the high-temperature anneal of TFA-YBCO on LAO single crystal. Humidified gas is introduced at 100ºC. 0.02kPa oxygen mixed gas is used in the firing profile with a maximum temperature of 795ºC.YBCO film is annealed below 500ºC to become YBCO superconductor.

Once optimal growth conditions are used, epitaxial films of very high quality are achieved on single-crystal substrates, as can be seen in XRD θ-2θ scan from Fig. 3-6. Phase purity and preferred *c*-axis orientation are observed. In-plane and out-of-plane texture from ϕ-scan and ω-scan respectively, demonstrate high quality biaxial texture with Δϕ(102) =1.3º and Δω (005) = 0.5º, Fig. 3-7.

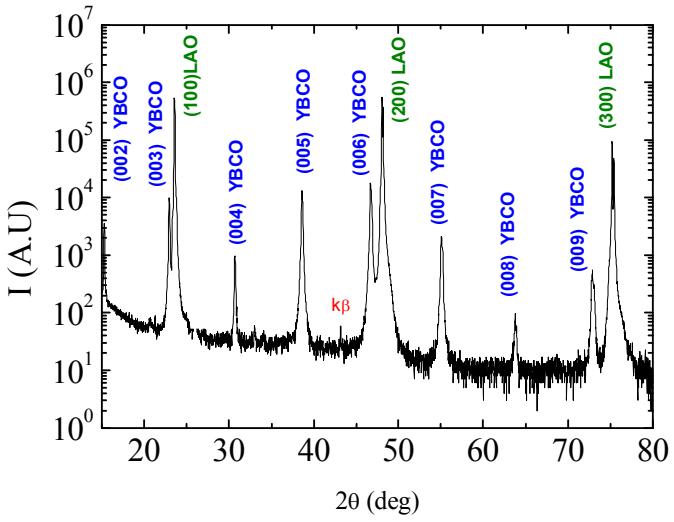

Fig. 3-6 Intensity of YBCO films formed on $LaAlO_3$ single crystal by TFA growth at 795ºC, P(O_2) 0.02kPa and P(H_2O) 0.6kPa.

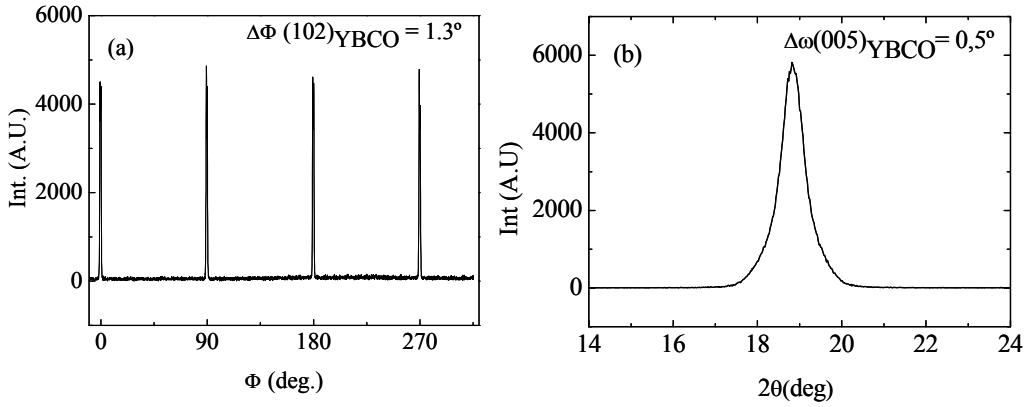

Fig. 3-7 Texture of a typical YBCO film grown at 795ºC, P(H_2O)=0.6 kPa , P(O_2)= 0.02kPa on LAO single crystal (a) (102) reflection ϕ-scan of the YBCO films, (b) (005) reflection ω-scan of the YBCO film

It is worth mentioning that YBCO films is predominantly *c*-axis grain oriented indicated by flat surface with hills and holes in SEM micrograph Fig. 3-8(a). Cross-section TEM observations reveals a sharp interface and film porosity are nearly completely eliminated Fig. 3-8 (b) and (c): hence very high J_c values are achieved (J_c (77K) 3-4 MA cm^{-1}).

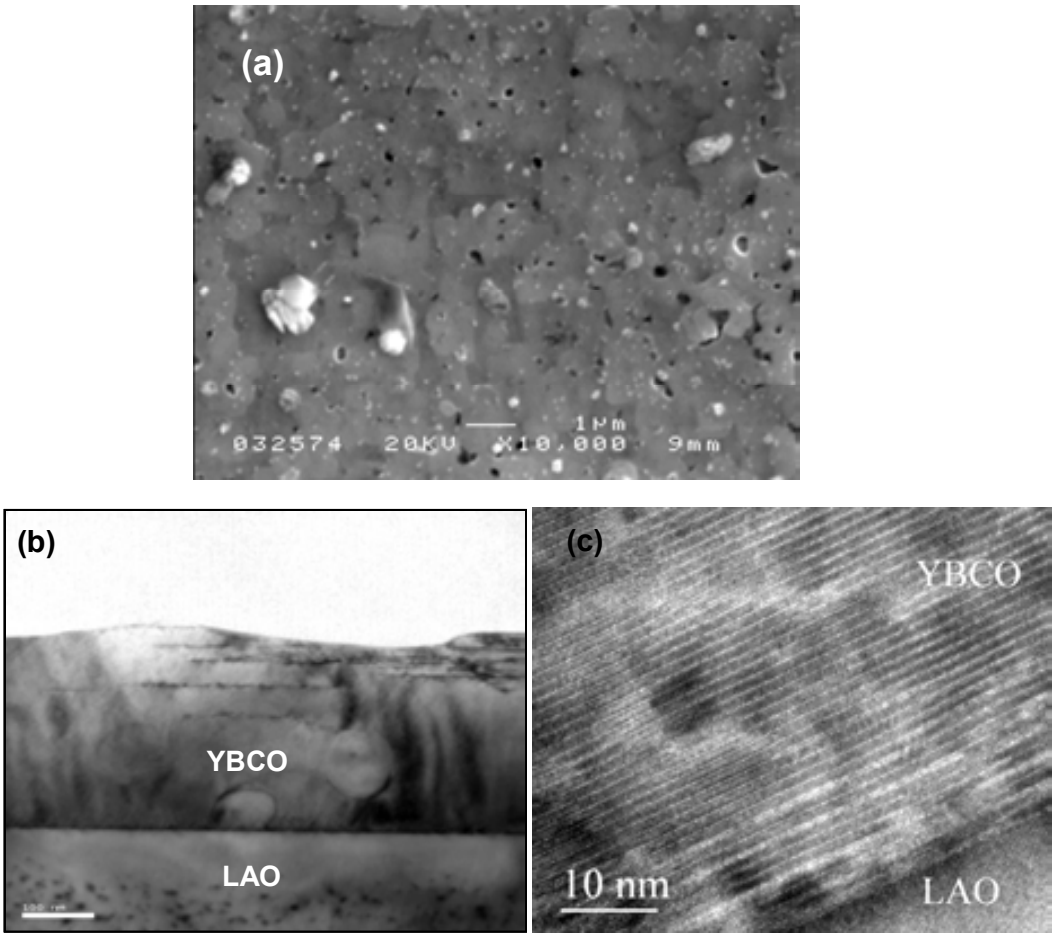

Fig. 3-8 (a) SEM micrograph of TFA-YBCO film (b) Low magnification and (c) high resolution XTEM images of a YBCO film after growth at 795ºC on a LAO single crystal. Note the high crystalline quality of the interface and the low porosity of the films.

3.2 Influence of growth parameters on YBCO microstructure

High quality YBCO films strongly depends on the nature of the substrate because the nucleation process in YBCO films occurs mainly at the substrate interface with the *c*-axis oriented perpendicular to the substrate, see Fig. 3-9, [133]. For this reason the effects of lattice mismatch on heteroepitaxial growth will be strongly discussed in this work. However, nucleation rate and crystal orientation are also influenced by YBCO growth conditions.

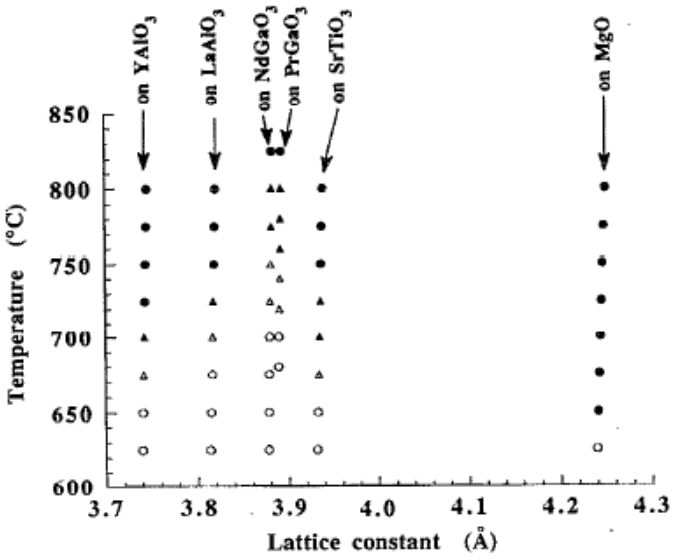

Fig. 3-9 Substrate temperature dependencies of the main orientation axis of YBCO thin films grown on different substrate materials. Solid circles (●), solid triangles (▲), open triangles (Δ), and open circles (○) represent grown thin films that were fully c-, strongly c-, strongly a-, and fully a-axis preferred orientation, respectively [133]

The complex reaction path leading to epitaxial YBCO films, has been investigated by several authors from TFA precursors and from PVD BaF_2 process methodology, but still many critical issues remain controversial and poorly understood. From our TFA precursors this complex reaction was also studied by analyzing by TEM films quenched from growth temperatures and from films completely grown modifying different processing parameters. As we previously introduced in see section 1.2.3.1.4.1 we have defined a microstructural scenario with a competitive nucleation growth between YBCO and $Y_2Cu_2O_5$ phase. Excellent control of YBCO growth involve a good knowledge of the YBCO phase diagram and also the nucleation and growth mechanisms on LAO substrate [134,91,71].

PO_2-T phase diagram is relevant for the initial film composition (oxygen content) and to generate a high crystalline quality (see 1.2.3.1.4.3). It is a well established phenomenon that growth of YBCO films near its stability line leads to an enhanced crystallinity (100% *c*-axis oriented YBCO), and hence, our growth process have been carried out typically in the range of $P(O_2)$ =0.02-0.1 kPa for an optimal growth temperature around 795ºC. Low temperatures or higher $P(O_2)$ favour a-axis grain growth, see Fig. 1-15 [91,90]. In agreement with our results, several authors have been reported that thermodinamically, c-axis oriented YBCO is the preferred growth mode and under conditions of supersaturation, a-axis oriented grains can easily nucleate [135,136]. Due to the anisotropic growth rate of YBCO, a-axis grains grow faster than c-axis grains and reach the upper films surface even before than *c*-axis grains, see Fig. 3-10.

Fig. 3-10 Schematic indicating the transition from thermodynamically preferred $c_{\perp}$ growth to kinetically preferred $a_{\perp}$ growth at high supersaturation [135].

This effect was clearly evidenced in inclined SEM images where a-axis grains were identified as outgrowths emerging from the flat c-axis oriented surface, see Fig. 3-11. *a*-axis growth can be easily distinguished by SEM micrographs by its plate-like shape giving a mosaic pattern, Fig. 3-11(b). The influence of the enhanced *a*-axis grain nucleation will lead to porous microstructure and reduction in J_c values of TFA- YBCO films [99].

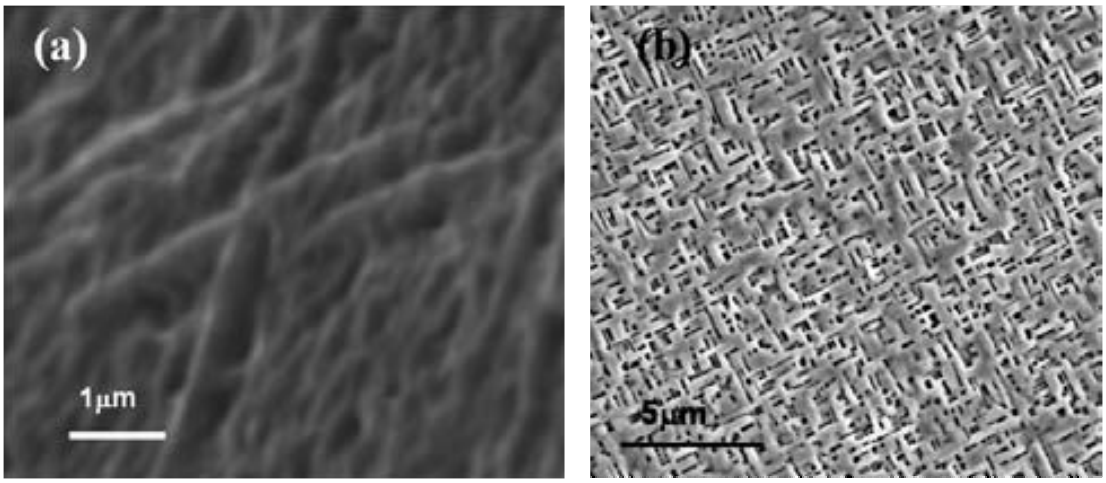

Fig. 3-11 (a)Inclined SEM micrograph shown *a*-axis YBCO grains outgrowth, (b) SEM micrograph of a YBCO film showing all *a*-axis grains growth and the associated pores around them.

When optimal growth temperatures (795ºC) are used, the gas flow rate and $P(H_2O)$ also play a non-negligible role on the film. It was observed that at excessively low gas flow rates or low $P(H_2O)$-values, the YBCO reaction formation is not completed, and inhomogeneous films are formed with trapped non-superconducting phases (unreacted fluorides or oxyfluorides). This entrapping of non-superconducting phases at low growth rate has also been previously observed by other authors [137]. As stated before (section 1.2.3.1.4.2), the YBCO formation reaction generates HF which needs to be eliminated from the growing interface. Therefore, the film growth rate is enhanced when the gas flow rate is increased [138].

In our group we investigated the dependence of $P(H_2O)$ and gas flow on the final quality of YBCO film [99]. We suggested that the degradation of the superconducting properties at low gas flow rates can be assigned to stagnant HF gas blocking the advancement of the YBCO formation reaction. Similar to the gas flow rate case, low $P(H_2O)$ give uncompleted YBCO formation reaction due to insufficient supply of H_2O at the growing interface ($R \propto P(H_2O)^{1/2}$). For higher gas flow rates (2.03×10^{-2} m s^{-1} keeping $P(H_2O)$ at 0.6kPa) the reaction was completed and so a high-quality crystalline structure was evidenced with low porosity, sharp interfaces with the substrate and high critical current. When the gas flow rate or $P(H_2O)$ is too high (>4.8×10^{-2} m s^{-1} or >2.5 kPa respectively), the superconducting performance of the films are found to be degraded. The microstructural or physical origin of this film quality degradation is not completely well established, but μ-Raman spectra suggest that a disordered YBCO structure is generated in both cases [121]. However at high $P(H_2O)$ film degradation is no more evidenced increasing gas flow rate. This indicates that a close relationship exists between processing parameters. A deeper microstructural investigation is required, however, to fully substantiate this phenomenon.

Finally we summarize the recent growth conditions found for optimal TFA-YBCO film quality with 300 nm thickness grown on LAO single crystalline substrate leading J_c (77K) ~3MA cm^{-2}

T= 795ºC

$P(H_2O)$=2.2kPa

Gas flow rate= 2.03×10^{-2} m s^{-1}

t = 180 minutes (150 humid +30 dry)

$P(O_2)$ during growth step =0.02kPa

3.3 Metalorganic Decomposition (MOD) buffer layer preparation

Buffer layers play a key role in YBCO 2G wire technology. The main purpose of the buffer layers is to provide a continuous, smooth, and chemically inert surface for the growth of the YBCO film while transferring the biaxial texture from the substrate to the YBCO. To achieve this, the buffer layers need to be epitaxial to the substrate, that is, they have to nucleate and grow in the same biaxial texture dictated by the underlying film. Buffer layer materials that have been studied in this Thesis are: $BaZrO_3$, $SrTiO_3$ [98,46] and CeO_2 [38,40].

In this chapter we describe the experimental procedure to synthesize the buffer precursor solution as well as the corresponding thermal treatments. Detailed film characterization is given in chapter 5 for perovskite buffer layers (STO and BZO) and in chapter 7 for fluorite buffer layer (CeO_2).

3.3.1 MOD-$BaZrO_3$ buffer layer

The preparation of $BaZrO_3$ (BZO) precursor solution was carried out under atmospheric conditions.

Barium acetate (Aldrich) ($Ba(CH_3COO)_2$) and Zirconium (1,4)2,4-pentadionate (Alfa Aesar) ($Zr(CH_3COCHCOCH_3)_4$) were used as precursor compounds. Because acetylacetone could ionize in aqueous solution as weak acid, ($CH_3COCH_2COCH_3 \leftrightarrow H^+ + CH_3COCHCOCH_3^-$) $Ba(CH_3COO)_2$ and $Zr(CH_3COCHCOCH_3)_4$ are weak acids salts and therefore expected to be soluble in carboxylic acids. By adding 0,153g of $Ba(CH_3COO)_2$ and 0,292g of $Zr(CH_3COCHCOCH_3)_4$ to 4 ml of glacial acetic acid (Panreac), it was obtained after 30 minutes under stirring and heating (at 50ºC), a transparent yellow solution. The concentration of the solution was adjusted to c= 0.3M (total metal ion concentration). The viscosity of the final precursor solution at room temperature was measured using a rheometer (1.72 ± 0.3 m Pa s) and then was kept in sealed vials.

15 μl of BZO precursor solution was deposited by spin coating on a 5 mm x 5 mm $LaAlO_3$ single crystal, supplied by Crystec, previously cleaned 10 min with acetone and 10 min with methanol in an ultrasonic bath. Deposition was performed with a rotation speed of 6000 rpm, rotation time of 2 minutes and an acceleration of 3000 rpm s^{-1}. After spin-coating, samples were heated under 95%Ar/5%H_2 (Ar/H_2) flow in a two-step process. Weight losses measurements (TGA) performed on dry BZO precursor [139] have allowed us to determine the most optimized growth process, to produce crack-free films in a relatively short time. As-deposited film was slowly heated (200ºC h^{-1}) to high temperature, 700-900ºC, in a tubular furnace. Then, it was hold for 4 hours at the set temperature to finally cooled down to room temperature. This optimal heating profile is illustrated in Fig. 3-12.

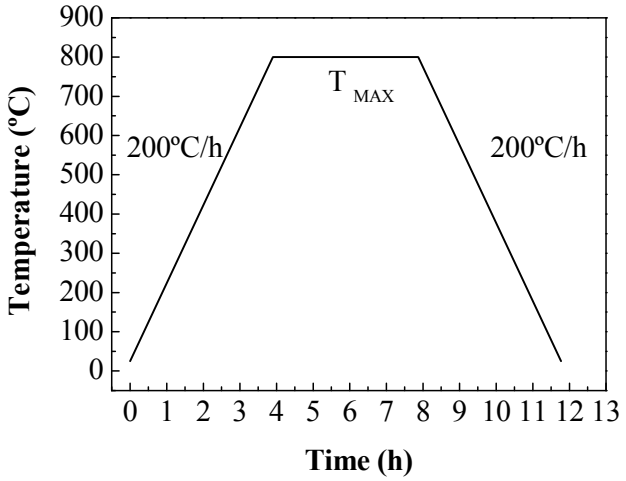

Fig. 3-12 General schema of the preparation procedure of BZO layer growth using Barium acetate and Zirconium (1,4)2,4-pentadionate as starting reactants in glacial acetic acid.

This procedure allowed us to obtain phase purity and (*h*00) oriented BZO observed by x-ray diffraction, first by obtaining θ-2θ patterns and then through ω-and ϕ-scans. Δϕ (202) and Δω (200) are1.8 º and 0.8º respectively even existing a large lattice mismatch between the two perovskite structures, ε=9.5% (see Table1-I).

AFM investigations of the BZO surface structure point towards a homogeneous grain structure. The average BZO grain size is 50 nm. The root mean square roughness of 3.2±2 nm indicates quite smooth surface of the buffer system, which is important for a successful epitaxial growth of c-axis aligned YBCO layers or another buffer layer like STO (see section 5.4).

3.3.2 MOD- $SrTiO_3$ buffer layer

The precursor solution for $SrTiO_3$ films was prepared by dissolving 0,515g of the available commercial strontium acetate hydrate (Aldrich), $Sr(CH_3COO)_2 \cdot xH_2O$, in glacial acetic acid (Panreac). To this solution, 0.76 ml of Ti (IV) isopropoxide (Alfa Aesar), $Ti[OCH(CH_3)_2]_4$, was added and the mixture was diluted using methanol anhydrous 99.8% (Panreac). The above mixture was stirred for 30 minutes on a hot plate maintained at 70-80ºC. A final concentration of 0.25M was used throughout this work. TG analysis was done on a dried part of the solution to confirm the temperature range where STO decomposes. It was observed that the decomposition temperature of the STO precursor starts at 150ºC and ends up above 600ºC (Fig. 3-13). The first weight loss occurs in the range of temperatures 50 - 130ºC and it is attributed to

solvent evaporation from the dried gel: water, methanol (boiling point methanol, bp =64.7º) and acetic acid (bp=117-118). The second part we have distinguished on the TGA curve is comprised between 130ºC and 600ºC and it is expected to decompose STO precursor. Based on these results it has been followed a single step heating profile similar to that used for $BaZrO_3$ buffer layer described in Fig. 3-12. We would like to mention that TGA analysis under 95%Ar/5%H_2 atmosphere have been carried out in the range of temperature 25-600ºC due to experimental equipment limitations.

This solution was deposited by spin coating on 5 mm x 5 mm (100) $LaAlO_3$ or (100) $SrTiO_3$ single crystal substrates, supplied by Crystec, and on MOD- (100) $BaZrO_3$ buffer layer fabricated in our group. A spin speed of 5000 rpm for 2 minutes was used for the deposition. The films were then heat treated in Ar/H_2 atmosphere at the previously optimized temperature 700ºC for 4 hours [139]. The corresponding viscosity was 1.56mPa s. These deposition and growth conditions led to buffer layers of thickness ranging 30 to 40 nm.

We anticipate that phase purity and good in-plane and out-of-plane texture were obtained. Optimal results have been obtained on single crystalline substrate, $\Delta\phi$ (202) ≈0.8º and $\Delta\omega$ (200) ≈0.2º with smooth surface (rms ≈ 0 .9nm). It is noteworthy that in this case, lattice mismatch are smaller than for the BZO film, see Table1-I.

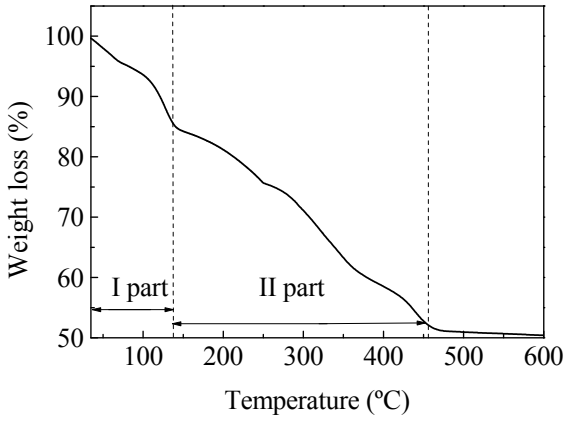

Fig. 3-13 TGA plot performed in Ar/H_2 atmosphere of the STO solution using as precursors strontium acetate, Ti(IV) isopropoxide dissolved in glacial acetic acid and anhydrous methanol. The heating rate was 60ºC h^{-1} between 30 to 250ºC and 198ºC h^{-1} between 250 to 600ºC. The decomposition can be roughly divided in two parts.

3.3.3 MOD-CeO_2 buffer layer

3.3.3.1 Preparation of precursor solution from acetic acid solvent

0,218 g of cerium (III) acetylacetonate hydrate (Alfa Aesar, 99,9%), $Ce(CH_3COCHCOCH_3)_3 \cdot xH_2O$, was dissolved in 2 mL of glacial acetic acid (Panreac), and 10 vol% of water to obtain a stable solution. The mixture was stirred for 30 min at 60ºC. A yellow and transparent solution of 0.25 M was obtained [139]. Ambient humidity was kept below 10 g m^{-3} because Cavallaro [139] found that above this value, films were more favorable to develop cracks than those deposited under a controlled humidity.

Fast aging of precursor solution (several hours) forced us to find improved solvents that were able to supply longer-term stability and simultaneously ease the elimination of organic components of the film. Glacial acetic acid was replaced by propionic acid and propyl alcohol.

These solvents could provide more solubility to $Ce(CH_3COCHCOCH_3)_3$ than acetic acid and methanol because they have an extra carbon in the hydrocarbon chain. In addition, the removal of the carbon-containing contaminants can be carried out via an alternative route avoiding exothermic elimination of CO_2.

3.3.3.2 Preparation of precursor solution from propionic acid solvent

A weighted amount of cerium (III) acetylacetonate hydrate (Alfa Aesar, 99,9%), $Ce(CH_3COCHCOCH_3)_3 \cdot xH_2O$, was dissolved in 1 mL of propionic acid (Aldrich), CH_3CH_2COOH, and 1 mL of anhydrous isopropanol (2-propanol) (Aldrich), $(CH_3)_2CHOH$. The mixture was stirred for 30 min at 60ºC. A yellow and transparent solution was obtained which was deposited on cleaned (10 min acetone and 10 minutes methanol in an ultrasonic bath) (001)-YSZ single-crystal substrates (Crystec) by spin-coating at 6000rpm and an acceleration of 3000 rpm s^{-1} for 2 minutes. The solution's lifetime was several months.

Thermogravimetric analysis (TGA) of CeO_2 gels have been investigated and performed in 95%Ar/5%H_2 (Ar/H_2). Fig. 3-14 (a) presents the TGA curves of two different CeO_2 gels. One represents the thermal decomposition of the dried gel prepared with acetic acid solvent and the second is related to the same precursor but using propionic acid and isopropanol as solvents. The unique difference between the two curves is observed at the beginning of the process (35-100ºC). In this range it appears clearly that the gel of acetic acid looses ~40% of their weight whereas gel of propionic acid/ isopropanol weight loss is smoother (~10% followed by ~30%).

For gel of acetic acid, these looses could not be attributed only to the dehydration of the gel, it should be also attributed to solvent evaporation. These results are consistent considering the nature of the solvents, recall bp of acetic acid is around 117-118ºC.

For gel of propionic acid and isopropanol, the first weight loss is assigned to isopropanol solvent (bp=82ºC) and the second one to propionic acid (bp=180ºC). After this first important loss of weight, the shapes of the two curves follow the same trend, meaning that the decomposition occurs at the same time. Contrasting with decomposition of STO gel presented above, it is noticeable that CeO_2 precursor is still not completely decomposed at 600ºC.

Finally, it has been adopted the same heating profile for both gels and it is described in Fig. 3-14 (b). As-deposited films were heated to 900ºC at 1500ºC h^{-1} for 8 hours in reducing- Ar/H_2 conditions compatible with the available technical substrates. Obtention of highly epitaxial CeO_2 film under these reducing conditions is not straightforward. Optimization process and film characterization is described in detail in chapter 7. We anticipate that substitution of glacial acetic acid precursor for propionic acid and isopropanol solved the main drawback of the initial precursor solution (aging) and improve crystallinity of CeO_2 films.

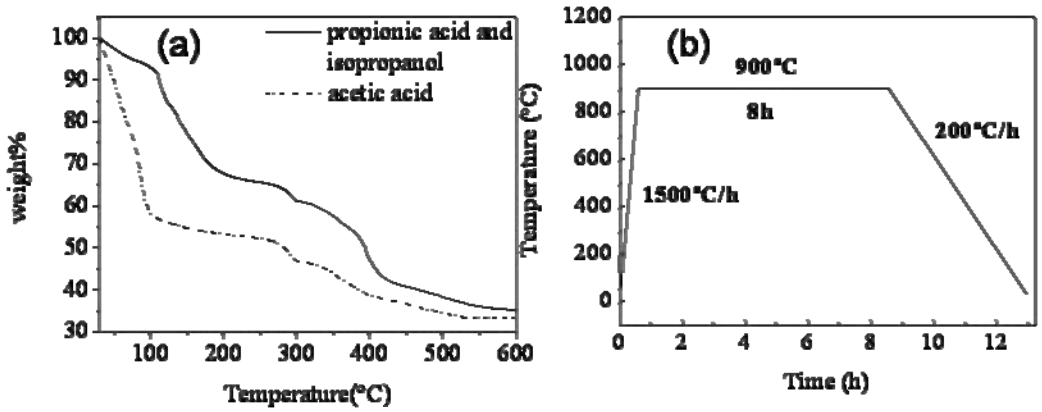

Fig. 3-14 (a) TGA plot of a dried gel from the CeO_2 precursor solutions. The heating rate was 300ºC h^{-1} between 35ºC and 300ºC and 1500ºCh^{-1} between 300ºC and 600ºC. (b) Typical thermal treatment followed for MOD-CeO_2 growth.

3.3.3.3 Preparation of precursor solution of doped-CeO_2

Cerium pentadionate ($Ce(CH_3COCHCOCH_3)_3$, 99.9% from Alfa) and gadolinium pentadionate ($Gd(CH_3COCHCOCH_3)_3$, 99.9% from Aldrich) or zirconium pentadionate $Zr(CH_3COCHCOCH_3)_4$ 99.9% Aldrich) were chosen as starting materials.

For 10% of dopant: Dopant precursor (Zr^{4+} (0.025g)or Gd^{3+} (0.023g)) was dissolved in 1 mL of propionic acid and 1 mL of isopropanol, the solution was stirred and heated (40ºC) for 20

minutes, followed by the addition of the stoichiometric amount of $Ce(CH_3COCHCOCH_3)_3$ and stirred for another 20 minutes at 60ºC. The total metal concentration of the solution was controlled to be 0.25 M. The precursor solution with a viscosity of 3 mPa s was spin-coated at 5000 rpm for 1.5 minutes on the (100)YSZ single crystal substrate and grown with the deposition conditions and heating profile reported above for undoped CeO_2 Fig. 3-14 (b). The final thickness of the film was about ~30 nm.

From TG analysis we do not observe important differences in decomposition process between doped and undoped CeO_2 precursor. In doped-ceria, the weight of the final decomposition product differs from undoped ceria because of the contribution of heavier cations: Zr^{4+} or Gd^{3+} . Incorporation of aliovalent cation does not modify the stabilization of precursor gel nor the decomposition mechanism. Further characterization of crystallinity, surface morphology and chemical composition are described in detail in Chapter 7.

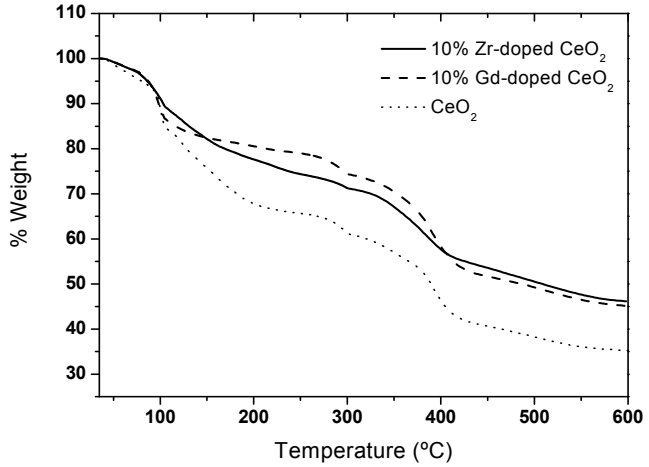

Fig. 3-15 TGA plot of a dried gel from the CeO_2 and doped-CeO_2 precursor solution fabricated from propionic acid and isopropanol. The heating rate was 300ºC h^{-1} between 35ºC and 300ºC and 1500ºCh^{-1} between 300ºC and 600ºC performed under 95%Ar/5%H_2 atmosphere.

A. Perovskite structure

CHAPTER 4

Stress-induced spontaneous dewetting of heteroepitaxial $YBa_2Cu_3O_7$ thin films

4.1 Motivation

For the preparation of YBCO coated conductors, epitaxial growth should be transferred from the substrate to the YBCO film through compatible buffer layers (section 1.2). Although the film and the substrate have similar structure, the film can undergo a temperature-induced morphological instability due to the interfacial strain associated to the lattice parameter misfit, yielding to spontaneous formation of discontinuous films [140,141].

While extensive research has been made concerning the formation of semiconductor nanostructures such as nanodots or nanowires through interface strain control [142,143], the study of epitaxial oxide nanostructures has been very scarcely explored [144,145]. Particularly, the stability of heteroepitaxial YBCO films is unknown and no reports have been made concerning the generation of spontaneously ordered structures controlled by the interfacial strain.

In this chapter we give for the first time evidence of the spontaneous generation of strain-induced surface structures in YBCO films epitaxially grown on different types of single crystal ($LaAlO_3$, $SrTiO_3$) or oxide buffer layer with modified lattice mismatch values ($BaZrO_3$). These substrate materials and buffer layer have been selected as model systems to understand the formation mechanisms of YBCO films and islands. It appears as a unique opportunity for both controlling the interfacial YBCO thin film quality and determining under which conditions the heteroepitaxial films are stable to obtain high quality and continuous YBCO films in coated conductors.

We propose an analysis of the surface free energy for the YBCO films allowing defining a scenario where the spontaneous formation of surface structures is understood as a consequence of a dewetting effect, allowing to relieve the elastic energy [146]. We show that the film instability depends on the film thickness and the degree of interfacial strain. Actually, modeling the surface free energies in heteroepitaxial films is a first step towards a complete mastering of the formation of self-assembled interfacial nanostructures, such as nanodots, where the required repulsive interactions are mediated via strain field [147]

4.2 Influence of growth temperature on TFA-YBCO film stability on (100)$LaAlO_3$

4.2.1 Structural characterization

We started by studying the influence of growth temperature on TFA-YBCO film stability grown on (100)-$LaAlO_3$ single crystal substrate ($\varepsilon = (a^{LAO}-a^{YBCO})/a^{YBCO} = -1.8\%$, see 1.2.1.1).

The synthesis of the trifluoroacetate (TFA) precursor solution for YBCO layers used in the present chapter was carried out as described previously (3.1.1.1), using TFA- precursor salts with a metal concentration of 0.8M. From this total metal concentration results a final film thickness of ~ 150 nm.

TFA-YBCO films were grown in a range of temperatures 750-860ºC under $P(O_2)$ =0.1kPa and gas flow (V_g) = 2.3 $x10^{-3}$ ms^{-1} for 180 minutes. The heating profile used in these experiments was based on a standard high temperature heat treatment shown in Fig. 3.5. Post-annealing treatments were carried out in some cases to investigate the kinetics of the dewetting phenomena.

X-ray diffraction θ-2θ scans were performed to investigate phase purity and crystalline quality for two representative TFA-YBCO films grown at 795ºC and 860ºC, shown in Fig. 4-1. It is observed that the films are mainly (00*l*) oriented, indicating c-axis preferred orientation of the YBCO, but secondary phases have also been detected. They are indexed to BaF_2, Ba_{1-}

$_xY_xF_{2+x}$ (BYF) and Y_2O_3. By considering the pathway reaction for YBCO formation, see Fig. 1-12 , it is clear that they are precursors that have not been completely transformed to c-axis YBCO [71]. However, by the high intensity of (00*l*) YBCO reflections we consider that the film is almost converted and such secondary phases will not be detrimental for superconducting properties. Based on recent work performed in our laboratory we can now explain the presence of precursor specimens in our film as due to the low gas flow rate (2.3 $x10^{-3}$ ms^{-1}) which limited the YBCO growth conversion [99,89].

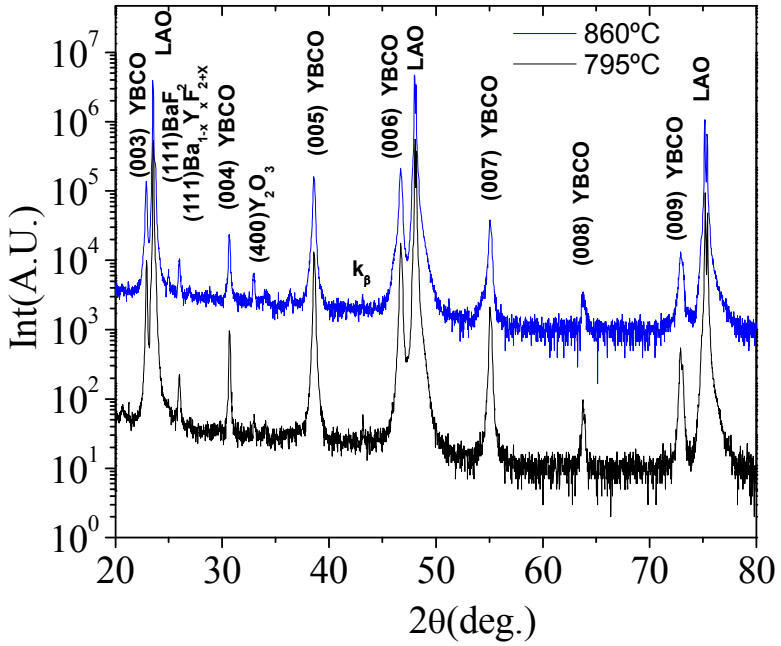

Fig. 4-1 XRD patterns of YBCO on LAO grown during 180 min in a humidified gas mixture containing 0.1 kPa oxygen at 795ºC and 860ºC.

Furthermore, according to XRD θ-2θ scans, the intensity of (005)YBCO Bragg line reflection increases with increasing annealing temperature until it saturates at 860ºC. Since Bragg line intensity of precursor phases are weak, the increase in I(005) has not been attributed to the formation of YBCO phase, indeed, it has been suggested that reflects an improvement of YBCO texture. Fig. 4-2 (a) shows the dependence of the I(005) on the growth temperature. To characterize the quality of out-of-plane orientation of YBCO (001) planes, X-ray ω-scans were performed for the YBCO (005) reflections. The out-of-plane quality can be evaluated from the full-width-at-half-maximum (FWHM) of the ω-scans. From it we find a decrease of FWHM with increasing growth temperature. Finally, in the range of 795-860ºC the FWHM is 0.7 ±0.1 º, showing a high degree of alignment in the out-of-plane direction of YBCO, Fig. 4-2(b). Similar

trend has been found in the study of in-plane alignment through (102) Bragg line reflection. Typical FWHM values of the ϕ-scan were $\Delta\phi \approx 1.3^{\circ}$.

We conclude then, from x-ray diffraction studies that crystallinity of YBCO films improve with growth temperature until it saturates [91].

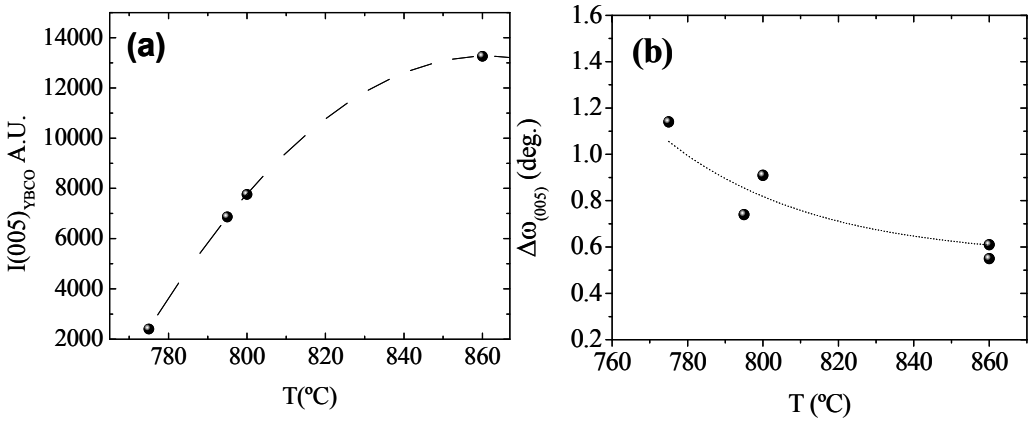

Fig. 4-2 (a) Dependence of the YBCO (005) peak intensity on the growth temperature. (b) Dependence of FWHM values of the ω-scans (005) YBCO on the growth temperature.

4.2.2 Morphological characterization

Even though X-ray diffraction analysis points 860ºC as optimal growth temperature, surface morphology and superconducting properties have to be investigated.

We turn now to the study the surface morphology for both films by SEM. As it can be seen in Fig. 4-3 (a) the film grown at 795ºC has a homogeneous and flat surface with very few pores or pinholes and that grown at 860ºC, Fig. 4-3 (b), displays a very pronounced dewetting effect with many holes propagating in a branched manner and keeping a parallepipedic-like geometry with the lateral faces being mainly parallel to the $\{100\}_{LAO}$ planes. A detail of the strong tendency toward a parallepipedic structure of the generated pinholes can be appreciated in the inset included in Fig. 4-3(b). Similar film dewetted images were obtained in films prepared at temperatures intermediate between 795ºC and 860ºC, but with a progressive decrease of the relative surface area displaying the dewetting phenomenon and with a reduction of the size of the holes that seem to nucleate randomly as small patches in the original flat films. Note that film displaying optimal texture and crystallinity obtained at 860ºC corresponds to dewetted morphology. We would like to remark that for YBCO coated conductor fabrication the most feasible growth temperature might be 795ºC, as will confirm superconducting properties discussed below [91].

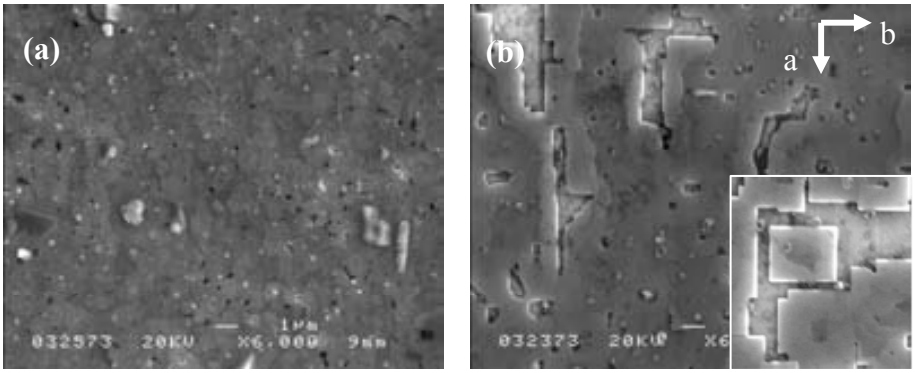

Fig. 4-3 Surface morphologies of the YBCO/LAO films grown under the different temperature conditions observed by SEM (a) 795ºC and (b) 860ºC

In order to investigate if such morphological instabilities occurred during the heat treatment process or otherwise resulted from a rapid cooling rate which could not facilitate the accommodation of different thermal expansion coefficient of YBCO (α=11.5 x10^{-6}ºC^{-1}) and LAO (α=10-13 x10^{-6}ºC^{-1})[148], we prepared YBCO films in similar conditions to that described above but modifying the cooling rate from 1500ºC h^{-1} down to 60ºC h^{-1}. As it can be seen in Fig. 4-4, a similar microstructural instability was obtained. Thus, from these experimental results we confirm that the breakup phenomenon is not dependent on the cooling rate parameter.

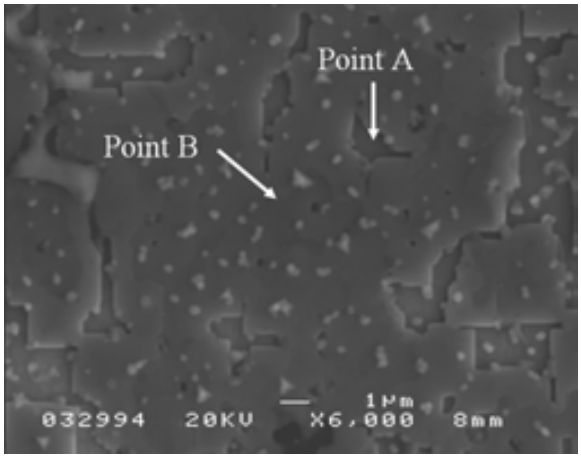

Fig. 4-4 TFA-YBCO film grown on LAO single crystal at 860ºC for 180 min with a cooling rate of 60ºC h^{-1}.

In order to investigate chemical composition of the parallepipedic -shaped holes, EDX analysis was employed. We analyzed two different points in the same film: one region in which we focused on a hole, point A from Fig. 4-4, and another one in which we have a continuous layer, point B from Fig. 4-4. Their corresponding EDX spectrums are shown in Fig. 4-5 (a) and

Fig. 4-5 (b) respectively. The EDX analysis on the hole region demonstrates the presence of Al and La, components of the single crystal substrate: $LaAlO_3$. Oxygen presents a characteristic peak at 0.52 keV. Unfortunately, this peak is very weak and is overlapped with a more intense peak of La, therefore, it cannot be detected in the EDX analysis. Nevertheless, it is reasonable to consider that the parallepipedic-shaped holes expose $LaAlO_3$ single crystal substrate. In contrast, from the EDX analysis of the covered area we detected La, Al, Cu, Y and Ba. Due to the matching of the Ba and La, it is difficult to quantify this spectrum but qualitatively we can estimate that in this region we have a contribution of both $LaAlO_3$ and $YBa_2Cu_3O_7$.

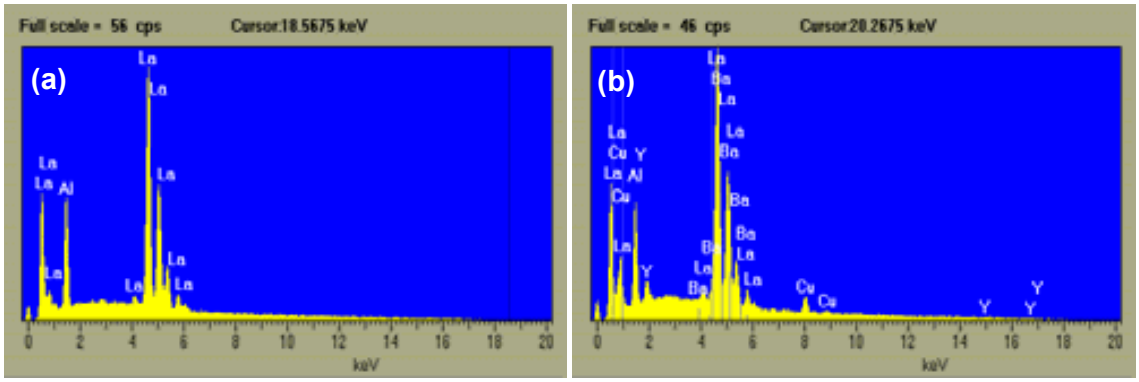

Fig. 4-5 EDX spectra of the (a) parallepipedic -shaped holes in the YBCO film and (b) substrate covered with YBCO layer.

Thus, EDX analysis indicated that the observed holes are free of Y and Cu, and hence we can conclude that a full migration of the YBCO film occurs from these regions. These results are supported by TEM microstructure analysis presented further on in this chapter. An AFM height profile analysis of these dewetted regions has also been carried out (see a typical example in Fig. 4-6 (a)), which indicates that, typically, these hole regions are about 100 nm-150 nm deep, coinciding with the entire thickness of the YBCO film. In agreement with EDX analysis, it indicates the full film has been eliminated in these regions.

From the AFM height profile analysis we also observed that the average rms roughness of the covered areas is very low, i.e. ≈ 2 nm or about two unit cells. This indicates that the films have a high atomic mobility which allows a strong mass redistribution. It is noticeable as well that very often some mass accumulation is detected near the edges of these holes (see Fig. 4-6 (a) and (b)) with YBCO overgrowths as high as ≈ 50 nm. This indicates that mass diffusion away from the holes has not been still completely redistributed in the time scale of our growth experiments, i.e., 180 min, or that this is a continuous process and so a film thickness gradient exists. We should note, however, that when the film thickness is increased to 300 nm, the dewetting effect was not detected anymore under our growth conditions. In Fig. 4-7 it is shown

a YBCO film with a thickness of 300 nm which displays a continuous surface morphology with some pores.

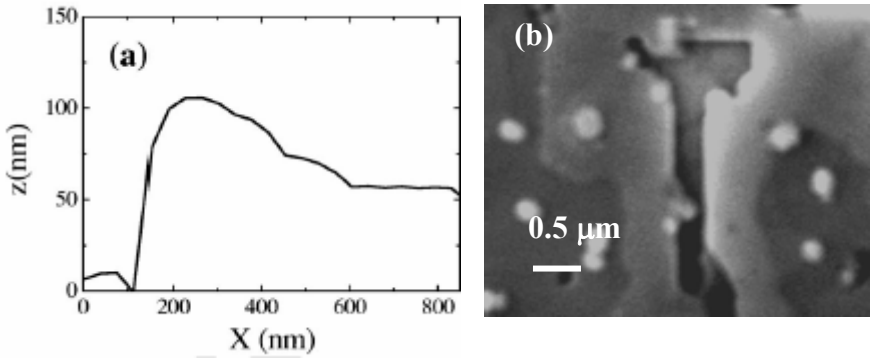

Fig. 4-6(a) AFM height profile of the YBCO film thickness when a dewetted region is crossed; (b) SEM micrograph showing a detail of a YBCO film near a dewetted area where the mass accumulation near the edges of the YBCO film can be appreciated.

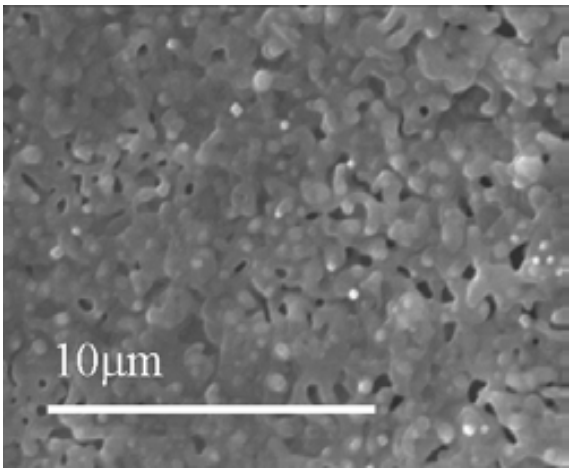

Fig. 4-7 300 nm thick TFA-YBCO film grown on (100)-$LaAlO_3$ single crystal substrate at 830ºC for 180 min at P_{O2} =0.1kPa and $P(H_2O)$=0.6kPa.

These results then suggest that dewetting is induced by interfacial strain, i.e., the relative lattice mismatch between YBCO and LAO layers, but this only occurs below a certain film thickness. Also, the shape of the holes created in the YBCO surface clearly indicates that there is a tendency to create mainly {100} facets of the high-temperature tetragonal YBCO phase. This indicates that this is the more stable crystal face, besides the already existing (001) face.

4.2.3 Study of microstructure of dewetted areas

To understand the microscopic mechanisms leading to the spontaneous formation of dewetting in heteroepitaxial YBCO films it seems very appealing to further investigate the microstructure by means of TEM. Fig. 4-8 (a) and (b) display TEM cross sections of typical regions where dewetting occurs in a YBCO/LAO film grown at 860ºC. The low resolution image of Fig. 4-8 (a) confirms that sharp new {100} faces are indeed formed for the whole YBCO film thickness of ~ 150 nm and also that the films are single phase without any entrapped liquid and completely pore-free, similarly to the films annealed at lower temperatures [149]. High resolution images of the interfacial regions with the substrate (Fig. 4-8 (b) and (c)) show, first, that the LAO surface is indeed free of YBCO in the dewetted areas, thus indicating that YBCO has completely migrated to reduce the interfacial surface energy. On the other hand, we observe that the YBCO/LAO interfaces remain of high quality, without any sign of interfacial secondary phases. This confirms that there is no mutual reactivity or a decomposition of the YBCO phase that would modify the interfacial energy of the heteroepitaxial structure. These results are consistent with X-ray diffraction θ-2θ scan where no interface reaction product has been identified.

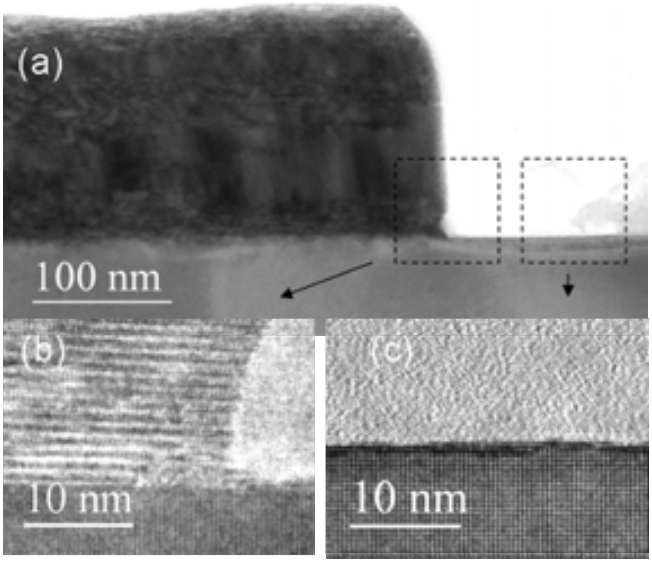

Fig. 4-8 (a) Cross section TEM image of YBCO films grown at 860ºC showing a typical dewetted region, (b) HRTEM image of the YBCO film near the interface with the LAO substrate indicating a sharp termination parallel to {100} planes; (c) HRTEM image of the LAO surface at the dewetted regions showing complete migration of the YBCO film.

It is also very useful to analyze the defect structure of the YBCO film and its interface with the LAO film. Fig. 4-9 (a)- (b) show high resolution TEM images of a YBCO film grown at 860ºC, where we can identify first that interfacial misfit dislocations have been formed to accommodate the lattice mismatch in the heterostructure [150,151]. These misfit dislocations can be observed all along the YBCO/LAO interface, though with some degree of disordered periodicity, which would indicate that some residual stress persists. In some cases (Fig. 4-9 (b)), however, a regular distribution of the interfacial dislocations is actually observed, which allows us to conclude that the elastic energy associated with the interfacial strain is already fully relaxed after the growth of few YBCO cells, and so a semicoherent film results (see 1.2.1.1). The relief of the interfacial elastic energy in these YBCO heterostructures proceeds then, both through the formation of dewetted areas and through plastic deformation, though some complex interaction may exist among both mechanisms [140,152]. It is also particularly striking to note that the YBCO films can display, in some cases, a structure completely free of planar defects, such as the stacking faults that are very often observed in YBCO films grown by the TFA methodology [153,154,34,155] (see Fig. 4-9 (a)). In some cases however (see Fig. 4-9 (c)), a sharp transition from an initial strongly defective structure toward a defect-free region is observed when the film thickness is increased.

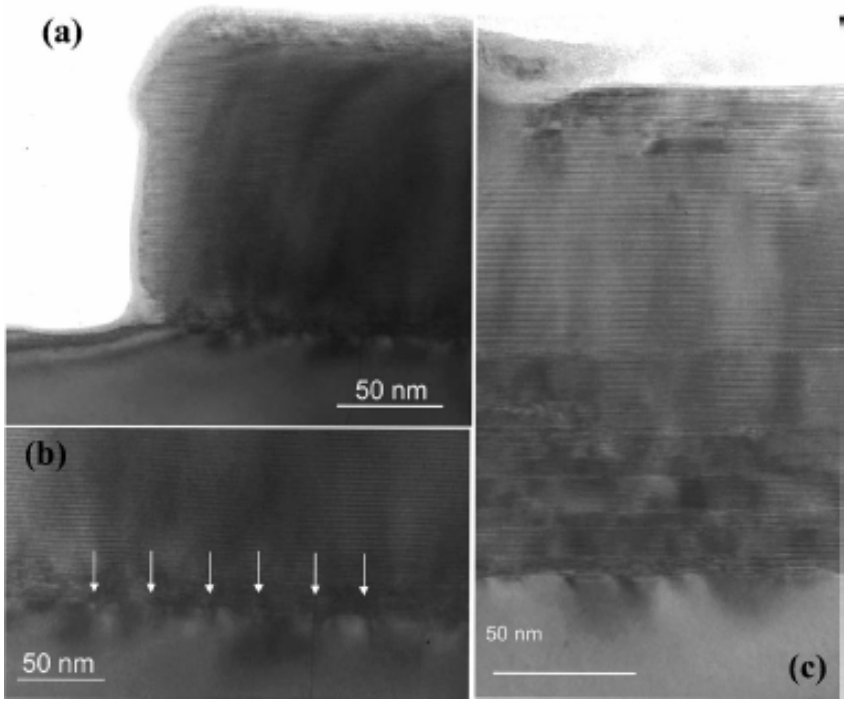

Fig. 4-9 Cross section TEM images of a YBCO film grown at 860ºC on a LAO single crystalline substrate. (a) Image of a region adjacent to a hole where a defect-free area across the whole film is discerned and where the interfacial area shows that misfit dislocations have been formed; (b) details of an interface where regular misfit dislocations are indicated by arrows;(c) details of a full cross section where a sharp transition from a defective (planar defects) region originated at the interface toward a nondefective region in the upper side of the film is clearly discerned

The origin of the formation of these complex microstructures in these heteroepitaxial YBCO films grown at high temperatures is still uncertain, but it is certainly related to the existence of different pathways, to relief the interfacial stress between YBCO and the substrate due to the lattice mismatch.

4.2.4 Superconducting properties

As a final experimental investigation intending to quantify the relevance of the film dewetting phenomenon, we have studied the influence of the growth temperature on the superconducting and normal state properties of the YBCO films grown on LAO substrates when fixed growth times (≈180 min) are used. Fig. 4-10 (a) displays a typical temperature dependence of the normal state resistivity ρ(T) of two YBCO films displaying a different degree of surface dewetted area. Fig. 4-10(b) summarizes the influence of the growth temperature on the normal state resistivity of the films measured at 300 K, ρ_{300K}, and the critical current density measured at 5K, J_c(5K). We should remind at this stage that our microstructural observations displayed a progressive enhancement of the dewetted areas above T≈ 800ºC, while at lower growth temperatures the film can also keep some residual porosity, probably due to a reduced grain growth after YBCO island nucleation [99], which it has been previously shown to have also some influence on the transport properties [156,99]. Both ρ_{300K} and J_c(5K) are very sensible magnitudes to reflect the evolution of the film microstructure and actually, as it can be seen in Fig. 4-10 (b), they agree to signal that the optimum film microstructure is obtained at T≈800ºC. At lower growth temperatures the residual porosity degrades somehow the metallic and superconducting properties of the films [153,99]. The enhanced resistivity computed at high temperatures is actually a consequence of the reduction of the effective YBCO film cross section due to an inhomogeneous distribution of the migrated YBCO mass during the dewetting process. Correspondingly, the computed critical current density J_c and normal state resistivity assume smaller and larger mean values, respectively, when film dewetting occurs.

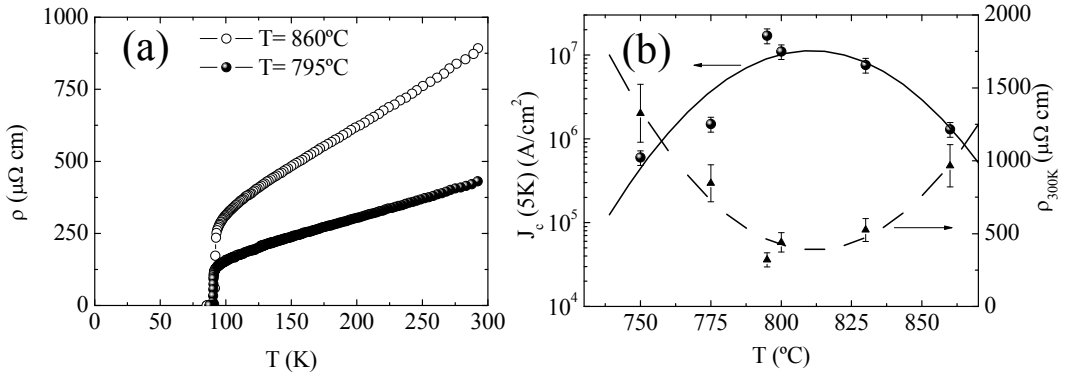

Fig. 4-10 Superconducting and electrical resistivity measurements performed on YBCO/LAO system (a) Temperature dependence of the normal state resistivity ρ(T) of two films having different degrees of dewetted areas (T= 795ºC and T=860ºC). (b) Dependence of the room temperature resistivity ρ_{300K} and the critical current density at 5K, J_c(5K), with the growth temperature.

4.3 Free energy and film instability model

From the above results and based on work from Seifert [141], here we propose a free energy model, which includes surface energy anisotropy and the spacing between preexising holes to describe this instability phenomenon.

Our analysis considers a single crystal film of initial thickness $\boldsymbol{h_0}$. The geometrical parameter used to describe the hole size is $\boldsymbol{x}$, which as we have mentioned above will vary with growth temperature and $\boldsymbol{a}$ is the typical spacing between cavities, as shown in Fig. 4-11.

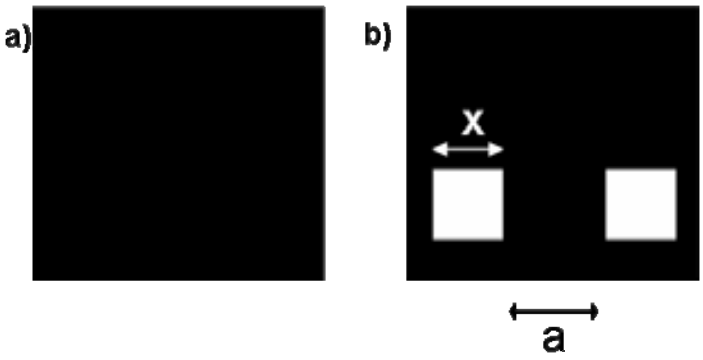

Fig. 4-11 Schematic of the configurational change of the unit cell chosen for the free energy calculation. (a) continuous layer , (b) film which has broken up and two cavities have been formed where $\boldsymbol{x}$ is the hole size and $\boldsymbol{a}$ the separation distance between two cavities.

Accordingly, the area of the continuous film have been normalized and it is given by,

$$A = a^2(1-x^2) \qquad \text{Eq. 4-1}$$

Because the film volume is conserved during the hole growth, the film thickness ***h*** concurrently increases with increasing hole size ***x***. To simplify calculations, we define ***h*** as a function of h_0 as follows,

$$h = \frac{h_0}{(1-x^2)} \qquad \text{Eq. 4-2}$$

Once defined and normalized our system we have to define the energy components. The driving force for the evolution of the film structure is always the difference in the free energy between the equilibrium state and the metastable state. The general free energy expression, E, of the film/substrate system is given by,

$$E = A_t\gamma_t + A_p\gamma_p + A_i\gamma_i + A_S\gamma_S \qquad \text{Eq. 4-3}$$

where γ is the surface energy per unit area, A the area and the subscripts denote the surface of the film (t), the new surface formed (p), the interface film/substrate (i) and the uncovered substrate surface(s).

The observation of parallepipedic holes and YBCO islands indicates that the most stable surfaces are the upper face of the (00l) textured YBCO film and the lateral faces {100} of the parallepipedic dewetted areas (i.e. $\gamma_t=\gamma_{001}$ and $\gamma_p=\gamma_{100}$). Therefore we can assume that the only relevant interfacial energies are: γ_{001}, γ_{100}, γ_i and γ_s where γ_i and γ_s correspond to the interfacial energy of the YBCO film with the substrate and the free surface of the substrate, respectively.

To understand the formation of the new observed structures we need to compare the film energy when it wets completely the substrate, E_o, with that corresponding to a partially dewetted structure, E.

Therefore we can write the total surface energy E_o of a homogeneous film with a surface $A=a^2(1-x^2)$ and when it has some dewetted regions E, as follows:

$$E_o = \left(a^2\left(1-x^2\right)\right)(\gamma_{001} + \gamma_i) \qquad \text{Eq. 4-4}$$

$$E = A_{001}\gamma_{001} + A_{100}\gamma_{100} + A_i\gamma_i + A_s\gamma_s \qquad \text{Eq. 4-5}$$

where the symbols A_j stand for the corresponding areas of these surfaces. In order to compute the relative stability of the different surface configurations we need to compare the corresponding energies E and E_o, therefore we have calculated the ratio $\bar{E} = E / E_0$ as a function of the normalized dimension x of the dewetted areas in the film having an initial thickness h_o (Fig. 4-11), Eq. 4-5 can thus be rewritten as:

$$E = a^2(1-x^2)(\gamma_{001} + \gamma_i) + ax\frac{h_0}{(1-x^2)}\gamma_{100} + a^2x^2\gamma_s \quad \text{Eq. 4-6}$$

In order to compute the relative stability of the different surface configurations we would need a complete knowledge of the different surface energies involved in Eq. 4-6 but these energies are not known at present, therefore we have normalized these energies to γ_{001} and we have examined the general behaviour of the film under reasonable range values in order to analyze the relative stability of the different surface configurations. The corresponding equation is the following:

$$\bar{E} = \frac{E}{E_0} = (1-x^2) + \frac{xh_0}{a(1-x^2)}\left[\frac{\left(\frac{\gamma_{100}}{\gamma_{001}}\right)}{1+\left(\frac{\gamma_i}{\gamma_{001}}\right)}\right] + x^2\left[\frac{\left(\frac{\gamma_s}{\gamma_{001}}\right)}{1+\left(\frac{\gamma_i}{\gamma_{001}}\right)}\right] \quad \text{Eq. 4-7}$$

As we can see, only three interfacial energy ratios are relevant for the present problem. Also we can very safely make the following approximation $\gamma_s/\gamma_{001} \approx 1$, i.e. we assume that the free (00l) surfaces of the substrate and YBCO have similar stabilities which are very reasonable for these stable surfaces. On the other hand, the relative stability of (100) and (00l) faces in YBCO crystals has been estimated for YBCO crystals from the crystal shape grown from solution which leads to a ratio $\gamma_{100}/\gamma_{001} \approx 5$ [157] (see Fig. 4-12). Therefore we can easily estimate the relative stability of the different surface configurations through a modification of the ratio γ_i/γ_{00l} which will correspond actually to the situation of the different investigated substrates or buffer layers having different interfacial energies due to the modified strains when the lattice mismatch with YBCO is changed.

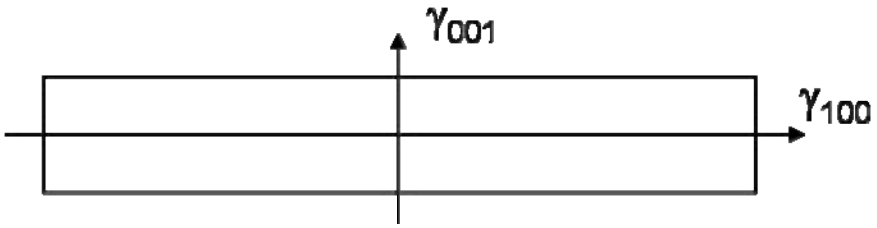

Fig. 4-12 Two-dimensional construction of Wulff, showing the geometric relationship between (001) and (100) on the growth morphology of YBCO. The aspect ratio (crystal width: thickness) is generally superior to 5.

Fig. 4-13 (a) displays, as a typical case, the dependence of the ratio E/E_o with x for different initial film thickness h_o, ranging from 0.1 to 0.001, and a single interfacial energy γ_i/γ_{001}=0.4. It is assumed γ_i/γ_t = 0.1 if both specimens have the same structure and similar lattice parameter, Fig. 4-13 (b) displays, also as a typical case, the corresponding results for different interfacial energies for a single film thickness h_o/a=0.025. As it can be seen in Fig. 4-13(a), the YBCO film becomes unstable, i.e. E/E_o<1, below a certain film thickness, in agreement with our experimental observations. Also the fraction of dewetted area is clearly increased when the film thickness is reduced thus becoming very easy to generate submicrometric YBCO islands, similarly to other oxides displaying ferroelectricity, ferrimagnetism, etc. [144,145]. On the other hand, Fig. 4-13 (b) shows that the heteroepitaxial YBCO films become less stable when the interfacial energy increases. Therefore, if the interfacial energy is enhanced by a higher lattice mismatch, as it was the case for our experimental study of the YBCO/BZO/LAO heterostructure, the fraction of dewetted area will increase as it was indeed experimentally observed and presented below. It's clear then that it becomes possible to engineer YBCO nanostructures through tailoring the lattice mismatch in bilayer heterostructures.

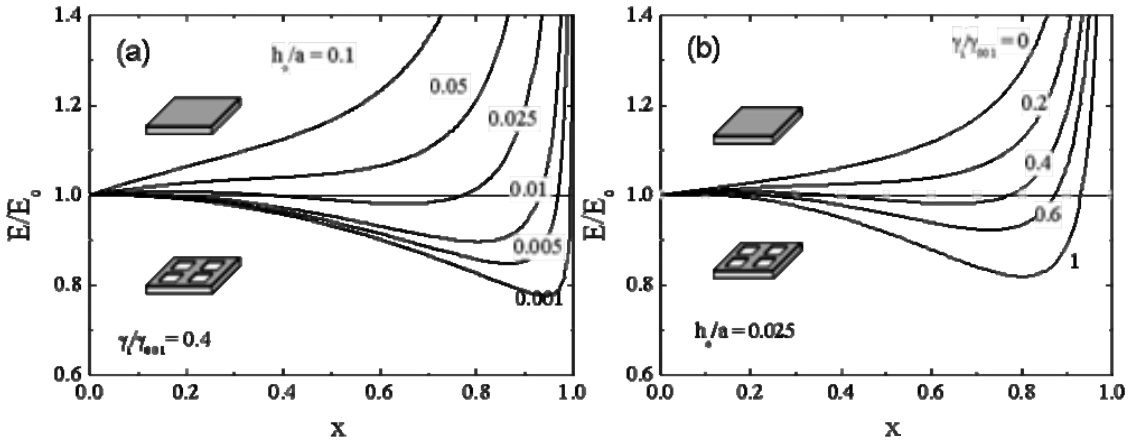

Fig. 4-13 (a) Free energy dependence on the cavity size varying initial film thickness h_o/a . The following variables are held fixed for this diagram: γ_i/γ_{001} =0.4, $\gamma_{100}/\gamma_{001}$=5 and γ_s/γ_{001} =1. (b) Free energy dependence on the cavity size varying γ_i/γ_{001} ratio. It has been kept constant: $\gamma_{100}/\gamma_{001}$=5 and γ_s/γ_{001} =1 and h_o/a =0.025

Finally, to summarize the results of our free-energy analysis, we represent in Fig. 4-14 the stability regions of continuous YBCO films when the thickness and the interfacial energies are linked. As it can be seen, even for relatively low interfacial energies there is a certain range of film thickness where the heteroepitaxy becomes unstable. Within these regions of film thickness-interfacial energy there is a strong potential for the spontaneous generation of ordered YBCO nanostructures through control of interfacial strain as it has been largely demonstrated for semiconductors.

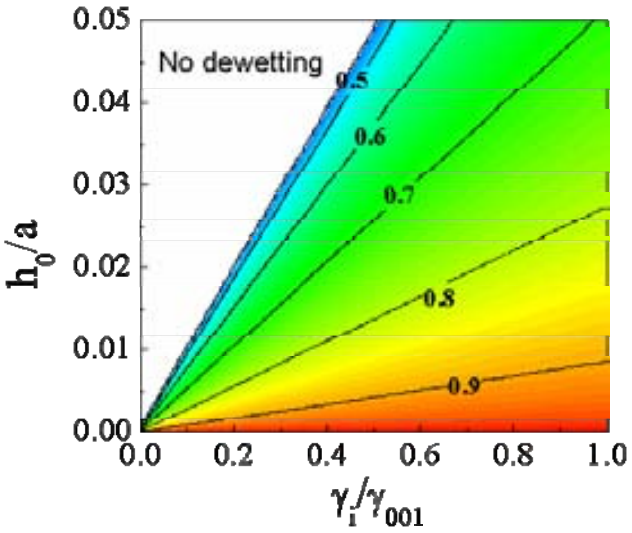

Fig. 4-14 Stability diagram mapped for varying initial film thickness h_o/a and ratio of the film/substrate interfacial energy to the top surface energy γ_i/γ_{001}. The colored/white areas mark the regions where dewetting/no dewetting occurs. Within the colored region there is an evolution of the surface fraction of dewetted area x. Colors and straight lines indicate x_{min}, i.e., the x value corresponding to the equilibrium configuration (minimum energy E/E_0)

4.4 Influence of long processing time on the YBCO films stability

We should now wonder ourselves if the spontaneously generated surface structures described above are in a quasiequilibrium state or, instead, if they are kinetically limited structures. This is a key issue because, first, it will put the basis for modeling the observed behavior and, second, it will open the possibility to generate different nanostructures controlled through growth kinetics and coarsening effects [158,159]. For those reasons we have

investigated the influence of the annealing time on the surface structure of the YBCO films. For instance, a YBCO film was grown at a temperature where a homogenous film is obtained after a growth time of ≈180 min, i.e., at ≈795ºC, and then an additional long annealing time (12h) is applied at a slightly higher temperature, for instance, at 820ºC. The results are extremely spectacular, as it can be seen by comparing the two SEM images included in Fig. 4-15. While the film grown at short times only displays very few nanometric pinholes (Fig. 4-15(a)), the additional thermal annealing treatment (Fig. 4-15 (b)) induces severe dewetting, and isolated micrometric and nanometric YBCO islands, spheridized to minimize their surface energy. We can then conclude that the heteroepitaxial structure of the YBCO films with a thickness 0.15 μm is a metastable state that evolves toward a new equilibrium state through a slow atomic diffusion process.

Under the typical growth conditions of YBCO films, the observed structure is then metastable and limited by diffusion kinetics. It is very likely, however, that a nucleation energy barrier exists for the formation of pinholes from which the dewetted areas are propagated. In our TFA-YBCO films grown at 820ºC actually some square shaped pits are already observed (Fig. 4-15(a)), which probably corresponds, to these nucleation centers. It is very likely that the island growth mode typically observed in MOD films facilitates the formation of these patches and hence the spontaneous formation of dewetted films, however, a complete analysis of the patch nucleation and growth dynamics of the dewetted areas would be required to achieve a full image of the complex pattern generation.

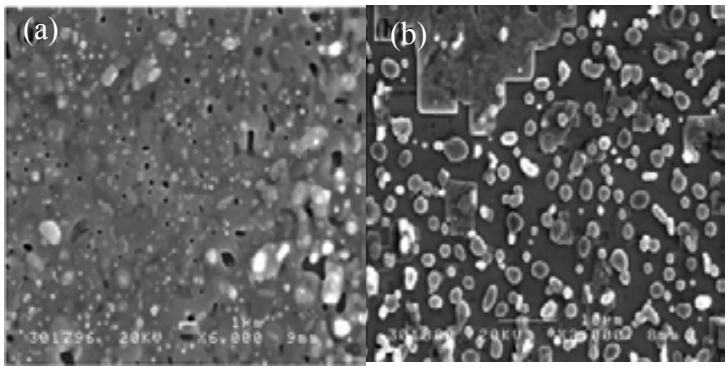

Fig. 4-15 SEM micrographs of YBCO films grown by TFA-MOD on a LAO single crystal substrate with different durations (a) Film grown at 820ºC during 180 min; (b) film grown at 790ºC during 180 min and post-annealed at 820ºC during 12h.

4.5 Influence of the substrate on the dewetting phenomena

To further verify our free energy model and if the morphological instability is indeed induced by the interfacial strain associated to the lattice parameter, we carried out the heteroepitaxial growth of YBCO on STO single crystal substrates and on MOD-BZO buffered LAO single crystal substrates.

It is of interest to study the stability of YBCO on those systems since STO is suitable buffer layer for YBCO coated conductors due to similar lattice constants and coefficients of thermal expansion [160,49]. On the other hand, BZO is a suitable candidate for SOE-NiO template to prevent the poisoning of the superconducting layer with Ni. Furthermore, it reduces the lattice misfit between NiO and YBCO, ε^{NiO}= -8.3% [24].

The lattice mismatch between YBCO and LAO is ε^{LAO}= -1.8%, while that with STO and BZO are ε^{STO}= +1.1% and ε^{BZO}= +8.1%, respectively. In accordance with the free energy model proposed above we should expect then an enhanced interfacial energy in the two latter cases, though some chemical bond contribution to the interfacial energy cannot be disregarded.

Specimens described in this section were heat treated 180 min in the range of temperatures between 775ºC and 860ºC, in the same conditions as the previous system YBCO/LAO. The furnace atmosphere was ultrahigh purity oxygen/nitrogen gas mixture containing 0.1kPa oxygen, $P(H_2O)$=0.6kPa and with V_g=2.3 x10^{-3} ms^{-1}.

4.5.1 Structural characterization

4.5.1.1 YBCO/STO system

XRD θ-2θ scans were carried out for two representative TFA-YBCO films, T= 795ºC and 860ºC, shown in Fig. 4-16. Besides the (00*l*) STO and (00*l*) YBCO Bragg line reflections peaks assigned to intermediate and/or secondary phases such as BaF_2, BYF, $Y_2Cu_2O_5$, CuO, Y_2O_3 were detected in both patterns [71].

Considering growth parameters, the presence of intermediate phases are consistent with low growth rate [99], moreover, it is in well agreement with experimental results obtained in the previous YBCO/LAO system. Additionally, at 860ºC we have detected secondary phases tentatively identified as $BaTiO_3$ and Ba-Sr-Ti-O which are likely to form due to interface reaction between YBCO and STO [20,91]. Furthermore, the formation of these interface reaction products yield to excess of Y and Cu which must be accounted for in some form. The

presence of high intensity peaks at XRD θ-2θ scan for Y_2O_3, $Y_2Cu_2O_5$, CuO phases at 860ºC would satisfy this mass balance [161].

It has been also acquired ω- and ϕ-scan to investigate YBCO in-plane and out-of-plane orientation. Optimal FWHM values has been obtained for the growth temperature of 810ºC giving a $\Delta\omega$=0.5º and $\Delta\phi$= 2.1º, shown in Fig. 4-17. In addition, contrasting with YBCO/LAO system, degree of crystallinity does not saturate with increasing temperature. At 860ºC, crystallinity and grain alignment has been strongly deteriorated due to interface reaction. This is the first indication of the substrate influence on the TFA-YBCO film growth.

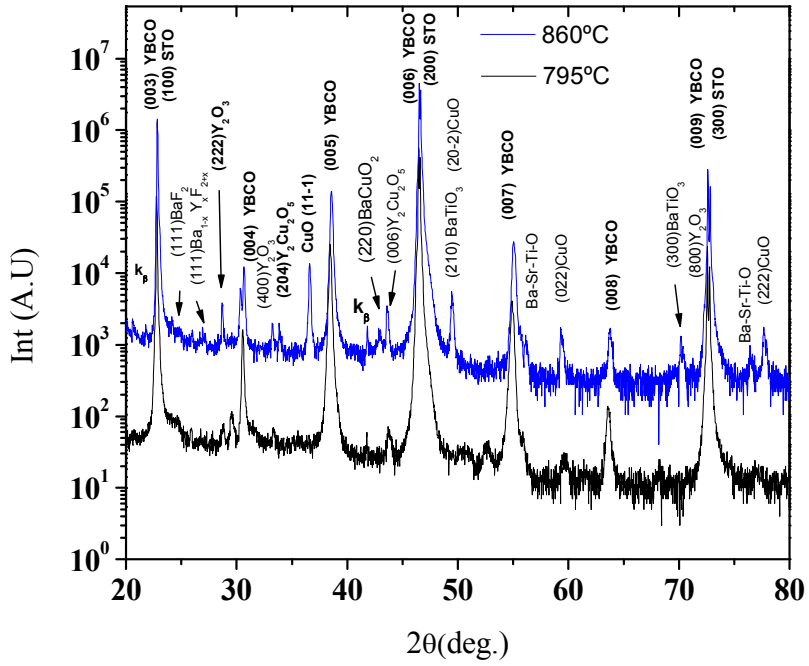

Fig. 4-16 X-ray diffraction θ-2θ scans of YBCO films grown on STO single crystal at 795ºC (black) and 860ºC (blue).

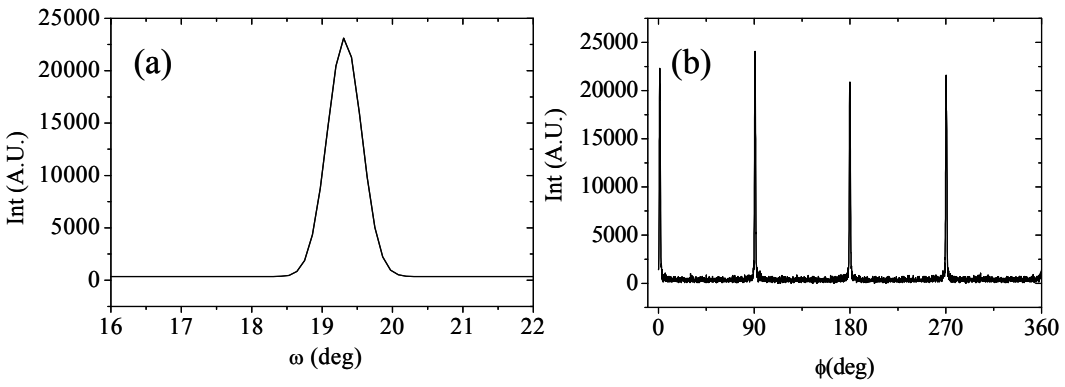

Fig. 4-17 XRD texture analysis performed on TFA-YBCO film grown at 810ºC on STO single crystal substrate.(a) ω-scan (005)YBCO with FWHM= 0.5º and (b) ϕ-scan (102)YBCO with FWHM=2.1º.

4.5.1.2 YBCO/BZO/LAO system

Similar study has been performed on YBCO films grown on BZO/LAO substrates. X-ray diffraction θ-2θ scan was carried out at growth temperatures of 795ºC and 860ºC, shown in Fig. 4-18. In all cases *c*-axis oriented YBCO and BZO films have been distinguished. We have also detected secondary phases like Y_2O_3 and BYF which are associated with growth conditions as we mentioned earlier [99]. Concomitantly, we have investigated in-plane and out-of-plane alignment for YBCO films from ω- and ϕ-scan. We have found that Δω varies from 1.8 to 0.5º by increasing growth temperature, following similar trend as previous systems. By contrast, studying in-plane texture from ϕ-scan (102) YBCO, it has been found that above 800ºC YBCO film only displays out-of-plane texture, see Fig. 4-19 . This is the other evidence of the strong influence of lattice mismatch on YBCO epitaxial growth. It is interesting to note the low intensity of (00*l*) YBCO reflection in comparison with the previous systems. Clearly, the lattice mismatch has a significant effect on the degree of YBCO texture that is developed during the annealing step. For a better understanding of this structural data, it is important to investigate surface morphology for these specimens.

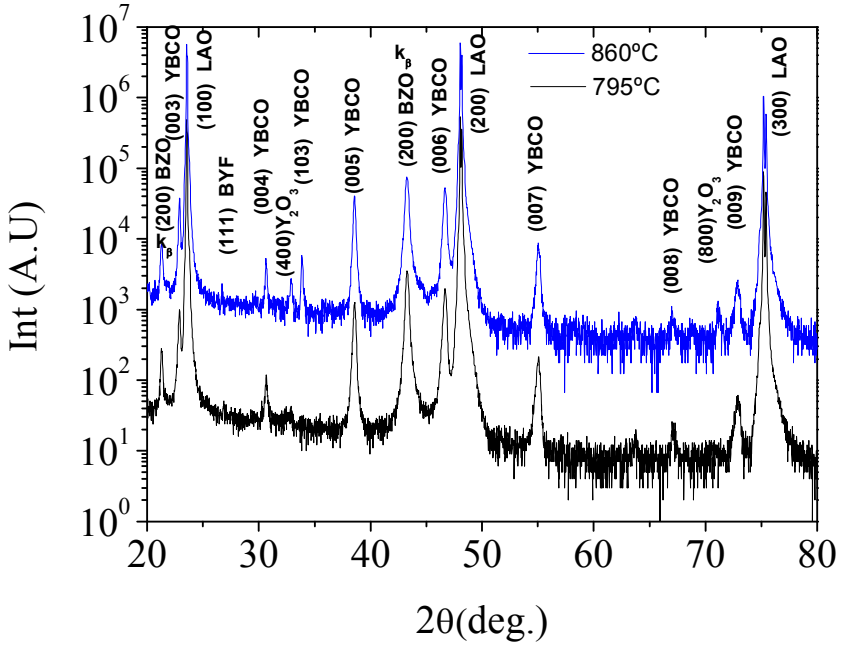

Fig. 4-18 X-ray diffraction θ-2θ scans of YBCO films grown on BZO/LAO substrate at 795ºC (black) and 860ºC (blue).

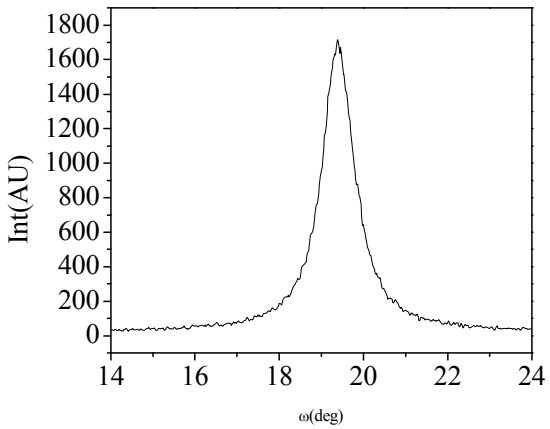

Fig. 4-19 XRD (005) ω-scan for a TFA-YBCO film grown on MOD-BZO/LAO substrate at 810ºC with FWHM= 0.9º

4.5.2 Morphological characterization

Through the SEM observation of the YBCO shown in Fig. 4-20 and Fig. 4-22, the differences in the processing temperature and lattice mismatch between YBCO and the underlying substrate or buffer layer were recognized.

4.5.2.1 YBCO/STO system

TFA-YBCO film grown on STO substrate follows a similar trend as TFA-YBCO grown on LAO single crystal substrate. As shown in Fig. 4-20(a), the microstructure after heating to 795ºC consisted of a continuous and slightly porous film with a roughness determined by AFM around 50 nm. After heating to 860ºC the film contains strongly faceted holes, the dewetting phenomena, Fig. 4-20 (b). Like in the previous system (YBCO/LAO) borders of discontinuous layers follow (100) and (010) substrate planes. Fragments of film covering the substrate are *c*-axis oriented with smooth surface, quasi bi-dimensional, rms around 5 nm, as could be appreciated from AFM analysis shown in Fig. 4-21. In addition, from Fig. 4-21(b) it is also detected the as mentioned mass accumulation near the edges of these holes.

The analysis of the dewetting process in STO single crystals indicated a slightly higher tendency to form holes than with LAO, as it was expected from the higher lattice mismatch of YBCO with STO and supporting the free energy stability model proposed above, Fig. 4-13(b).

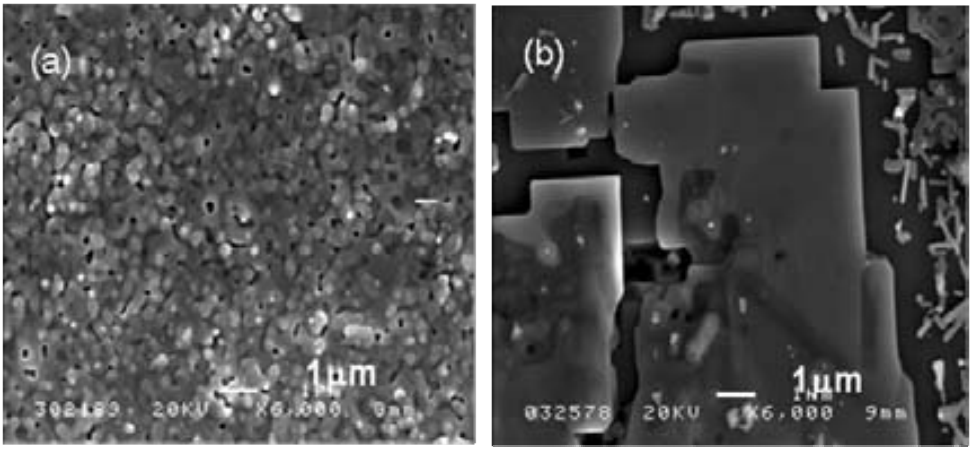

Fig. 4-20 Series of SEM micrographs of the TFA-YBCO film grown on STO single crystal (a) at 795ºC, (b) at 860ºC .

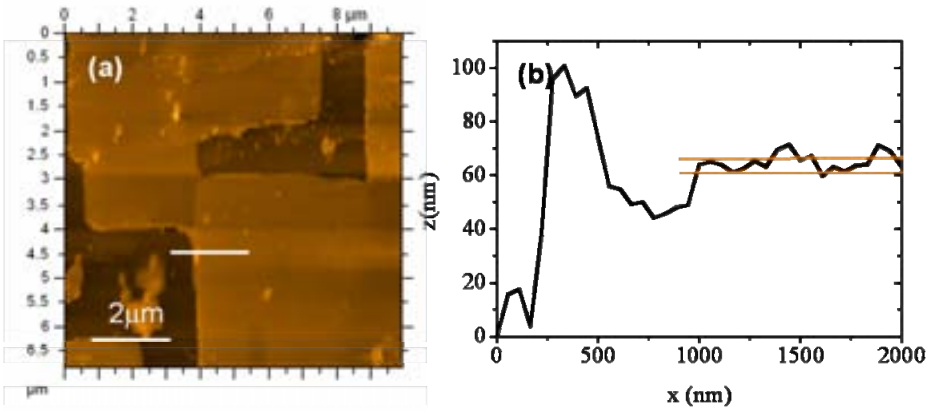

Fig. 4-21 AFM analysis of YBCO film grown on STO single crystal at 860ºC (a) topographic AFM image (b) height profile scan performed on the topographic AFM image.

4.5.2.2 YBCO/BZO/LAO system

We now turn to study YBCO film stability on MOD-BZO buffered LAO single crystal. Here, in contrast with the previous systems studied, at 790ºC strong dewetting effect is already observed, Fig. 4-22 (a), while sparsely distributed YBCO islands with parallepipedic shape and

sizes in the range ~0.1-10 μm are formed at 860ºC, Fig. 4-22 (b). As it is clearly evidenced, a strong enhancement of the dewetted area occurs in the case of BZO/LAO.

We should note as well that, in addition to the most stable parallepipedic islands having {100} surfaces, we can also observe a few of them oriented at 45º. These islands can correspond either to a YBCO crystal with a texture ⟨100⟩ YBCO || ⟨100⟩ BZO, and so being defined by {110} faces, or to a texture ⟨100⟩YBCO || ⟨110⟩BZO, and so being defined by 100 faces [46]. A detail of these 45º oriented crystals can be appreciated in the inset included in Fig. 4-20 (d).

The analysis of the dewetting process in BZO indicated a higher tendency to form holes than with LAO and STO, in agreement with the higher interfacial energy expected on the basis of the corresponding lattice misfits. In conclusion, our experimental results appear to be in a qualitative agreement with the trends of the free energy model reported above [146].

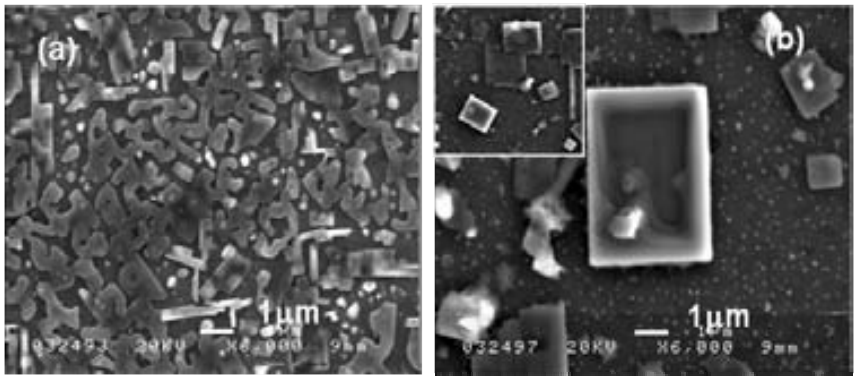

Fig. 4-22 Series of SEM micrographs of the TFA-YBCO film grown on BZO/LAO substrate at 790ºC, (b) at 860ºC .

4.6 Influence of the YBCO synthesis process on the dewetting phenomena

It is generally assumed that thin films will remain stable during their use. However, here in this work we have shown that TFA-YBCO films grown by the solution precursor method are not always thermodynamically stable and that they can uncover the substrate during a high temperature heat treatment. We have also tested if the same phenomena occurred on YBCO films deposited by vacuum techniques in order to know if the reported analysis has a wide validity. To carry out this work, in collaboration with Dr. Ron Feenstra from Oak Ridge National Laboratory, Tennessee, we studied the stability of YBCO film deposited by ex-situ growth of PVD BaF_2 ex-situ process 1.2.3.2.1. We also investigated the YBCO film stability deposited by rf-sputtering, this study was performed from samples supplied by Prof. Jacobo Santamaria from Universidad Complutense de Madrid, Spain.

4.6.1 Physical vapor deposition (PVD) BaF_2 ex situ process for YBCO film

YBCO films of thickness 210 nm were grown on (100) $SrTiO_3$ single crystal substrates. Precursors were formed by e-beam evaporation and converted using ex situ annealing. Films were converted at 750ºC, $P(O_2)$= 0.02kPa ,1.33 kPa of $P(H_2O)$ with a V_g= 0.11 m s^{-1} for 50 minutes. As it can be seen in Fig. 4-23 (a) it presents a homogeneous and continuous surface characterized with the *c*-axis oriented microstructure and also with porous features. Increasing heat treatment to 900ºC for 12 hours and keeping constant the other growth parameters, films undergo a dramatic change. From Fig. 4-23 (b) we observed that the film breaks up into isolated islands and expose the substrate surface. Here, elongated grains are the preferred crystallization shape in contrast with the parallepipedic-like structure generated in YBCO chemical solution de posited.

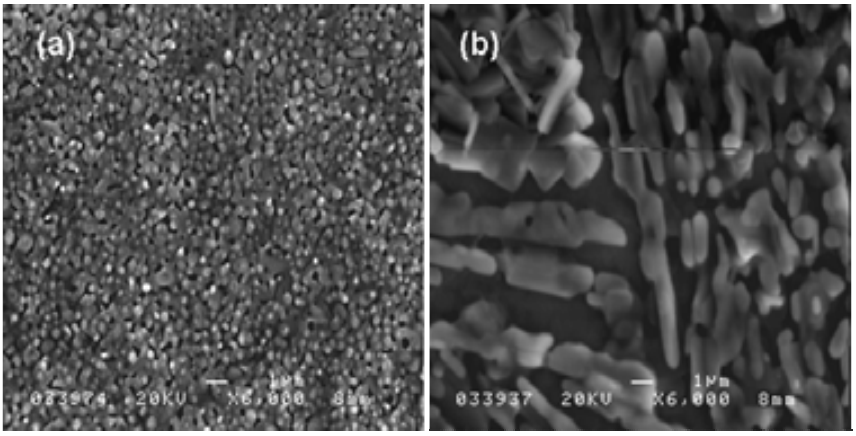

Fig. 4-23 SEM micrographs of YBCO grown by vacuum techniques (a) Film grown by PVD BaF_2 ex-situ technique at 750ºC for 50 min;(b) film grown by PVD BaF_2 ex-situ technique at 750ºC 50 min and post-annealed at 900ºC during 12 hours;

Before to conclude this section, we would like to note that YBCO fabricated by physical vapor deposition BaF_2 ex situ process was also deposited on MOD-BZO buffered LAO single crystal [91]. It has been modified temperature, gas flow rate, oxygen partial pressure and water partial pressure. Unfortunately, like in YBCO film deposited by chemical route, it was impossible to obtain YBCO film biaxially textured. When this films were then heated at higher temperature (~900ºC 12 h) they broke up into isolated grains that possess a low interfacial energy. As we expected, a morphological instability occurred leading to a more disordered surface microstructure, as it can be appreciated in Fig. 4-24 [91].

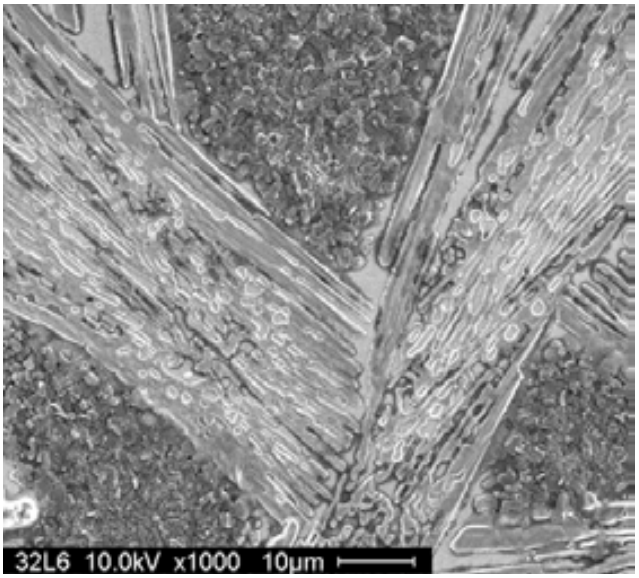

Fig. 4-24 SEM micrograph of YBCO film grown by PVD BaF_2 ex-situ technique on MOD-BZO buffered (100)LAO single crystal grown at 750ºC and post annealed at 900ºC for 12 hours.

Thus, these experimental results confirm that continuous layer of YBCO deposited by PVD BaF_2-ex-situ process is also a metastable state limited by diffusion kinetics which evolves toward a new equilibrium state, dewetted film, under high temperature (900ºC) and prolonged annealing time (12h).

4.6.2 YBCO film grown by sputtering technique

High quality YBCO films were grown by high-pressure sputtering ($P(O_2)$=0.36 kPa) on $SrTiO_3$ substrates at 900ºC. Film thickness was kept in the range 100-200nm. As can be observed from Fig. 4-25 (a) compared to YBCO film deposited by PVD BaF_2 process and TFA-MOD, this YBCO film exhibits a denser surface microstructure and apparently smoother, with some precipitates randomly distributed on it.

Subsequently the as-received films have been submitted to a post annealing treatment at 900ºC for 12 hours. The microstructure after annealing, as it can be shown in Fig. 4-25 (b), consisted of some large and irregular islands, which lead ~30% of the substrate uncovered. As was already seen for YBCO films grown by PVD BaF_2 process, we do not observe the geometrical cavities. However, the formation of spontaneously dewetten structures has been demonstrated in both CSD and vacuum deposited YBCO films. For a full understanding of this stress-induced dewetting pheonomena, a complete analysis of the growth dynamics should be required for this vacuum deposited YBCO film.

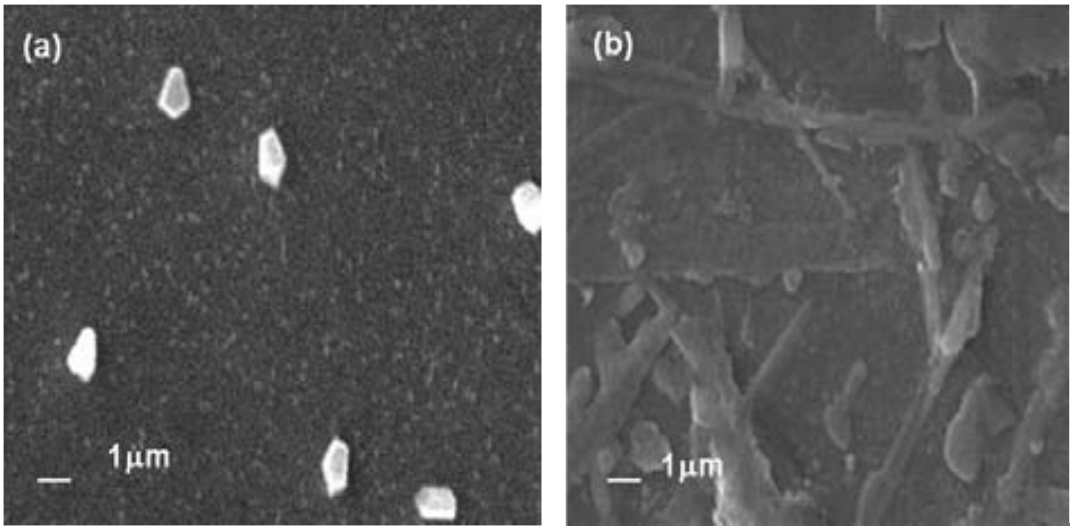

Fig. 4-25 YBCO film deposited on (100) LAO single crystal substrate by rf-sputtering (a) at 900ºC and $P(O_2)$=0.36 kPa (b) post processed at 900ºC for 12 h.

4.7 Conclusions

In conclusion, we have shown that the homogeneous and flat structure of heteroepitaxial TFA-YBCO films is unstable and we have demonstrated that under certain conditions of film thickness and growth or post-processing annealing temperatures strongly dewetted films can be generated. Moreover, we have also proved that such morphological instabilities occur in YBCO films deposited by vacuum techniques (i.e. PVD BaF_2 ex-situ and sputtering).

The film instability has been demonstrated to be a mechanism to relief the stress induced at the interface by the lattice misfit between the YBCO film and the single crystal substrates $LaAlO_3$, $SrTiO_3$ or the $BaZrO_3$ buffer layers. We have also shown that the non-continuous films are actually metastable and so the observed structures are kinetically-limited by atomic diffusion. Microstructural analysis with TEM has confirmed that clean interfaces are obtained where the interfacial stress is strongly relaxed through the formation of misfit dislocations. Cross sectional TEM analysis have demonstrated that the YBCO migration process is complete in the dewetted areas, even for film thickness as high as ≈ 100-150 nm. The arrangement of the dewetted areas has been found to display well defined geometrical features, with parallepipedic-like shapes, either for the dewetted areas or for the islands, indicating that the surface energy of {100} faces is relatively low. The sharpness of the new generated {100} surfaces and the high crystallinity of the YBCO film has been confirmed by cross section TEM images.

Finally, we have reported a free-energy analysis of the film instability which establishes a rationale of the observed phenomena. It has been shown that a certain film thickness is needed to reach a continuous film and also that the instability of atomically flat film structures is promoted by the enhancement of the interfacial elastic energy of the heterostructure when the lattice mismatch is increased.

CHAPTER 5

All-chemical high-J_c $YBa_2Cu_3O_7$ multilayers with $SrTiO_3$ as cap layer

5.1 Motivation

Perovskite thin films prepared by chemical solution deposition (CSD) are finding increasing use in applications ranging from buffer layers for the integration of high-temperature superconductors onto biaxially textured nickel substrates [50,162], to multifunctional highly integrated CMOS-based devices, such as non-volatile memories [163], voltage-tunable microwave filters[164], and pyroelectric imaging arrays [165].

$SrTiO_3$ (STO) perovskite structure has been selected as a potential cap layer for YBCO coated conductor because the lattice misfit between STO and YBCO is about 1.5% and can act as an oxygen barrier to prevent the uncontrolled oxidation of Ni substrate. Indeed, studies have documented successful deposition of YBCO on STO single crystal substrates exhibiting J_c values > 1MA cm^{-2} at 77K [57,166,161] as well as on STO buffer layers [160]. More important

is that it was demonstrated its use as single buffer layer (Nb-doped) on Ni tapes [167] and on IBAD MgO even with a lattice misfit as high as about 7.4% [162,168].

Another potential architecture for coated conductors that should not be overlooked relies in the fabrication of oriented NiO templates through surface oxidation epitaxy (SOE) because it prevents the oxidation of Ni substrate under oxidizing atmosphere [24,169]. Utilization of a second buffer layer is necessary to ensure epitaxial growth of the YBCO as well as to prevent Ni contamination of the superconducting layer. In that metallic substrate, perovskite $BaZrO_3$ (BZO) can be used as intermediate buffer layer due to its excellent lattice matching with NiO that allows cube-on-cube epitaxy as recently proved [47,46]. Even tough PLD-YBCO has been successfully deposited on top of MOD-BZO/SOE-NiO/Ni resulting in epitaxial layer with J_c up to 1 MA cm^{-2} [47], we demonstrated in the previous chapter that TFA-YBCO does not grow epitaxially on MOD-BZO due to the large lattice mismatch (ε=8.11%) [91]. Here, STO arises quite naturally as the main and more logical approach for the cap layer.
Thus, it seems clear that perovskite architectures deserve more importance in coated conductor technology.

While to date best results on multilayered system have been obtained reproducible using vacuum techniques, the study of an inexpensive MOD-perovskite multilayers have been very scarcely explored. The challenge of this chapter is to obtain an all-chemical multilayer-perovskite system in which superconducting YBCO film is grown by TFA route and buffer layers grown by metalorganic decomposition (MOD). Therefore, it is important to investigate the dictating aspects of high quality buffer growth and the relationship between growth conditions of the buffer layer and the possible influence on the final superconducting properties.

Epitaxial growth of ^{TFA}YBCO/ ^{MOD}STO/^{MOD}BZO/LAO system is not straight forward because of the increased interface energy originated form the combination of layers with different lattice parameter, atomic position, thermal expansion coefficient and surface roughness. Therefore, the multilayered system has been generated in different stages. (1) STO buffer layer growth on single crystal substrate as a model system, (2) Optimization of STO buffer layer growth on ^{MOD}BZO-buffered LAO single crystal substrate, and finally (3) TFA-YBCO deposition on ^{MOD}STO/^{MOD}BZO/LAO.

5.2 Chemical solution deposition of STO on (100)-LAO and on (100)-STO single crystals

As a first step towards multilayers growth, following the work previously started in our laboratory [139,134], we concentrated on growing 35 nm epitaxial MOD-$SrTiO_3$ (STO) buffer layer deposited either on STO single crystal substrate (homoepitaxy) or on LAO single crystal

substrate (heteroepitaxy), see 1.2.1.1. Both substrate materials have the same crystal structure and almost the same lattice constant (see Table 1.I). Since phase evolution and crystallinity of STO buffer layer cannot be distinguished from the STO single crystal substrate, structural characterization (XRD analysis) will be carried out only on the heteroepitaxial sample. The deposition of STO buffer layers has been described in detail in 3.3.2 and the growth was performed at the optimized temperature of 700ºC on both substrates (100)-LAO and (100)-STO. The other growth parameters remained constant (95%Ar/5%H_2 (Ar/H_2) atmosphere, dwell time = 4h, heating ramp 200 ºC h^{-1}).

To easily index the samples studied in this chapter, they have been described by two parts: two or three characters and one number, for example SL700. The first character denotes the cap layers (S from $SrTiO_3$) and the second character identifies the single crystalline substrate (L from $LaAlO_3$). The number identifies the buffer layer growth temperature (i.e. 700ºC). Accordingly, SS700 and SL700 will be the samples examined in the next section.

5.2.1 Structural characterization

A typical x-ray diffraction θ-2θ scan for STO single layer deposited on LAO single crystal is shown in Fig. 5-1. The peaks appearing at 46.5º and 72.6 belong to the $SrTiO_3$ buffer layer (*h*00) reflection, whilst, the peaks appearing at 23.4º, 47.9º, 75.1º belong to the (*h*00) reflections of $LaAlO_3$ single crystal substrate. Sharp and weak peaks at 2θ = 21.3, 43.1º and 66.7º corresponds to k_β reflection from the substrate.

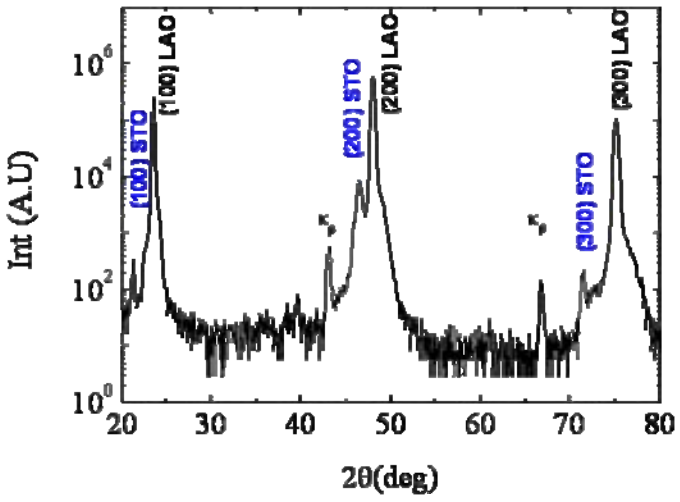

Fig. 5-1 XRD θ-2θ pattern of MOD-STO buffer layer grown on LAO single crystal for 4 h in Ar/H_2 atmosphere at 700ºC .

Out-of-plane and in-plane texture analysis were carried out from ω-scan of (200) STO peak and ϕ-scan of (202) STO peak. The results are illustrated in Fig. 5-2. In both cases, excellent texture is achieved with out-of-plane FWHM of 0.2º and in-plane texture FWHM of 0.8º±0.1.

FWHM values of ϕ-scan and ω-scan have been summarized in Table 5-I. Compared to STO buffer layers deposited by PLD on LAO single crystal substrate, similar or even improved grain alignment has been obtained by solution deposition approach [170].

From these results we assumed that samples SS700 also display an excellent crystalline quality. However, it will be verified by depositing TFA-YBCO film on top (see section 5.3).

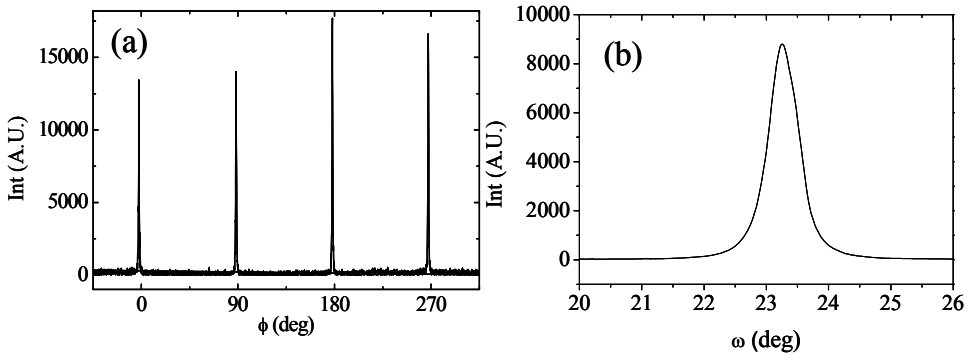

Fig. 5-2 XRD texture analysis of SL700 (a) ϕ-scans with Δϕ(202)=0.8º and (b)ω-scans with Δω(200)=0.2º.

Table 5-I FWHM of ω-scan from (200) STO peak and ϕ-scan from (202) STO peak of MOD-STO cap layer grown on (100)-LAO single crystal substrate at 700ºC.

Substrate	$SrTiO_3$ buffer T_{growth} (ºC)	FWHM $\Delta\omega_{STO}$ (200)	FWHM $\Delta\phi_{STO}$ (202)
$LaAlO_3$	700	0.2º	0.8º

5.2.2 Morphological characterization

In Fig. 5-3 it is shown the surface morphology of homoepitaxial and heteroepitaxial samples analysed by AFM. It is clear that both systems follow a similar trend and are crack-free. Height profile scan reveals that the morphology of the grains is regular and has globular shape with a

mean grain size of: 50±5 nm. However, at the junction of the boundaries and the surface, there is usually a groove which is formed by the requirement of the energy balance between boundary and surface.

Over an area of 2 μm x 2 μm, the average root mean square (rms) surface roughness (see section 2.1.1.) of STO buffer layers deposited on (100)LAO is about 0.9 nm and on (100)STO is 1.1 nm (Fig. 5-3). To perform a complete characterization of the buffer layer surface we have carried out a quantitative estimation of the atomically flat surface. This parameter, contrasting with rms, rules out the groove contribution and therefore provides a strictly value of flat grains. For the computation of the atomically flat area, we have defined the value of 1.14 nm as threshold value for flat area (3 STO unit cells). Then it has been applied a binary operator on the AFM topographic image resulting an image as the one shown in Fig. 5-4 where the blue area corresponds to flat grains. Detailed procedure is described in section 2.1.1.

In both cases we have obtained that around 65% of surface area is occupied by flat grains (62% for SL700 and 68% for SS700). In this case, since surface morphology is very homogeneous for both samples, similar rms value is correlated with similar percentage of flat area and therefore, it makes no difference using rms or percentage of flat area to characterize surface morphology. However, this connection should not be always accomplished, it depends on the nature of the buffer layer as will be discussed in chapter 6 and 7.

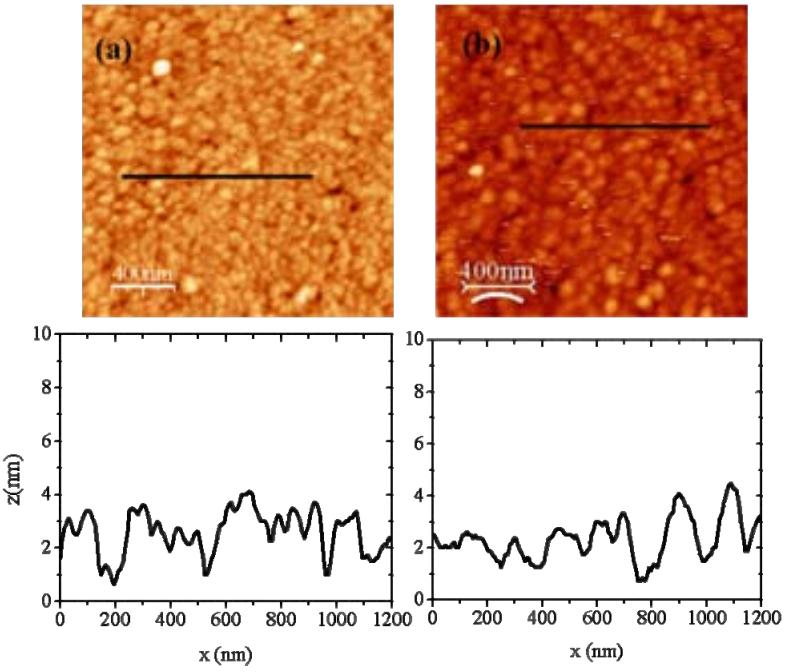

Fig. 5-3 AFM analysis of the MOD-$SrTiO_3$ layers (a) SL700, (b) SS700

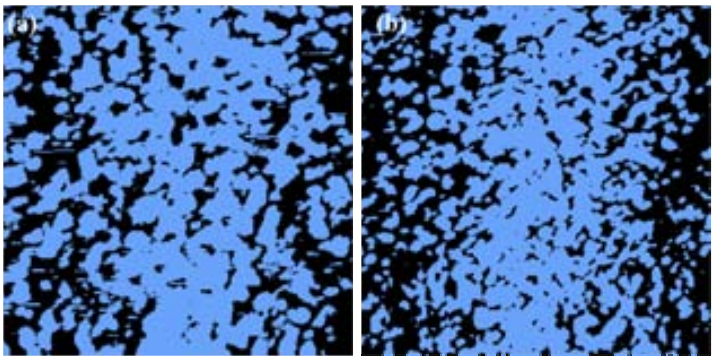

Fig. 5-4 Binary images of (a) SL700 with 62 % of flat area and (b) SS700 with 68% of flat area

In conclusion, we successfully grew high quality STO buffer layer homoepitaxially on STO single crystal substrate and heteroepitaxially on LAO single crystal substrate by chemical solution deposition. The optimized growth temperature of 700ºC yielded smooth STO surface with percentage of flat area around 65% and sharp texture. Now, to study the critical effect of buffer layer surface on YBCO film quality, we systematically deposited YBCO film by TFA route on the as- described STO cap layers.

5.3 TFA-YBCO on MOD- STO on (100)-LAO and (100)-STO single crystals

TFA-YBCO was grown on the above homoepitaxial and heteroepitaxial samples following the experimental procedure described in Chapter 3. The TFA solution was prepared from the dissolution of solid YBCO ceramic powder in the trifluoroacetic acid, described in detail in 3.1.1.2. These films were then calcined following a heating treatment reported in 3.1.2-4. In the present work, we maintained the growth parameter values optimized for LAO single crystal: T=795ºC, $P(H_2O)$= 0.6kPa, $P(O_2)$=0.02kPa, gas flow rate =2,03x10^{-2} ms^{-1} and the total reaction time of 180 min [99].

5.3.1 Structural and morphological characterization

Typical X-ray diffraction θ-2θ scan of the resulting TFA-YBCO film deposited on SL700 and SS700 are shown in Fig. 5-5. Sharp and intense (00*l*) reflections indicate that YBCO film is *c*-axis oriented with no detection of (*h*00) YBCO peaks, i.e. a-axis grains. We have detected an extra Bragg line peak around 2θ ≈ 31.7º and shoulder peak at 2θ ≈ 45.4º. They have been assigned to Ba-Sr-Ti-O secondary phase [20]. It is a clear indication that there exists interface

reaction between YBCO and STO, being well consistent with previous results obtained on STO single crystal (Fig. 4-16) and further supported by other authors [166,171,91]. Other secondary phases that have been also detected in this XRD θ-2θ scan are: BaF_2, $Ba_{1-x}Y_xF_{2+x}$ (BYF), $BaCuO_2$ and CuO.

Considering the decomposition pathway by which YBCO film typically forms (see 1.2.3.1.4), the identification of BaF_2 and BYF is a clear indication that intermediate phases have not been fully converted to YBCO [71]. On the other hand, the presence of $BaCuO_2$ and CuO are consistent with the need to place excess of Cu from interface reaction. For the same reason we also assume that exist $Y_2Cu_2O_5$ phase, however, its most intense reflection matches with Ba-Sr-Ti-O Bragg line reflections and could not be distinguished from our XRD θ-2θ scan. The diffraction peaks (*h*00) of STO thin film can not be separated from (00*l*) YBCO peaks because of limited resolution in the θ–2θ scan spectrum.

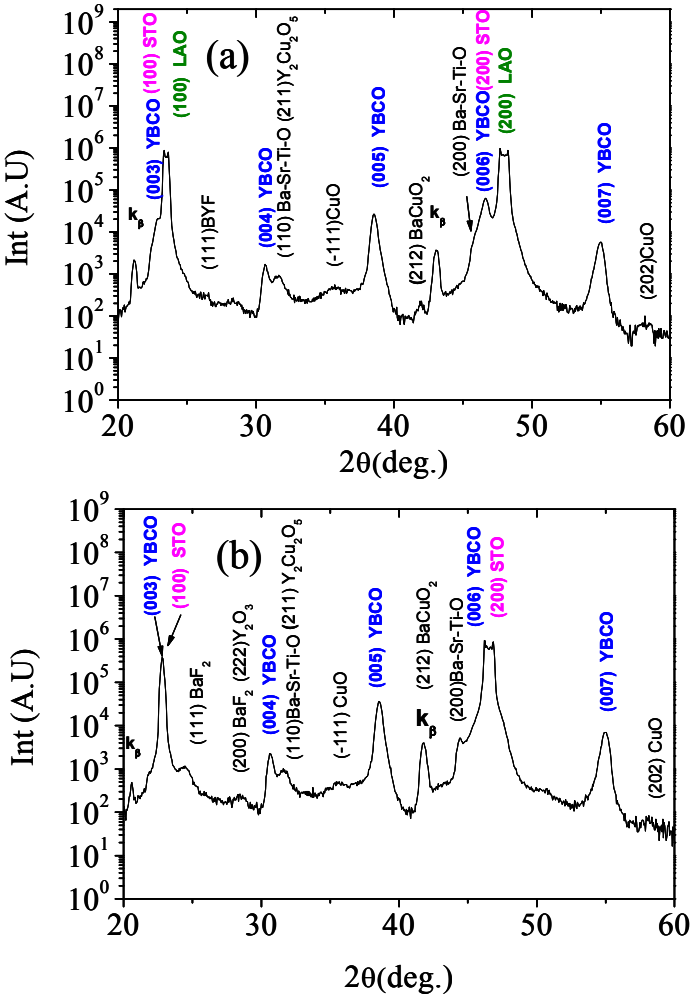

Fig. 5-5 x-ray diffraction θ-2θ scan of YBCO grown at 795ºC, $P(H_2O)$=0.6kPa, $P(O_2)$=0.02kPa on (a) SL700 and (b) SS700

To examine the epitaxial growth of YBCO layer on SL700 and SS700 and determine the transfer of the underlying textured crystalline alignment, XRD ϕ-scan from (102) YBCO peak and ω-scan from (005) YBCO peak were taken, see Fig. 5-6. From Δϕ (102) and Δω(005) values displayed in Table 5-II, we observe similar crystalline quality. In both cases, YBCO is biaxially textured independently of the nature of the substrate.

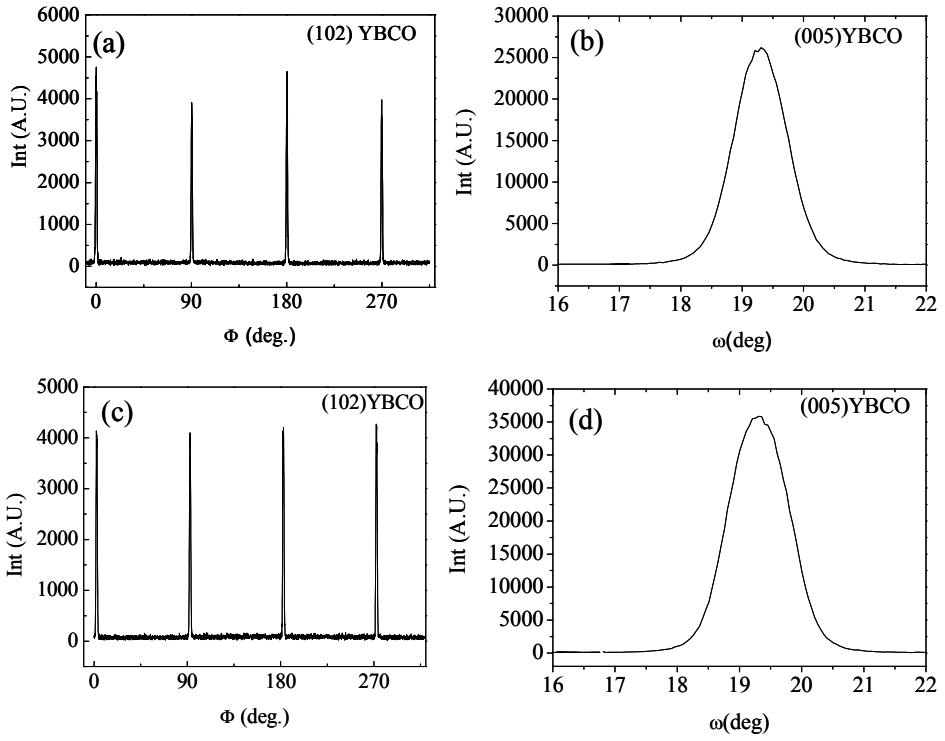

Fig. 5-6 XRD texture analysis of TFA-YBCO film grown on (a-b) SL700 with Δϕ(102)=1.1º and Δω(005)= 0.8º (c-d)SS700 with Δϕ(102)=1.2º and Δω(005)= 0.9º.

Table 5-II Summary of the Δϕ(102), Δω(005) YBCO and electrical resistivity values obtained for YBCO grown at 795ºC at $P(H_2O)$=0.6 kPa, $P(O_2)$=0.02kPa on STO-buffered STO, STO-buffered LAO and on STO single crystal*.

	Buffer T(growth)(°C)	$\Delta\phi_{(YBCO)}$	$\Delta\omega_{(YBCO)}$	ρ_{300K}	ρ_0
Sample	$SrTiO_3$	(102)	(005)	(μΩcm)	(μΩcm)
SS700	700	1.1°	0.8°	460	<7
SL700	700	1.2°	0.9°	650	<10
YBCO/STO*	-	1.3°	0.5°	~300	<2

Examining the surface morphology of YBCO superconducting layer grown on SL700, Fig. 5-7(a), and on SS700, Fig. 5-7(b), it is identified some a-b axis grains in both samples although they have not been previously detected in the XRD θ-2θ scan. Refined XRD analysis should be required to identify them. It is also evidenced the formation of small pores randomly distributed in the film. Additionally, some precipitates identified as $BaCuO_2$ according to XRD θ-2θ scan and preliminary studies of μ-Raman [121] have been observed from surface morphology analysis of YBCO film on SL700 suggesting a more inhomogeneous surface.

The surface morphology of these samples has been compared to TFA-YBCO films grown on STO single crystal substrate under the same growth conditions. From Fig. 5-8 we observe similar density of pores but the concentration of a-b axis grains is strongly minimized. These observed modifications seem to be an interfacial effect pointing out a strong sensitivity of TFA-YBCO film quality with the underlying film.

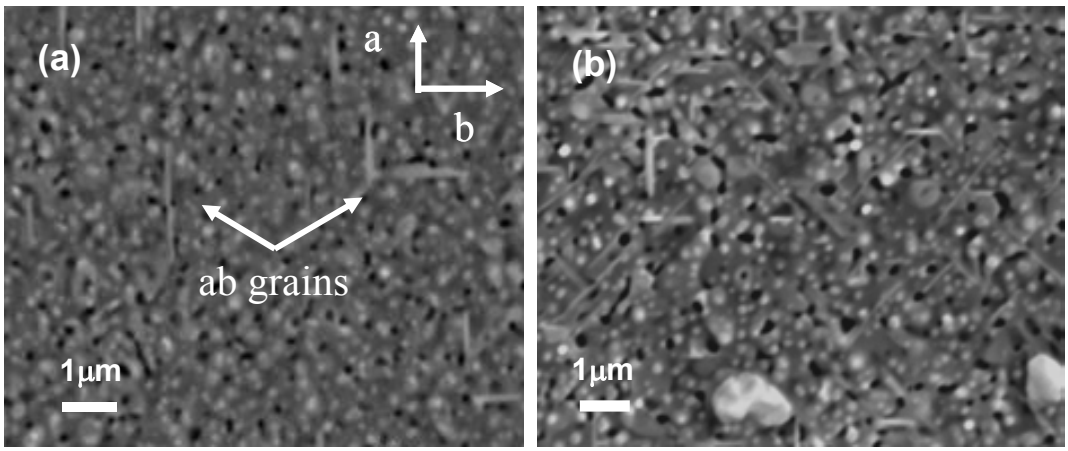

Fig. 5-7 Plan-view SEM photomicrographs of a TFA-YBCO film prepared at 795ºC, 180 minutes, $P(O_2)$=0.02kPa on (a)SS700 and (b)SL700

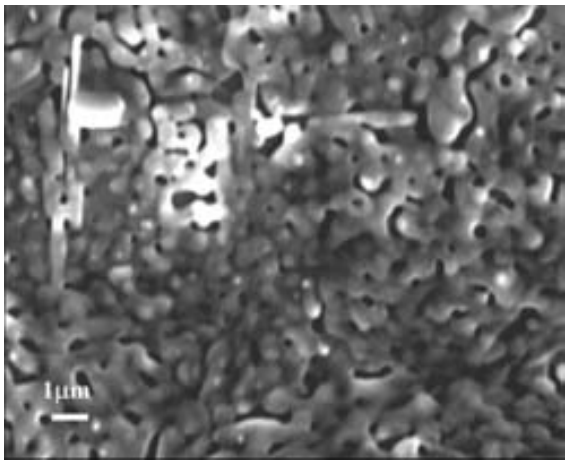

Fig. 5-8 SEM image of TFA-YBCO film grown on STO single crystal substrate at 795ºC for 180 min with $P(O_2)$=0.02 kPa

5.3.2 Superconducting and electrical properties

Critical current density was obtained from these two samples described above. Results have been contrasted with YBCO films grown on STO single crystal substrate (YBCO/STO). We should reiterate that YBCO film was grown in the same conditions regardless of whether the substrate was STO buffered or not (i.e., 795ºC, $P(H_2O)$=0.6kPa, $P(O_2)$ =0.02kPa).

The dependence of critical current densities, J_c, with temperature is similar for YBCO on SS700 and YBCO/STO model system. YBCO on SL700 displays slightly lower values, Fig. 5-9(a). However, it is noticeable that in all cases J_c values at 77K are around 1 $MAcm^{-2}$.

By comparing these results with J_c values of TFA-YBCO films grown on LAO single crystal, (~3MA cm^{-2} at 77K) [34], it is clearly seen that the quality of the TFA-YBCO film on STO system could be further improved. This is in well agreement with previous XRD data where intermediate phases and interface reaction were detected and with SEM image which showed a/b axis grains.

In order to investigate which is the main contribution that could lead to this smooth difference between samples here studied, electrical resistivity measurements were carried out.

From electrical resistivity measurements, shown in Fig. 5-9(b), we can see that all samples exhibit a sharp transition at T=90K indicating a good homogeneity through the sequence of layers. Moreover, linear T-dependence in the normal state regime points out an optimal state doping. No reduction of T_c has been observed as a function of buffer layer quality in contrast to what other authors have been previously reported for MOCVD YBCO thin films where a minimum grain size of the buffer layer on the order of 70 nm was required to obtain high T_c [172].

In our case, the main differences between YBCO films arise from the value of the electrical resistivity at room temperature, ρ(300K), which is higher in the case of SL700 and SS700 than YBCO/STO (650 μΩcm and 560 μΩcm and 300 μΩcm respectively). Referring back the SEM images, see Fig. 5-7, we observe that higher normal state resistivity correlates with a surface morphology characterized by pores and a/b axis grains. In addition, normal state resistivity for YBCO/STO system slightly differs from pore free and fully c-axis oriented YBCO film, i.e. 200μΩcm [173]. Considering that the deterioration of the superconducting properties is mainly by the geometric fact that the effective cross section for current transport is strongly reduced [156], we propose that a/b axis grains and pores are the main factors that degrades resistivity at room temperature. Although the mechanisms involving the formation of pores during film pyrolysis and growth are not completely elucidated, we have recently demonstrated that the presence of a/b axis nucleated grains promotes this residual porosity in TFA-YBCO thin films [49].

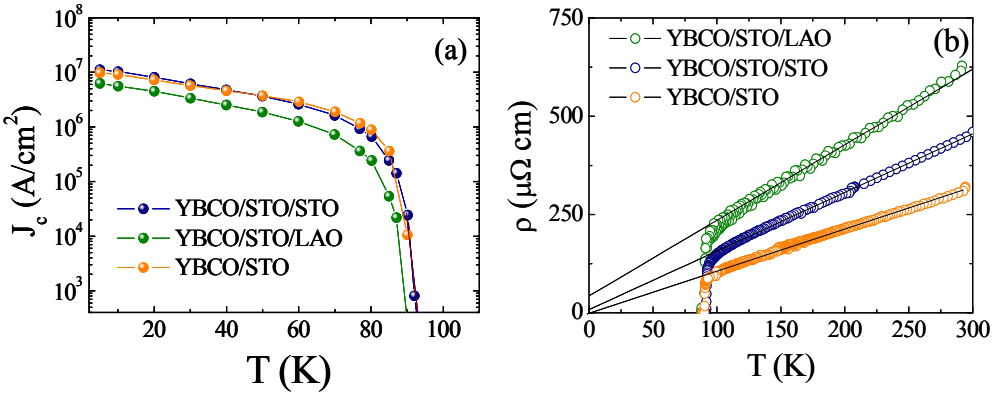

Fig. 5-9 (a) Temperature dependence of the critical current density and (b) Temperature dependence of the electrical resistivity for YBCO film grown on different substrates.

By fitting the experimental curves in the range 150-250K (see solid line in Fig. 5-9(b)), we can obtain experimental estimations of ρ_0 (ρ at 0K) which accounts for any residual resistivity arising from different electron scattering mechanisms, for example, the presence of secondary phases or high-angle grain boundaries [174]. Although some residual resistivity has appeared in buffered samples, it is easily observed that the main increase of resistivity appears at 300K.

Since SS700 and SL700 buffers exhibited very low surface roughness (~ 65% of flat area) as well as high texture quality, it is likely that the interfacial effect should be overcome by modifying YBCO growth parameters as we anticipated from XRD, SEM and J_c measurements. In fact, more recent optimization carried out in our laboratory has demonstrated that increasing growth temperature, we minimize a-axis grain nucleation and consequently the superconducting properties could be enhanced [91]. However, an optimization process is required for this particular system to study the stability of the MOD-STO buffer layers with respect to the TFA-YBCO film since as we already mentioned interface reaction exist between YBCO and STO.

5.4 Chemical solution deposition of MOD-STO on MOD-BZO buffered (100)-LAO single crystals

As it was mentioned in the introduction paragraph for some conductors architectures it can be useful to grow double buffer layers with lattice parameters matching both the substrate and the superconducting YBCO layer. Therefore, to generate such conductors through an all-chemical multilayered approach we have investigated a double buffer layer with one of them

having a low lattice mismatch with the metallic substrate, i.e. a BZO buffer layer which is a suitable material to deposit on NiO or IBAD-MgO. However, in this thesis we have studied a model system architecture depositing BZO directly on LAO single crystal substrate which has a strong lattice mismatch (ε^{BZO}= - 9.5%) and then STO has been deposited on BZO, also with strong lattice mismatch (ε^{STO}=7.1 %) .

To prepare this multilayered architecture we have deposited BZO buffer layer directly on (100)-LAO single crystal substrate and annealed at two different temperatures (700ºC, named BL700 and 850ºC, named BL850) for 4 h in Ar/H_2 atmosphere (see section 3.3.1). Subsequently, MOD-STO buffer layer was deposited on top of the as mentioned MOD-BZO buffer layers at 700ºC for 4 h in Ar/H_2 in accordance with the results obtained in section 5.3. As we stated before, STO buffer is used to reduce the lattice misfit between the barium zirconate and the YBCO (Table 1-I). In this case, reminding that STO layers were grown in both cases at 700ºC, samples will be identified referring to BZO annealing temperatures, i.e. SBL700 and SBL850.

5.4.1 Structural characterization

We note that to acquire the XRD θ-2θ scan, Ni filter was used because k_β peak from the substrate matches with (*h*00) peak reflections of BZO. For both samples, in the θ-2θ XRD scans only the (*h*00) peak reflection of $BaZrO_3$ and $SrTiO_3$ are observed, showing a strong c-axis orientation for both layers. Fig. 5-10 shows a typical XRD θ-2θ scan for STO/BZO/LAO system. While this particular film was SBL700, it is also representative of those usually obtained for SBL850.

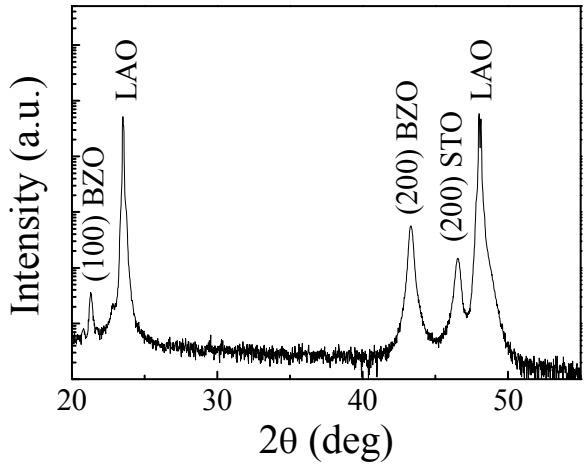

Fig. 5-10 X-ray diffraction pattern for a three-layer: MOD-STO on MOD-BZO-buffered (100)LAO single crystal substrate. Ni filter was used to record this θ-2θ x-ray pattern.

Structural characterization was further studied by in-plane ϕ-scan and out-of-plane ω-scan of both buffer layers. The results, presented in Fig. 5-11 for SBL700 and in Fig. 5-12 for SBL850 indicate that STO/BZO buffer layers grow nicely biaxially textured on LAO substrates (cube-on-cube) with similar FWHM values of in-plane and out-of-plane texture. It is indicative of a high degree of alignment, particularly for films prepared by a solution deposition approach.

Comparing Δϕ values for STO/BZO/LAO system, STO buffer layer preserves almost the same texture as its underlying buffer layer BZO despite high lattice matching, which is near the limit for growing a high-quality epitaxial film. Table 5-III highlights these results. On the other hand, it is worthy of remark that the degree of STO texture for STO/BZO/LAO system is slightly higher compared to STO/LAO or STO/STO systems (Table 5-I).

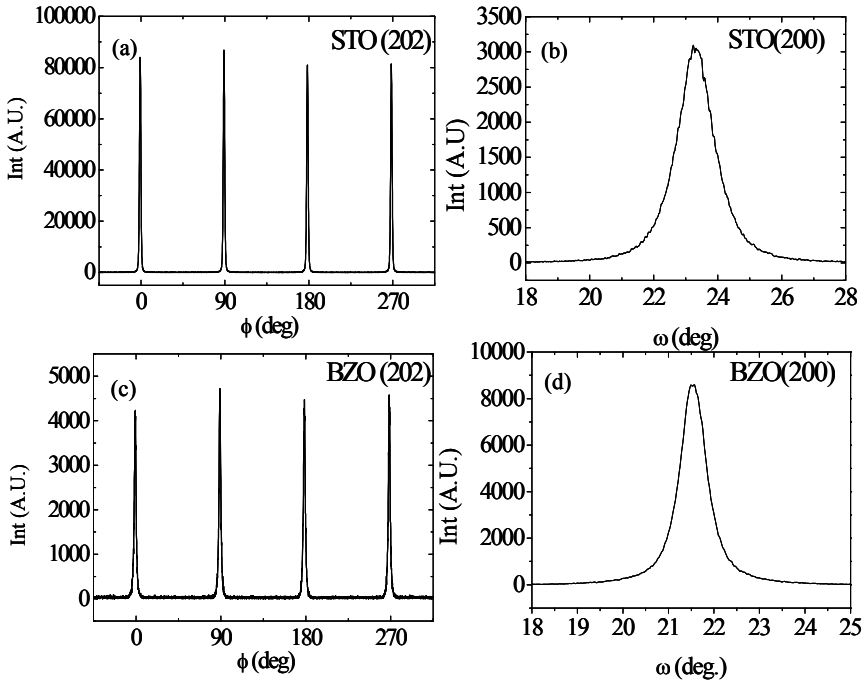

Fig. 5-11 XRD texture analysis of STO/BZO/LAO multilayered system (SBL700) (a) ϕ- scan obtained for STO layer, (b) ω-scan obtained for STO layer, (c) ϕ-scan obtained for BZO layer and (d) ω-scan for BZO layer. FWHM are summarized in Table 5-III.

.

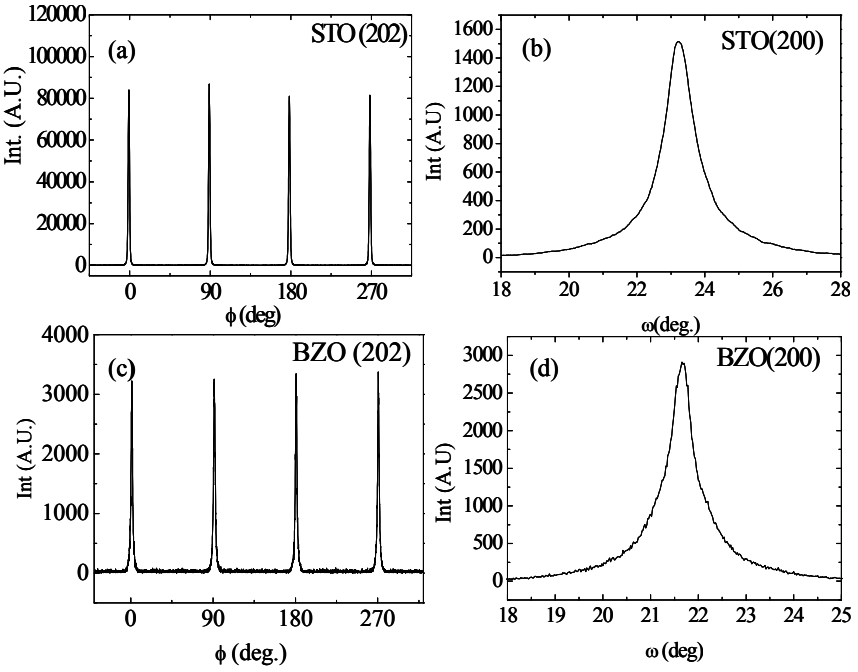

Fig. 5-12 XRD texture analysis of STO/BZO/LAO multilayered system (SBL850) (a) ϕ- scan obtained for STO layer, (b) ω-scan obtained for STO layer, (c) ϕ-scan obtained for BZO layer and (d) ω-scan for BZO layer. FWHM are summarized in Table 5-III.

Table 5-III Summary of the FWHM from ω-scan and ϕ-scan obtained from SBL700 and SBL850.

	Buffer T_{growth} (ºC)		Out of plane (FWHM)	Out of plane (FWHM)	In-plane mosaic (FWHM)	
			$\Delta\omega_{BZO}$	$\Delta\omega_{STO}$	$\Delta\phi_{STO}$	$\Delta\phi_{BZO}$
Sample	$SrTiO_3$	$BaZrO_3$	(200)(±0.1)	(200) (±0.1)	(202) (±0.1)	(202) (±0.1)
SBL700	700	700	0.7º	1.3º	1.6º	2.1º
SBL850	700	850	0.8º	1.2º	2.0º	1.8º

The accommodation of lattice mismatch in perovskite films grown by chemical methods on perovskite substrates was studied in depth by Langjahr et al.[175,151]. There, it was suggested that large lattice mismatches are accommodated by the introduction of an array of misfit dislocations at the interface between the film and the substrate. The dislocations are created at the initial stages of film nucleation when the thickness of the epitaxial layer exceeds a critical value. Once the dislocation network is formed, the epitaxial layer can grow at a much reduced

strain energy [176,175]. They should rearrange to equalize their distances during the coalescence of the different epitaxial grains. Our TEM observations have confirmed the presence of these arrays of dislocations. Fig. 5-13(a) shows a high resolution TEM image of the interface between LAO and a BZO buffer layer where misfit dislocations can be easily identified, marked as ⊤. In this case, lattice mismatch is ε= 9.54%. In our group it was calculated a rough estimation of the average separation between dislocations which coincides fairly well with the expected value for fully relaxed epitaxy, $S = a_{BZO}^2/(a_{LAO} - a_{BZO}) \approx 4.4$ nm. Further verification that perovskite thin films grown by chemical methods, in the present STO/BZO/LAO bilayer system, are fully relaxed is presented in Fig. 5-13(b). Here we show a reciprocal space map around the (103) reflections for the double buffered architecture STO/BZO grown on LAO single crystal.

Qualitatively, the fact that the observed peaks corresponding to the three layers were not aligned with the same $q_{||}$ indicates that the architecture is relaxed. A numerical estimation of the peak positions leads to values of the corresponding lattice parameters, which differ by less than 0.25% with respect to those of bulk specimens. Thus, the above results confirm that chemical solution deposition is a versatile technique for growing epitaxial multilayers of high quality even at important lattice mismatches. The lattice misfit between BZO and LAO is about -9.5% and between STO and BZO is about 7.1% [49]. Note that this relaxed situation can vary depending on the nature of buffer layer and the substrate. For example, MOD-CeO_2 on YSZ single crystal substrate displays a semicoherent interface, as will be presented in Chapter 7.

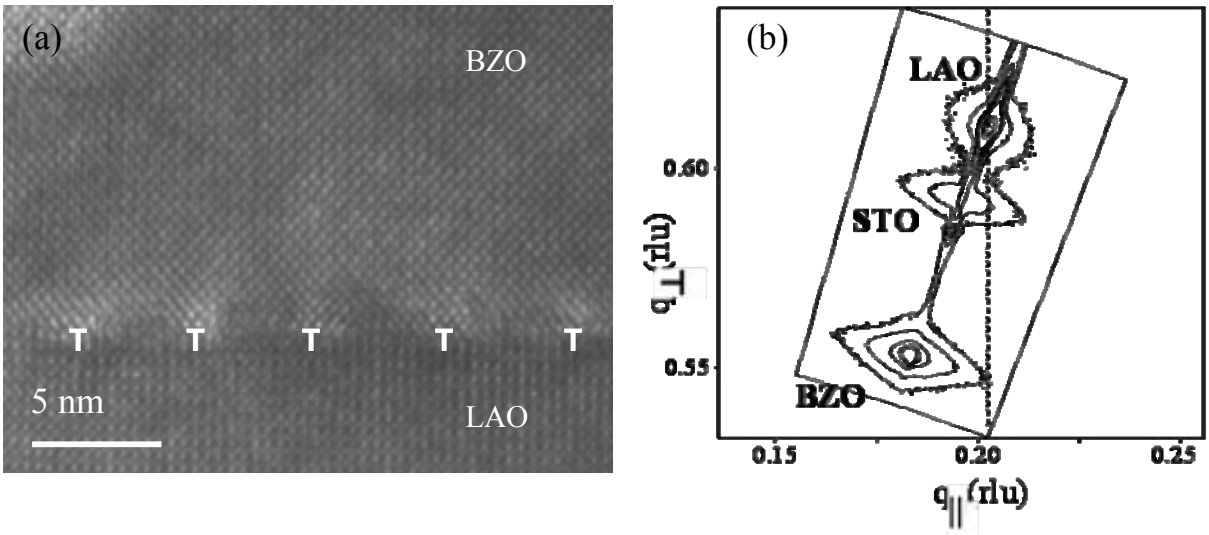

Fig. 5-13 (a) HRTEM image of the interface between a $BaZrO_3$ buffer layer and the LAO single crystalline substrate. The array of misfit dislocations that relax the interface stress can be clearly identified. (b) Reciprocal space map around the (103) reflections for the heterostructure $SrTiO_3/BaZrO_3/LaAlO_3$ of sample SBL700. Quantitative analysis shows that both perovskite buffer layers are totally relaxed.

5.4.2 Morphological characterization

X-ray diffraction investigations showed highly textured STO films, but we are also interested in growing other types of buffer layers or YBCO films on these samples, thus, it is necessary to investigate the surface morphology. AFM analysis was performed on BZO and STO buffer layers, as it can be seen in Fig. 5-14. As a general trend, buffers surface consist of connected globular grains with an average grain size ranging from 56±8 nm for BZO buffer layer to 24±2nm for STO buffer layer. Results of AFM analysis are listed in Table 5-IV. For the sample BL700, Fig. 5-14(a), the grains are homogeneously distributed whereas BL850, Fig. 5-14(b), has some voids and abnormal grains. These abnormal grains could be easily identified in the AFM picture because of its brightness and in the profile scan for their height above the flat surface (~15nm). As a result, STO deposited on BL700 grains are densely packed producing smoother surface with some voided boundaries, Fig. 5-14(c), and STO deposited on BL850 yields to granular but rougher surface, Fig. 5-14(d). In both cases the grains become smaller, 25 nm±2, and there are considerable amount of voided boundaries which contributes to rms value. Similarly to STO single buffer layer system, we have evaluated the percentage of atomically flat area for these samples. Fig. 5-15 shows the binary images obtained from the corresponding AFM topographic images. In sample BL850 it has been required to eliminate beforehand outgrowth contribution by applying a masking operator (procedure described in 2.1.1). After processing AFM images we have obtained that BL700 displays 40% of atomically flat area, BL850 36%, SBL700 41% and SBL850 30%. From these pictures it becomes very clear that percentage of atomically flat area decrease as rms value increase and thus, both parameters can be used indifferently to characterize surface morphology.

It is clear that surface defects in $BaZrO_3$ buffer layer (grooving, outgrowth or precipitates) strongly affect the subsequent $SrTiO_3$ layer. In particular, from the cross section we have observed that surface defects in $BaZrO_3$ lead to heterogeneous $SrTiO_3$ surface morphology.

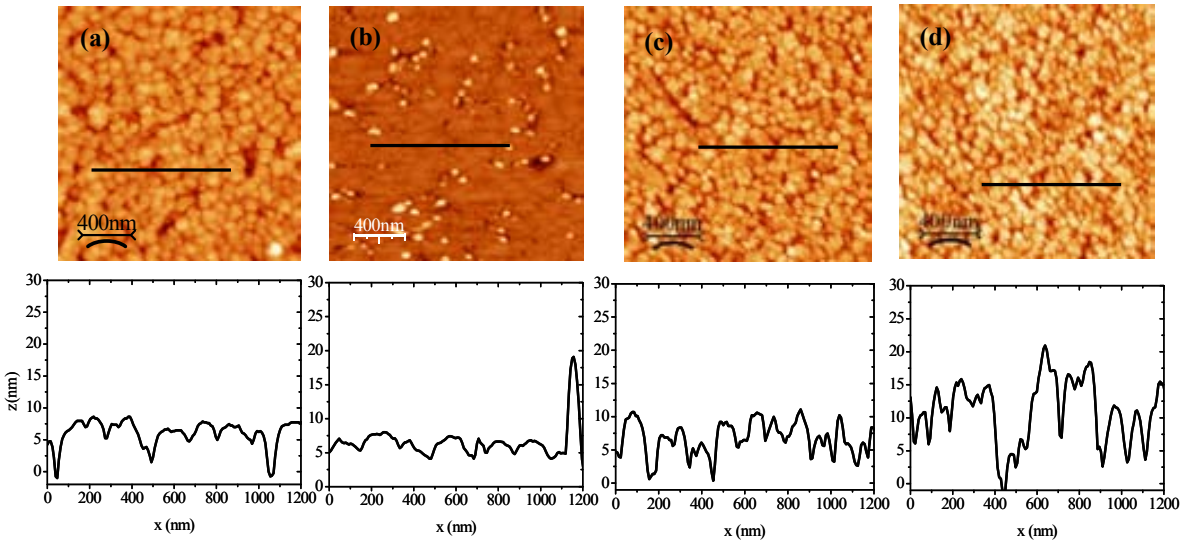

Fig. 5-14 AFM analysis of $BaZrO_3$ and $SrTiO_3$ buffer layers (a) BL700 with rms =2.0 nm, (b)BL850 with rms =2.7 nm, (c) SBL700 with rms =2.4 nm (d) SBL850 with rms=3.4.

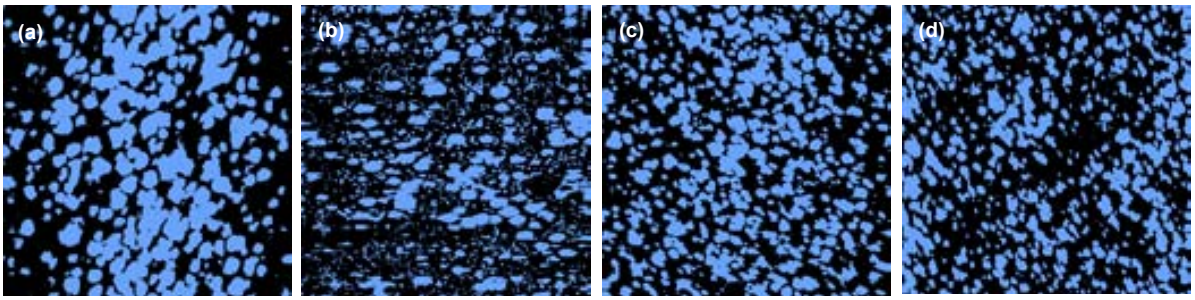

Fig. 5-15 Binary images from the AFM micrograph presented in Fig. 5-14. (a) BL700 with 40% of atomically flat grains, (b) BL850 with 36%, (c) BL SBL700 with 41% and (d) SBL850 with 30% of atomically flat grains.

It is interesting to see how an increased roughness affects the growth of multilayer structures. Fig. 5-16 shows cross section TEM image from an interface between STO and BZO in the case of sample SBL850. We can observe that, even if the interface is not planar, epitaxial STO growth can be achieved on BZO. An important point also to note is that this roughness did not lead to any reactivity between STO and BZO, and clean interfaces were always observed in the multibuffered substrates, being in well agreement with XRD θ-2θ scan data in which we did not detect secondary phases, recall Fig. 5-10. Highly epitaxial STO and BZO layers detected in the cross-sectional TEM images suggested us that no carbon impurities (from metalorganic

precursors) remained in the buffer structure, otherwise, their presence could strongly damage the development of the film epitaxy, as will discuss in chapter 7 for MOD- CeO_2 films.

Table 5-IV Summary of the values obtained for the AFM analysis performed for the samples BL700, BL850, SBL700 and SBL850: rms roughness and percentage of atomically flat area and finally grain size. It is also indicated the buffer layer growth temperatures.

Sample	T(growth) Buffer $BaZrO_3$	T(growth) Buffer $SrTiO_3$	rms (nm) (± 0.1)	% atomically flat area	Grain size (nm)
BL700	700	-	2.0	40	47±2
BL850	850	-	2.7	36	70±5
SBL700	700	700	2.4	41	25±2
SBL850	850	700	3.4	30	24±2

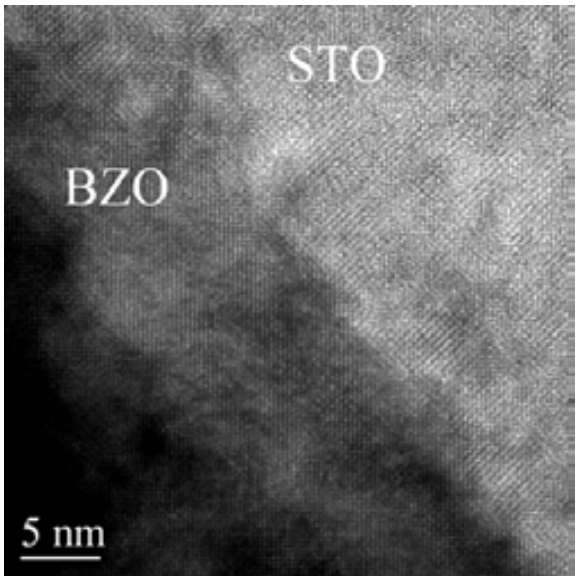

Fig. 5-16 TEM image corresponding to the sample SBL850 in which it is shown MOD-STO/MOD-BZO interface with high resolution. It can be assessed that the interface remains relatively abrupt with no evidence of interface reaction.

In conclusion, XRD reveals a perfect epitaxial growth of multilayered system with no significant differences for the two heat treatment temperatures. By means of AFM it is suggested that SBL700 is a suitable multilayer to induce highly (00*l*) YBCO film, because of its smoother surface (lower rms value and higher percentage of atomically flat area (41%). Next, TFA-YBCO is deposited on both SBL700 and SBL850 to verify our assumption.

5.5 TFA-YBCO on STO/BZO/LAO

5.5.1 Structural and morphological characterization

TFA-YBCO films were deposited on $SrTiO_3$ cap layers for samples SBL700 and SBL850 using the optimized growth parameters described in section 3.1. The total thickness of the TFA-YBCO films on these multilayered systems was 300 nm.

The crystalline structure of the films was analysed by x-ray diffraction techniques; θ-2θ scan, ϕ-scan and ω-scan. From XRD θ-2θ scan, given in Fig. 5-17(a) it is shown that YBCO is nearly phase pure and c-axis aligned. Again, as for YBCO/STO/LAO films, very small amounts of BaF_2 were observed as shoulder from (100) LAO peak and weak peak at $2\theta \approx 41.1^{\circ}$. It indicates an incomplete precursor conversion [71]. Besides this intermediate phase, it has also been detected CuO phase as a result of YBCO conversion. [71,99]. It is worthy of remark that in this case, no interface reaction has been identified by XRD θ-2θ scan.

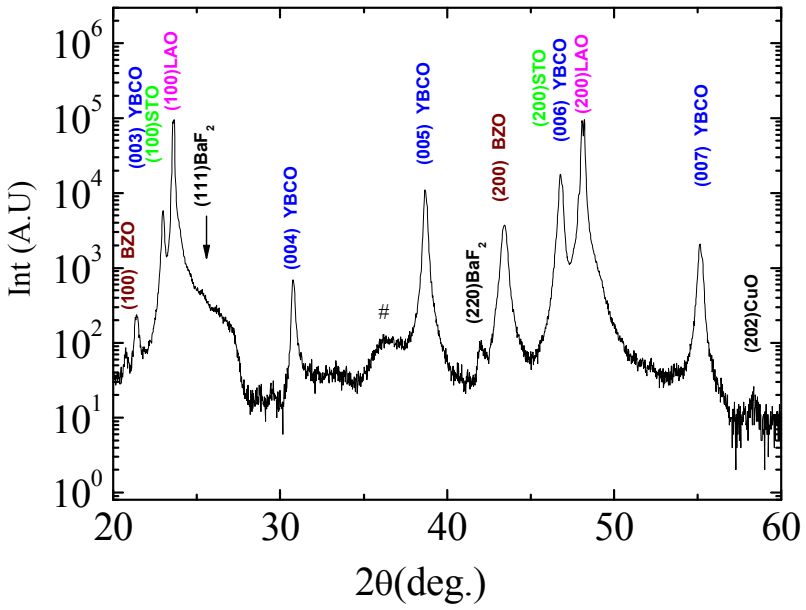

Fig. 5-17 θ-2θ XRD scan obtained for TFA-YBCO film grown on STO/BZO/LAO system at 795ºC with $P(O_2)$=0.02kPa and $P(H_2O)$=0.6kPa. Indicated by # is an instrumental artifact.

Fig. 5-18 shows detailed x-ray texture results obtained from ω- and ϕ–scan of YBCO for films grown on SBL700 and SBL850. They revealed a very good epitaxial texturing. The orientation relations determined are YBCO(00*l*)//STO(*h*00)//BZO(*h*00) and YBCO[001]//STO[001]//BZO[001]. We can observe from these results that the final YBCO in-plane texture maintains or even can improve that of the underlying cap layer.

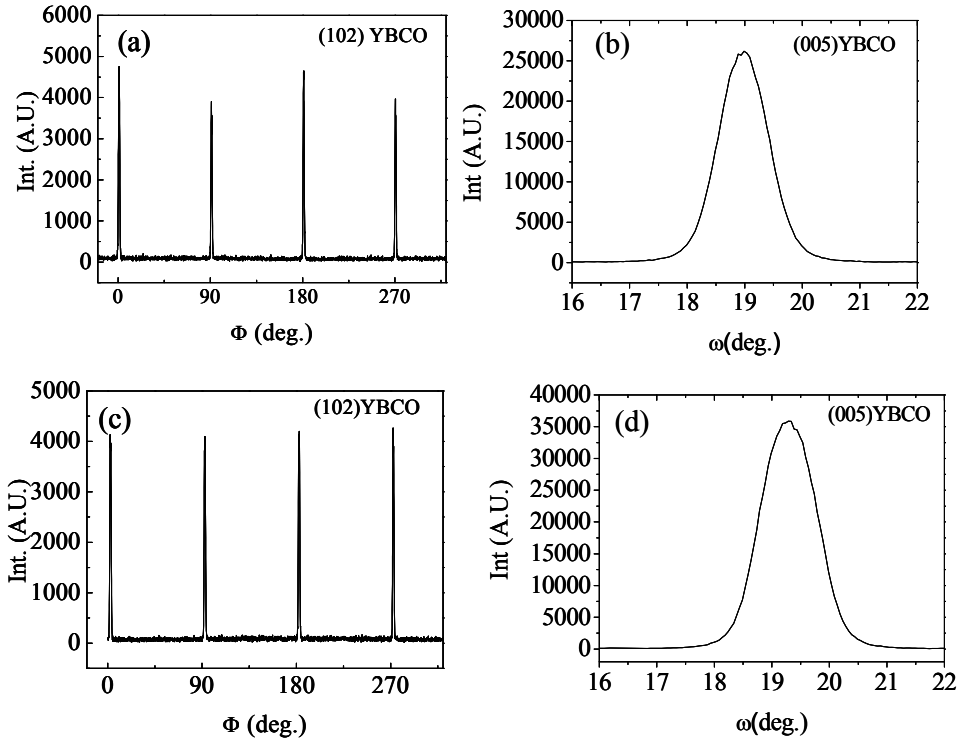

Fig. 5-18 X-ray diffraction texture analysis performed on YBCO film grown on (a) SBL700 $\Delta\phi$(102)YBCO= 1.4º (b) SBL700 $\Delta\omega$(005)YBCO=2.3º (c) on SBL850 $\Delta\phi$=2.1º and (d) SBL850 $\Delta\omega$(005)=1.2º

Moreover, it was found that in-plane and out-of-plane texture of YBCO grown on double buffer layer architecture, only increase up to 1.4º and 1.1º respectively in comparison with YBCO grown on a single buffer architecture.

We have investigated the surface morphology of these YBCO films by SEM. In Fig. 5-19(a) and (b). The more important feature of these images is that some a/b axis grains are observed, easily identified by their typical platelet-like shape. We should note that such pronounced increase in a/b-axis grain fraction is not resolved in typical θ-2θ x-ray diffraction patterns due to the overlapping with (006) YBCO and (200) LAO Bragg line reflections. In addition, for TFA-YBCO film grown on SBL850 we have eventually detected some YBCO grains at 45º.

Based on AFM surface analysis, here we suggest that the increased roughness of the STO buffer layer leads to an enhancement of a/b grains nucleation (as well as YBCO grown at 45º) and, as a consequence, to a higher density of residual pores associated with them in the YBCO films [156]. These results will be further discussed in the study of superconducting properties (see 5.2.2).

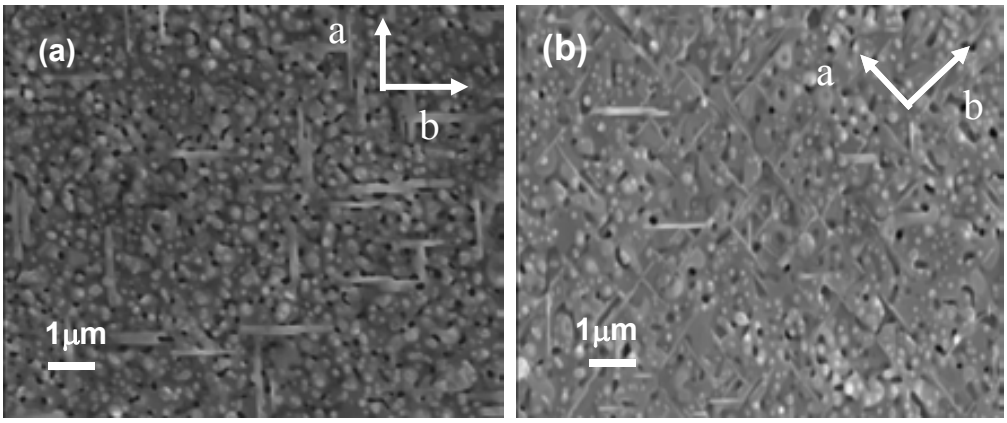

Fig. 5-19 SEM images of the surface of YBCO film grown on (a) SBL700 and (b) SBL850 at 795ºC,P(H_2O)= 0.6kPa, P(O_2)=0.02kPa, 180 minutes (150 min wet dwell+30 min dry dwell).

The high quality of the YBCO epitaxy is evidenced in the TEM images of Fig. 5-20. Here we can see a detail of the interface between a STO buffer layer grown at 700ºC and a TFA-YBCO thin film, Fig. 5-20 (a). The surface roughness of the STO layer leads to a non-planar interface with YBCO. Although in these samples we have not seen any indication of interfacial reaction, we have previously observed small traces of $BaTiO_3$ when TFA-YBCO was deposited on STO single crystal at T>830ºC (see Fig. 4-16) and on MOD-STO buffer layer (see Fig. 5-5). This indicates that chemical reactivity between STO and YBCO may occur. This fact should be taken in consideration when depositing YBCO/STO heterostructure onto metallic substrates with high surface roughness. As we mentioned earlier, fine tuning of YBCO reaction temperature and time could be needed to reduce the undesired formation of $BaTiO_3$. For the multibuffered architecture, we have observed that in some cases STO buffer layer did not completely cover the underlying BZO layer, and YBCO was found to grow directly onto BZO.

An example is given in Fig. 5-20 (b). Normally TFA-YBCO does not grow epitaxially on BZO due to the large lattice mismatch between both perovskites (Chapter 4) [91]. However, in Fig. 5-20 (b) we can see that there is no difference in the epitaxy quality of YBCO grown either on STO or on BZO. This suggest that YBCO (00*l*) nucleation takes place on the STO interface, and it is indeed this nucleation that governs the YBCO island growth mode. Thus, even if there are some YBCO grains directly nucleated on BZO, they become reoriented during the grain coalescence process.

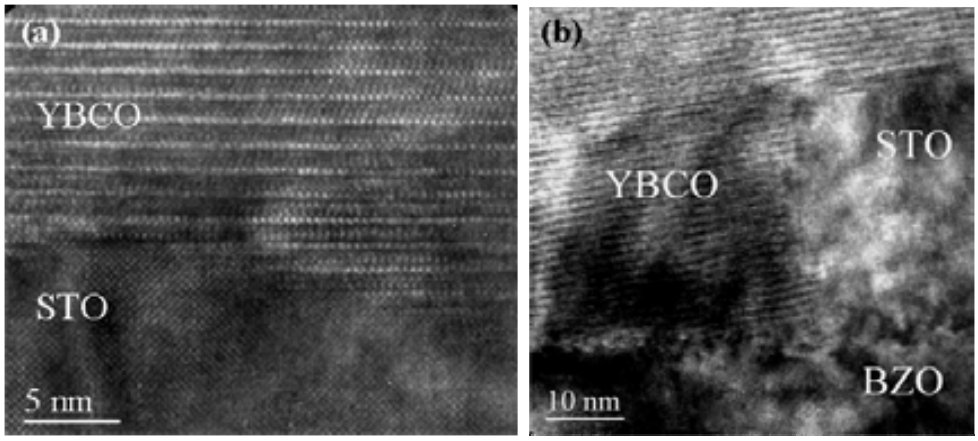

Fig. 5-20 Cross sectional high-magnification TEM images of TFA-YBCO on ^{MOD}STO/^{MOD}BZO buffered (100)-$LaAlO_3$ single crystal. (a) YBCO and STO interface. The good epitaxial growth of YBCO is evidenced even if the interface is not completely planar (b) detail of the TFA-YBCO thin film grown on top of the heterostructure STO/BZO. Epitaxial YBCO growth can be achieved even directly on BZO in the areas that were not coated by the STO layer.

5.5.2 Superconducting and electrical properties

Now we will turn our interest to the superconducting properties of the YBCO films. Fig. 5-21 shows the temperature dependence of the critical current density (a) and on the electrical resistivity (b) for YBCO films grown in the three architectures analysed in this chapter. In these series all the STO cap layers were grown at 700ºC. From the results of this figure several comments are in order. First, chemical solution deposition can lead to epitaxial thin films with high critical currents. However, in multilayered systems, J_c values and normal state resistivity are slightly degraded in comparison with YBCO/LAO single crystal substrate grown under the same conditions, being more pronounced in the case of double-buffered samples. Second, this evolution can be directly related to the as already mentioned porosity and a-b axis grains nucleation observed in SEM micrographs. Although nucleation and pore formation are still issues of debate in TFA-YBCO grown films [177,34,74], we believe that this enhancement of a/b grains and porosity is directly linked to the increased roughness observed in the final STO surface in STO/BZO/LAO and according to previous results found from STO buffer layers grown by PLD at different temperatures [162].

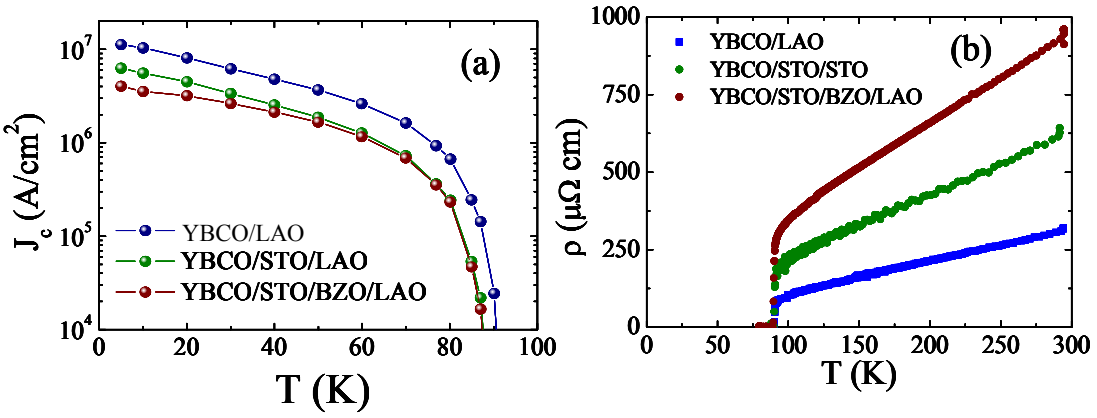

Fig. 5-21 Temperature dependence of the critical current density (a) and the electrical resistivity (b) for the three architectures here studied.

For a better understanding of this correlation we plotted the evolution of the STO average rms surface roughness with J_c, where all samples studied in this chapter have been included, independently of their architecture Fig. 5-22(a). Indeed, this figure shows the reduction of J_c at 5K with cap layer surface roughness, suggesting that an improving of the buffer layers quality should lead then to an improvement of superconducting properties and to recover this decrease of J_c [49].

c-axis grain fraction through micro Raman scattering measurements was quantified in the group (see 2.2.4) [178,121]. We can see in Fig. 5-22(b) that c-axis fraction exhibits a behavior similar to that of J_c and it significantly decreases from c-axis fraction ~0.9 for samples SS700 down to 0.82 for sample SBL700. For comparison, we have also plotted the typical c-axis fraction, 0.95, obtained from YBCO grown on STO single crystal. These results are consistent with SEM images in which it is observed an increase in a/b axis nucleation for multilayered structure.

Thus, we conclude that the increased roughness of the STO buffer layer leads to an enhancement of a/b grain nucleation in the YBCO layer and, as a consequence, to a higher density of residual pores in the YBCO films, both being limiting factors for high critical currents. However, considering the strong influence of the nature of the substrate on the TFA-YBCO film quality, as we previously observed in chapter 4, besides improvement the STO cap layer quality we also consider that optimization of YBCO growth parameters for each particular architecture: YBCO/STO/STO, YBCO/STO/LAO and YBCO/STO/BZO/LAO is required to improve texture quality and critical current densities of YBCO film.

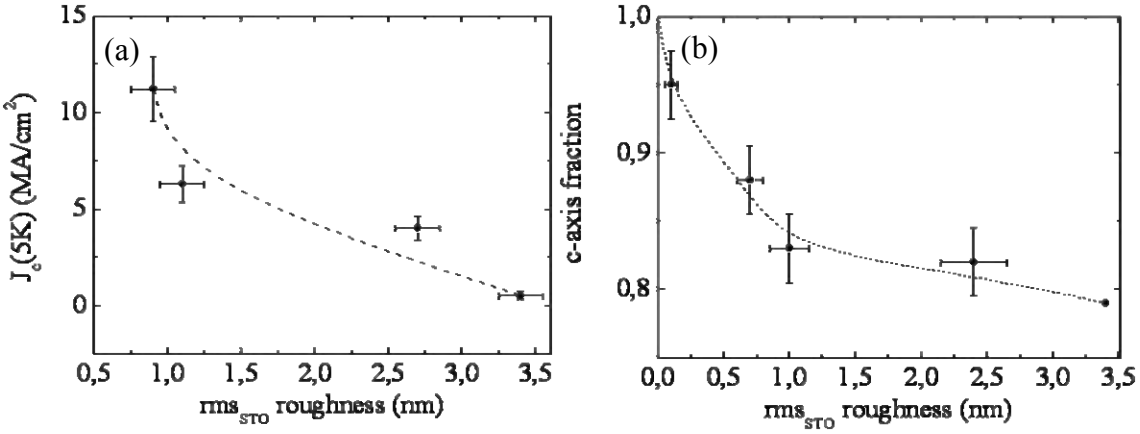

Fig. 5-22 Evolution of the fraction of c-axis-oriented grains as a function of the average rms roughness of the surface of the STO cap layer for the samples studied in this work. Dotted lines are guides for the eyes

Finally, we would like to remark that the all-sol gel coated conductor ^{TFA}YBCO/^{MOD}STO/^{MOD}BZO/NiO-SOE/Ni has been grown in our group and it has been shown that low roughness of the final cap layer of STO can be achieved with value of rms 3 nm. Also it has been proved that YBCO exhibits an excellent in-plane texture similar to that of the underlying buffer layer $\Delta\phi$(YBCO)~ 6.7º, $\Delta\phi$(NiO) ~6.6 [139]. Further work is now underway to optimize critical currents of these tapes.

5.6 Conclusions

In this chapter we have successfully demonstrated the compatibility of the use of chemical solution deposition techniques for buffer layer growth and for the superconducting YBCO layer, to generate reproducible heteroepitaxial perovskite films to be used as potential architectures in coated conductors technology. We have concentrated on the influence of the underlying buffer layer quality in the superconducting properties of TFA-YBCO thin films.

We have demonstrated by XRD and AFM investigations that high quality STO buffer layers films can be grown homoepitaxially in STO single crystals and heteroepitaxially in LAO single crystals in reducing atmosphere and 700ºC.

We have found by XRD analysis that TFA-YBCO film grows highly textured on STO single buffer deposited. SEM analysis reported a surface morphology dictated by pores, similar to YBCO film grown on STO single crystal, but here we have also found some a/b axis grains which leaded to high normal resistivity values. J_c values nearly 1 MA cm^{-2} have been obtained at 77K.

We have also produced double buffer layer architecture by chemical solution deposition, STO/BZO/LAO because this combination of two perovskite oxides is a promising alternative in SOE-NiO and IBAD-MgO and particularly for Ni substrate since we have work under reducing atmosphere.

We have optimized the growth temperature for BZO buffer layer. We have investigated 700ºC and 850ºC growth temperatures. Whereas XRD revealed a perfect epitaxial growth and no significant changes on texture quality, by AFM images we have observed that higher growth temperature leaded to rougher surface morphology. By TEM analysis it was observed an array of misfit dislocations at BZO/LAO interface to accommodate the high lattice mismatch. The quality of MOD-BZO buffer layer has been analyzed by depositing MOD-STO cap layer on top. By means of XRD and AFM we have investigated the quality of STO cap layer. Even though $\Delta\omega$ and $\Delta\phi$ values of STO have slightly increased in comparison to BZO values, excellent grain alignment is obtained. Rough surface morphology of BZO layer is transferred to STO cap layer. We have detetcted an increase of rms roughness from 0.9 nm in the case of STO single-buffer to 3.4 nm for double buffer architecture. However, by TEM analysis we have not observed interface reactivity.

We have analyzed surface morphology through two statistical parameters: rms and percentage of atomically flat area parameters. Due to in all cases the buffer surface consisted in rounded grain structure with considerable amount of voided boundaries, both parameters provided us similar information and therefore, for this system, they can be utilized in the same way.

We have successfully grown TFA-YBCO film grown on STO/BZO/LAO system. Biaxially textured YBCO film has been obtained but we have distinguished by SEM and quantified by μ–raman measurements an increase of the formation of sparsely distributed a-axis grains attributed to the increase of buffer layer rms roughness. The increase of a-axis grains in the YBCO film correlated by an increase of porosity which in turn degraded superconducting properties, evidenced by continuous decrease of J_c and increase of normal state resistivity. Actually the investigation of J_c dependence on STO rms roughness has given some hints about the origin of the film degradation confirming the influence of the underlying film on TFA-YBCO film quality.

In addition, comparing TFA-YBCO film quality grown on MOD-STO cap layer and even TFA-YBCO film grown on STO single crystal substrate with TFA-YBCO film grown on LAO single crystal substrate, we detected that we did not achieved optimal superconducting properties on STO layer. Indeed, recent investigation on the influence of growth parameters on YBCO film quality deposited on STO single crystal substrate revealed that the nucleation of a/b axis grains as well as the detection of intermediate phases can be overcame by using higher growth temperatures. Therefore, this knowledge should be also applicable for TFA-YBCO film

growth on MOD-perovskite buffer layers allowing improving film microstructure and superconducting properties and then being further transferred an optimized on metallic substrate. Since interface energy, lattice match and chemical compatibility changes between YBCO and the underlying layer, it is clear that YBCO growth conditions should be adapted in each case.

In conclusion, our work has shown that TFA-YBCO films have been successfully grown on perovskite buffer layers prepared under reducing atmospheres by chemical solution deposition reaching J_c values around 1MA cm^{-2} at 77K. We suggest, therefore that perovskite MOD-STO buffer layer have to be considered as a promising alternative as a cap layer for all chemical coated conductors.

B. Fluorite Structure

CHAPTER 6

Microstructure and surface conditioning of CeO_2 films deposited by vacuum techniques

6.1 Motivation

CeO_2 fluorite structure is considered a very promising cap layer for coated conductors since it has good lattice matching with $YBa_2Cu_3O_7$ (YBCO). The results achieved with vacuum technologies have proved the potential of coated conductor (CC) technology. J_c values of several MA/cm^2 at 77K are routinely achieved for YBCO films grown by pulsed laser deposition (PLD) onto IBAD-YSZ [36] and on biaxially textured Ni and Ni-W [179]. The major goal now for CC technology to be competitive is to demonstrate the suitability of low cost deposition techniques, similarly to the heteroepitaxial perovskite cap layer films (chapter 5).

During the last years, many efforts have been focused on fabricating CeO_2 buffer layers by metalorganic decomposition (MOD). However, a number of specific issues have emerged. They are mainly three ones: (1) to synthesize a stable and wetting precursor solution, because it tends to form a gel rather soon [139], (2) to grow fully epitaxial CeO_2 films with (001)-terraced surface in reducing atmosphere, for avoiding the oxidation of the bare metal substrate, and

finally, (3) to control the reactivity between YBCO and CeO_2 to form $BaCeO_3$, because still now there are some discussion about when $BaCeO_3$ forms and whether it is a critical parameter to J_c properties of the YBCO phase [180,181].

These important topics forced us to do a previous study on a model system: CeO_2 deposited by sputtering on YSZ single crystal substrate. The reason for this choice is basically that this vacuum deposited CeO_2 buffer layer has been successfully used in the literature as the first approach to medium cost coated conductors [182].

The quality of a buffer layer, in particular its surface is known to substantially affect the properties of the subsequent layer. In fact, we have seen in perovskite cap layers (Chapter 5) that the quality of TFA-YBCO growth depends not only on a good microstructure but also on the film surface roughness. In this chapter it has been optimized vacuum deposited CeO_2 cap layer exploring its influence on TFA-YBCO growth. To do that we modified CeO_2 surface by processing CeO_2/YSZ substrate at high temperature under different atmospheres and a detailed characterization for each sample (structural, morphological, compositional) has been carried out. These results were discussed in relation to the superconducting properties, microstructure and texture of TFA-YBCO films grown on top of this cap layer. The optimal conditions obtained by the model system, CeO_2/YSZ single crystal substrate, were then applied to multilayered metallic substrates: CeO_2/YSZ/CeO_2/Ni and CeO_2/YSZ/SS. This knowledge would be transferred to MOD-CeO_2 system in the next chapter.

6.2 CeO_2 properties

Ceria (CeO_2) is an important component in many technological devices due to its remarkable properties [183]; most of their technological applications (catalysis [184], electrochemistry [185,186], optics [187,188]) as in CeO_2 coatings for YBCO –CC, closely involve the surface of cerium oxide. Thus, there is a clear need to generate a full understanding of the influence of the surface chemistry and morphology of CeO_2 on the properties of the final superconducting film.

Vacuum CeO_2 buffer layers have been widely used in the fabrication of coated conductors because of its lattice match with the YBCO superconducting layer (ε=0.52%), it does not diffuse into the superconductor and it is a zirconia diffusion barrier [15,36].

We have observed in preliminary studies that MOD-CeO_2 cap layers needs to be (001) surface-oriented for subsequent TFA-YBCO epitaxial growth [38,189]. Several force-field calculations of surface energies and surface relaxations of CeO_2, predict the (111) surface to be the most stable followed by the (110) one. The same studies show that unfortunately the (001) surface is considered less stable due to the polar nature of the fluorite crystal structure with alternating planes of oxygen and cerium ions [190,191]. It is therefore an important issue of

this chapter to determine if this mechanism also controls the TFA-YBCO film on CeO_2 films deposited by vacuum techniques.

Additionally to a good cap layer for YBCO CC, CeO_2 is also a good oxygen conductor. This means that, under oxidizing YBCO growth conditions, if one wants to avoid a multibuffer architecture, it is necessary a high thickness of CeO_2 to protect the metallic substrate from oxidation. But this leads us to the other main problem of CeO_2: High thickness of CeO_2 easily deteriorates microstructure because microcracks form due to thermal stress [150,192,148]. The influence of these microcracks on the superconducting properties of TFA-YBCO films and their evolution with different thermal treatments is also studied in this chapter.

Another interesting aspect of CeO_2 which will be addressed in this chapter and stressed in the following one, is the special chemistry of Ce^{4+}, which can readily reduce itself to Ce^{3+} creating an oxygen vacancy, $V_o^{\cdot\cdot}$, by charge compensation.

In the Kröger-Vink-notation [193], the process of ceria reduction may be written as

$$O_O + 2Ce_{Ce} \rightarrow \frac{1}{2}O_2 + V_{\ddot{o}} + 2Ce'_{Ce} \qquad \text{Eq. 6-1}$$

where O_o describes an oxygen atom that occupies an oxygen site in the lattice and Ce_{Ce} represents a Ce^{4+} ion that occupies its corresponding atom site in the lattice. $V_O^{\cdot\cdot}$ is an oxygen vacant site and the superscript ($^{\cdot\cdot}$) shows that it has a double positive charge relative to the perfect lattice, as there is the absence of an O^{2-} ion. Finally, Ce'_{Ce} represents a reduced cerium ion (Ce^{3+}), which occupies a cerium site in the lattice.

6.3 Sputtering-CeO_2/YSZ single crystal substrates

6.3.1 Preparation of sputtering CeO_2 buffer layers

Rectangular wafers of (100)-oriented CeO_2 on YSZ (100) single crystal substrate were supplied by Cryoelectra [182] and diced into smaller square pieces (5 x 5 mm) using diamond-saw. The CeO_2 layers were grown by rf sputtering at 780ºC under Ar/O_2 (20% O_2 in Ar) atmosphere up to a thickness of 75 nm. Unfortunately, not many details are known about the preparation of this particular sputtering-CeO_2 buffer layer.

Full width at half maximum (FWHM) values for in-plane and out-of-plane texture were $\Delta\phi$ (111) = 2.1º and $\Delta\omega$ (200)= 1.2º.

CeO_2/YSZ samples were cleaned using an ultrasonic bath in two successive solutions of acetone and methanol. The cleaned buffered-substrates were then heated up to 900ºC at a lineal

rate of 200ºC h^{-1} and then held isothermally for 4 hours in two reducing conditions 95%Ar/5%H_2 (Ar/H_2) or 95%Ar/5%H_2 saturated with P(H_2O)=2.2 kPa (Ar/H_2/H_2O). The films were afterwards slowly cooled down to room temperature under the same gases.

Since in preliminary investigations on MOD-CeO_2 films we observed that best properties were obtained in O_2 atmosphere [38], post-annealing in O_2 was performed in CeO_2/YSZ substrate to compare morphology and surface chemistry evolution. Nevertheless, this treatment may not be feasible with practical CC metallic substrates (in particular Ni) taking into account the need to avoid substrate oxidation.

6.3.2 Structural and morphological characterization

6.3.2.1 X-Ray Diffraction analysis (XRD)

The grain alignment, morphology and chemical composition of the CeO_2 /YSZ samples were investigated after different processing conditions.

In Fig. 6-1 XRD θ-2θ scan of as-grown CeO_2/YSZ substrate has been compared with Ar/H_2/H_2O processed CeO_2/YSZ substrate. Only (*h*00) CeO_2 and YSZ reflections can be observed revealing CeO_2 single phase for both films (notice that XRD θ-2θ diagrams are vertically shifted). XRD θ-2θ scans for Ar/H_2 and O_2 processed CeO_2/YSZ substrates have not been compared in Fig. 6-1 because display similar profile as Ar/H_2/H_2O processed substrate. It is interesting to mention that the (*h*00) CeO_2 reflection for Ar/H_2/H_2O and O_2 processed samples are around 50% stronger than for the original sample.

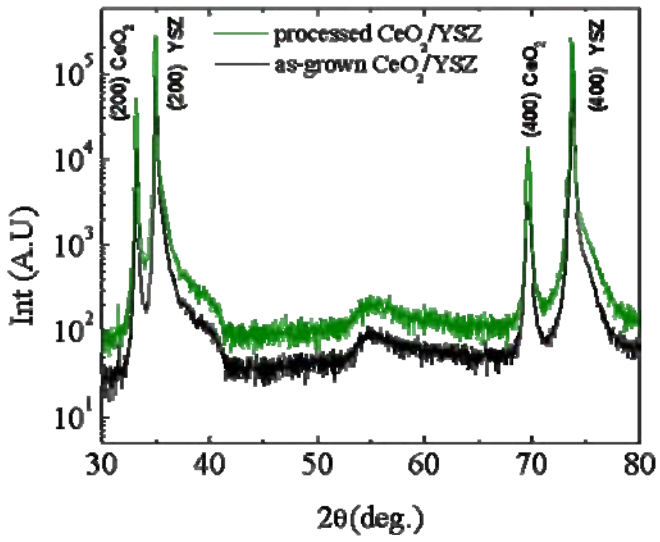

Fig. 6-1 XRD θ-2θ diagram of CeO_2/YSZ substrates of as-grown sample (in black) and processed in Ar/H_2/H_2O sample (in green)

On the other hand we have calculated FWHM of ω- and ϕ-scan for (200) and (111) CeO_2 reflection respectively for as-grown and processed samples (listed in Table 6-I). The FWHM values of ω-scans decrease from 1.2º in the as-grown sample to ~0.8º in the processed ones, while FWHM values of ϕ-scans have been reduced from 2.1º in as-grown CeO_2 film down to ~1.2º in the post-annealed ones. These results agree well with the observed increase in 2θ Bragg line intensity of (*h*00) CeO_2 reflections. Finally, ϕ-scans of the (111) reflection show four peaks 90º apart, signaling a unique in-plane orientation (Fig. 6-2). It was verified that the peak positions coincide with those corresponding to the (111) substrate reflection, indicating that CeO_2 grows on (100)-YSZ with a cube-on-cube type epitaxial relationship. In summary, from the XRD analysis we have found that the degree of crystallinity and grain alignment of the CeO_2 layer was slightly improved with any of the annealing treatments performed.

Table 6-I Summary of the XRD- texture measurements (Δω and Δϕ) of CeO_2/YSZ substrate processed at different atmospheres: Ar/H_2, $Ar/H_2/H_2O$ and O_2.

CeO_2/YSZ		
Processing atmosphere	Δω(200) CeO_2 (º) (±0.1)	Δϕ(111) CeO_2 (º) ±(0.1)
As-grown	1.2	2.1
Ar/H_2	0.8	1.7
$Ar/H_2/H_2O$	0.8	1.2
O_2	0.8	1.2

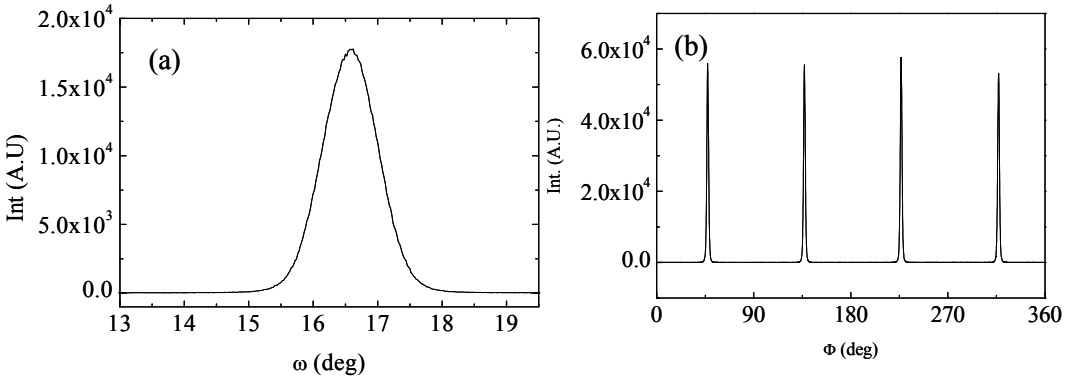

Fig. 6-2 XRD texture analysis of CeO_2/YSZ substrate processed in $Ar/H_2/H_2O$ atmosphere (a) omega-scan (200) CeO_2 with FWHM= 0.8º (b) Phi scan of (111) reflection of CeO_2, Δϕ=1.2º.

6.3.2.2 Atomic Force Microscopy

Surface topography of as-grown and processed CeO_2/YSZ substrates was studied through atomic force microscopy (AFM).

As reveled by AFM images, the surface of the as-grown CeO_2/YSZ sample, shown in Fig. 6-3 (a), presents microcracks and small globular grains, with rms roughness of 1.8 ± 0.2 nm. They can be appreciated in the inset of Fig. 6-3 (a). Instead, the film annealed under reducing atmosphere (Ar/H_2), Fig. 6-3 (d), showed a heterogeneous, hill-like surface. This film displays an average roughness of ≈ 3.7±0.4 nm. The surface of the sample annealed in O_2, Fig. 6-3 (b) and the sample annealed in $Ar/H_2/H_2O$ atmosphere, Fig. 6-3 (c), evoluted to larger and qualitatively flatter grains, preserving the cracked feature with an average rms roughness of ~0.9 and ~1.6 nm respectively. This result is better understood if we carefully inspect the representative line profile selected for each image. It is depicted at the bottom of the corresponding topographic image, Fig. 6-3 (a-d).

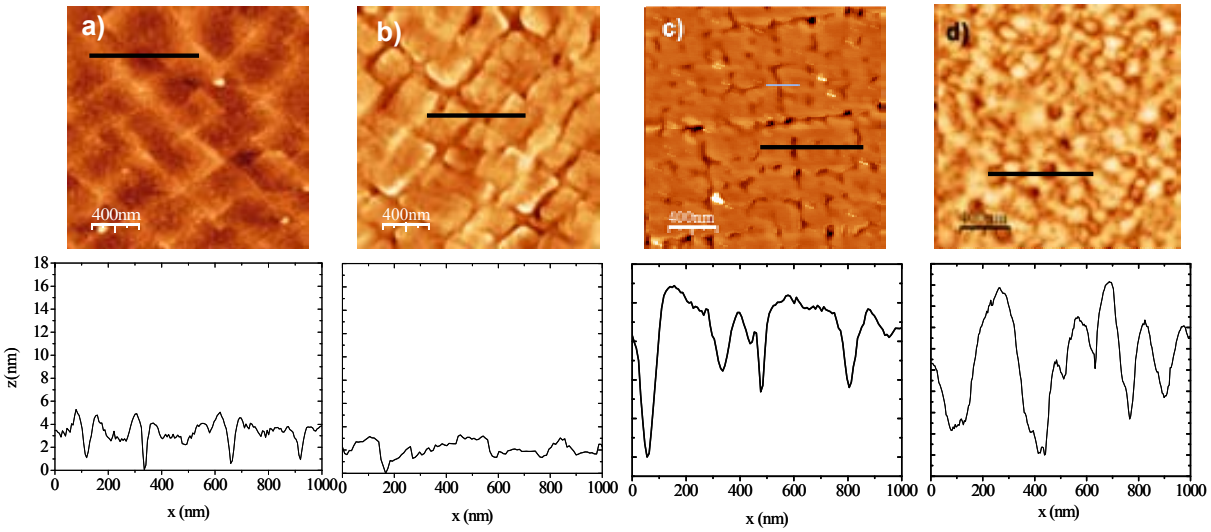

Fig. 6-3 AFM images and height profile of CeO_2/YSZ samples : (a) as-grown film with a rms 1,8nm ±0.2, (b) processed under O_2 rms ≈ 0.9 nm ± 0.1, (c) annealed under $Ar/H_2/H_2O$, rms ≈ 1,6 nm±0.3,and (d) annealed under Ar/H_2, rms ≈ 3,7 nm±0.4.

From these profile scans it is easily seen that annealing in O_2 and $Ar/H_2/H_2O$ atmosphere lead to atomically flat terraced-like surface morphology, (001)-faceted, whereas Ar/H_2 -reducing treatment gave rough surface. We have also carried out treatments under Ar/H_2 atmosphere with small quantities of O_2, to simulate the water content in $Ar/H_2/H_2O$ atmosphere, but the results are similar to that one of the pure reducing atmosphere. Therefore, it is clear that in this case H_2O has a special role in minimizing (001) surface energy as will be discussed forth.

We have performed a quantitative estimation of the atomically flat area that display each of these CeO_2 films before and after being processed. We followed similar procedure as the one described for perovskite buffer layers in chapter 5 and being further explained in section 2.1.1. However, in this case, the threshold value has been modified being three unit cells of CeO_2 (~1.5 nm).

Fig. 6-4 illustrates the resulting binary images where blue area identifies flat grains. From the statistics performed on binary images we obtained that as-grown CeO_2/YSZ substrate contains 46% of atomically flat area, Fig. 6-4(a). By contrast, CeO_2/YSZ substrate processed in O_2 and $Ar/H_2/H_2O$ exhibit 87% and 84% of atomically flat area, as can be seen from Fig. 6-4(b) and (c) respectively. Finally, in CeO_2/YSZ substrate processed in Ar/H_2 only 18% of surface is atomically flat, Fig. 6-4(d).

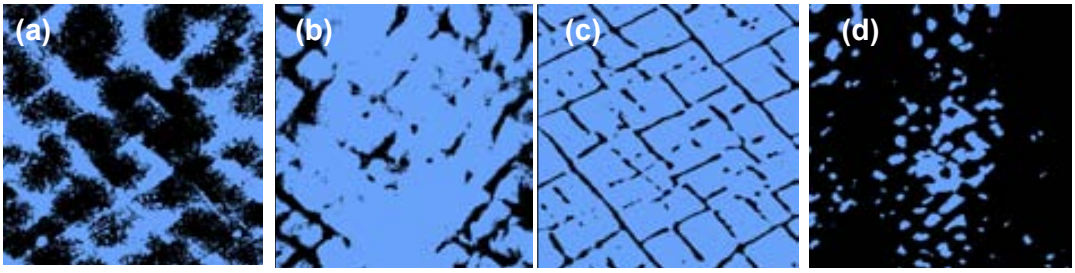

Fig. 6-4 Binary images resulting from the application of a Binary Operator on AFM topographic image of CeO_2/YSZ substrate (a) analysis performed on as-grown (b) on processed in O_2 (c) on processed in $Ar/H_2/H_2O$ (d) on processed in Ar/H_2 .

In contrast to the previously investigated perovskite cap layer system (chapter 5), in CeO_2 films rms roughness and percentage of atomically flat area parameters do not correlate, i.e, two films with similar rms values display strongly different percentages of atomically flat area (compare as-grown with 46% of atomically flat area and $Ar/H_2/H_2O$ processed CeO_2/YSZ substrate with 84% of atomically flat area, both with rms ~ 1.7 nm). By investigating in detail the surface topography of CeO_2 from Fig. 6-3 we have observed that the main difference arises from the development of (001)- atomically flat hillocks in some processed CeO_2 films. In fact, rms roughness parameter masks the atomically flat area contribution in terraced surfaces because it also computes the deep cracks contribution and results in a non meaningful average value. By contrast, percentage of atomically flat area parameter rules out this contribution and gives the effective flat area contribution. In section 6.4, by investigating the quality of TFA-YBCO film on these referred cap layers, it will be elucidated which of these two parameters have to be used to evaluate the atomically flat area in CeO_2 cap layers.

At present, there seems to exist no unified opinion among experimentalists concerning the mechanism to stabilize the (001) surface in CeO_2. There are several ways for nature to minimize the energy such as surface relaxation (elimination of one half monolayer of oxygen in the top

layer), surface reconstruction and adsportion of adatoms on the surface. Based on work reported by Jacobsen and coworkers [189] who stated that O_2 atmosphere stabilizes (001)- planes through a some kind of surface reconstruction of an unknown origin. We proposed that higher annealing temperature in oxygen, can change the relative surface energies, and possibly increase the mobility of the cation lattice resulting in change the free surface energy of cerium dioxide stabilizing the (001) planes [190]. Nevertheless, based on the experimental results observed above, it is likely that the O_2 scenario is not valid for the $Ar/H_2/H_2O$ atmosphere. It seems that here hydroxyls (not O_2) are the active component for stabilizing the (001) terraced surface. In this case, it was suggested that the exchange of oxygen (from ceria surface) with hydroxyls (from H_2O), would be the most feasible mechanism to reduce the surface charge per atom being consistent with the theoretical calculations, see Fig. 6-5, [194,195].

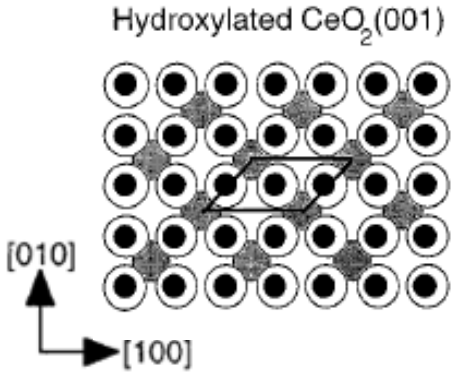

Fig. 6-5 Structural model for the nonpolar reconstruction of the $CeO_2(001)$ surface. The cerium, oxygen, and hydrogen ions are represented by gray, white and black circles, respectively [195].

Note that the study of the influence of processing atmosphere on CeO_2 surface morphology allows us to make a distinction between atmospheres that enhance the formation of atomically flat areas ($Ar/H_2/H_2O$ and O_2) and atmospheres that do not (Ar/H_2). By contrast, from XRD analysis we only observed a slight difference between processed and non-processed substrate. Therefore, to finish off the texture and morphology study on CeO_2 surface, we carried out, in collaboration with IFW-Dresden, RHEED measurements from as-grown (surface with rounded grains) and $Ar/H_2/H_2O$ processed CeO_2/YSZ substrate (flat terraced surface).

6.3.2.3 Reflection High Energy Electron Diffraction

We have investigated if the morphological evolution observed by AFM analysis is associated to changes in surface texture. Thus, we examined by RHEED the surface of the film after growth, Fig. 6-6(a), and the surface of the film processed in $Ar/H_2/H_2O$ atmosphere, Fig. 6-6(b).

The primary beam alignments along <100> and <110> directions of the substrate are shown. In both cases a diffraction pattern with spots are obtained, characteristic of a surface with high degree of oriented grains [38]. In the as-grown CeO_2 film the diffraction pattern displays an array of rounded spots, Fig. 6-6(a), whereas the pattern becomes streakier when CeO_2 is processed under wet atmosphere, Fig. 6-6(b). Spotty pattern is characteristic of a 3D surface, in agreement with the rounded grains proved by the cross section line in AFM analysis, Fig. 6-3(a). On the other hand, in CeO_2 processed in $Ar/H_2/H_2O$ atmosphere, the transition from rougher (3D) to smoother surface morphology (2D) dominates the RHEED, resulting in a streakier pattern. This result correlates well with terraced surface morphology detected from AFM analysis performed above.

In summary, from the above results we observed that both original and processed under $Ar/H_2/H_2O$ CeO_2/YSZ single crystal substrates display textured surface and we have observed an evolution from three dimensional to bidimensional surface. As we anticipated in section 6.4 we will explore if these two scenarios will influence differently TFA-YBCO film quality.

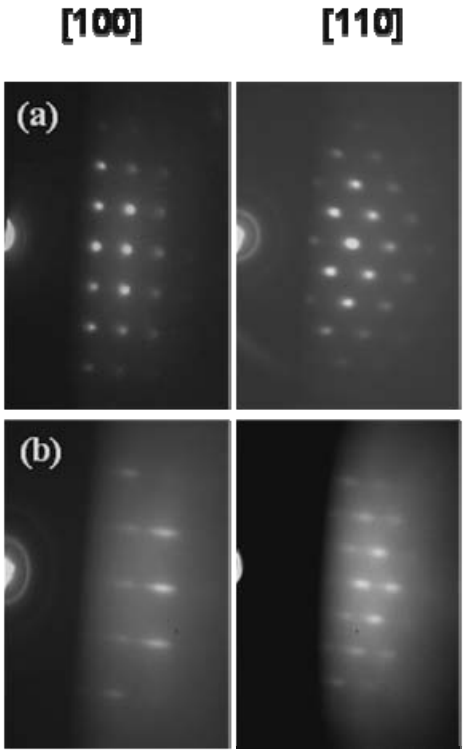

Fig. 6-6 RHEED patterns obtained from a CeO_2 cap layer on YSZ single crystal along the <100> and <110> directions of the substrate for as-grown (a) and processed in $Ar/H_2/H_2O$ atmosphere (b).

6.3.3 Surface chemistry characterization

Further investigation on these ceria-based substrates is carried out by X-ray Photoelectron Spectroscopy (XPS) in attempt to figure out the relationship between processing atmosphere and these geometric surface reconstructions through possible changes in chemical composition such as larger degree of hydroxylation or Ce^{3+} content. Therefore, we performed a systematic analysis on the different samples: as-grown, processed in Ar/H_2, $Ar/H_2/H_2O$ and O_2 atmosphere.

Survey spectra were firstly recorded in the range of binding energy of 1200-0 eV with unmonochromatized Mg K_α X-rays, to identify the elements present in each sample. Then the photoelectron peaks of O(1s), C(1s) and Ce(3d) were recorded with higher resolution. Conditions and details of spectra acquisition are described in section 2.1.3.1.

Due to the insulating nature of this material, surface charging occurred during the photoemission process, and calibration of the binding energy scale had to be made in all cases using $Ce(3d)_{5/2}$ spectra, the peak singed u''' (see section 2.1.3.1).

Due to the complexity of the Ce(3d) spectra, it is difficult to determine by simple inspection the percentage of Ce^{3+} involved in each annealing conditions. For our aim, we used a quantitative approach in which all necessary basic data are integrated peak areas. However, in order to compare, add and subtract areas from different samples we have to normalize the intensity of all the spectra of these series of samples from reference spectra (for detailed explanation of quantification procedure see section 2.1.3.1.3). The results of this normalization are depicted in Fig. 6-7, Fig. 6-11 and Fig. 6-10 for these three photoemission signals.

It is clear, by comparison of Ce(3d) spectra in Fig. 6-7 with the spectrum for pure CeO_2 (see Fig. 6-8(a)), that Ce^{+4} is the main oxidation state at the surface of all the four samples of the series. Moreover, as expected, the shape of the Ce3d spectrum for the sample annealed under O_2 (Fig. 6-7 (d)) is just the one due to pure Ce^{+4}, in CeO_2. Only for the original sample, Fig. 6-7 (a), the presence of the peaks u' and v', clearly indicates the existence of a certain (minor) amount of Ce^{+3}.

The Ce3d spectra for the two resting situation (after annealing under Ar/H_2 and $Ar/H_2/H_2O$ atmospheres) are nearly identical, and very close to the one for pure CeO_2, indicating the existence of only traces of Ce^{+3}.

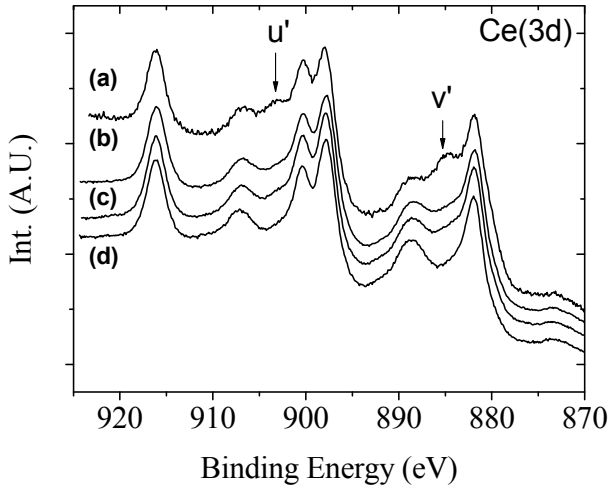

Fig. 6-7 Ce(3d) spectra from the CeO_2/YSZ samples: as-grown film (a), and after annealing in $Ar/H_2/H_2O$ (b), in Ar/H_2 (c) and under O_2 (d). Indicated with arrows the typical features developed when Ce^{3+} is present (u' and v' peaks).

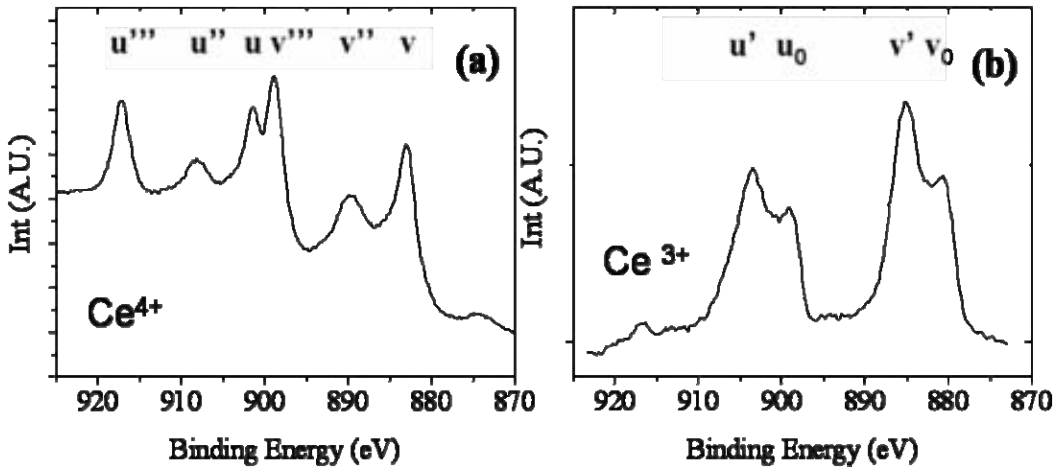

Fig. 6-8 (a) Ce3d spectrum of well-oxidized ceria close to CeO_2 (b) Ce3d spectrum of reduced ceria, close to Ce_2O_3

Quantification of the Ce^{+3} content can be now easily done by subtracting the spectrum for sample annealed under O_2 to the other three situations. From this computation it results an spectrum with only Ce^{3+} contribution, shown in Fig. 6-9. By comparing these spectra with pure Ce^{3+} spectrum (see Fig. 6-8 (b)) we observe that they reproduce quite well the typical features of Ce^{+3} species. Their intensity (areas), in comparison with the intensity of reference spectra, determines the Ce^{+3}/Ce ratio in each sample.

Thus, samples annealed under $Ar/H_2/H_2O$ and Ar/H_2 present 5% and 7% of Ce^{+3} species. Despite it is well known that Ar/H_2 atmosphere enhance ceria reduction [106], Ce^{3+} is air sensitive and ceria surface has been likely oxidized during its exposition to air, after annealing treatment. Finally, the as-grown film contains ~18 % of Ce^{3+}. This result is in disagreement with the expected fully oxidized surface. Regarding this apparent inconsistency, detailed analysis of C(1s) and O(1s) regions is required.

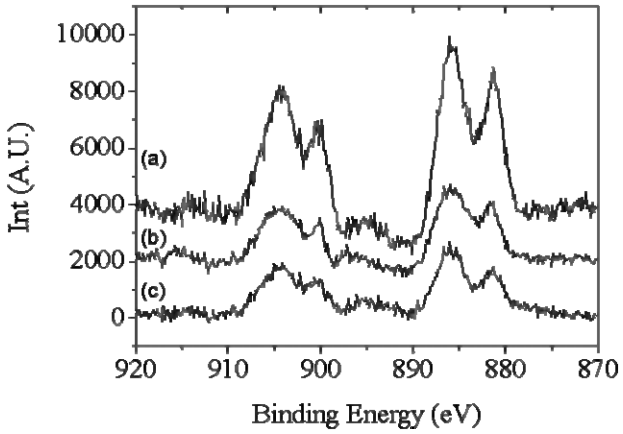

Fig. 6-9 Resulting spectra of the Ce^{3+} contribution from CeO_2/YSZ samples: As-grown (a), processed in Ar/H_2 (b) and processed in $Ar/H_2/H_2O$ (c).

Data for O(1s) region for as-grown ceria consists of two peaks, Fig. 6-10 trace (a). The main peak located at about 529.7 eV is related to the oxygen in the CeO_2 [196]. The high binding energy component, at 532.1 eV, can be ascribed both to OH^- and CO_3^{2-} species. In this respect, it is a very well known that rare earth oxides form hydroxides by water adsorption [197]. However, for this sample, the high intensity of this component, $O_{532.1}$, may be also attributed to oxygen due to carbonates.

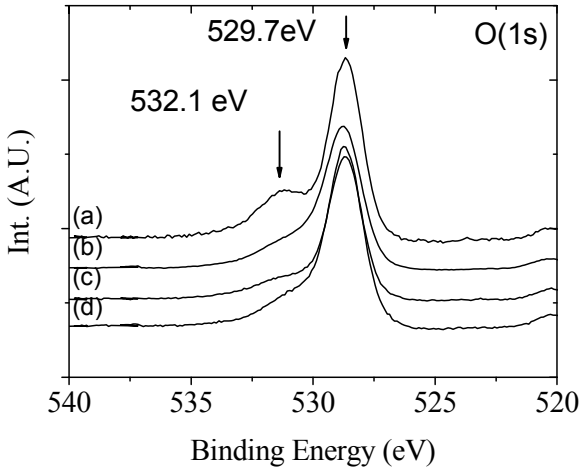

Fig. 6-10 O(1s) spectra from the CeO_2/YSZ samples: as-grown film (a), and after annealing in $Ar/H_2/H_2O$ (b), in Ar/H_2 (c) and under O_2 (d).

Actually, the presence of a peak at ~ 289.5 eV (BE) in the C1s spectrum demonstrates the existence of an important amount of CO_3^{2-} species at the surface of this sample. Finally, the main peak in the C(1s) region, at ~ 285.3 eV, is assigned to 'carbon', (graphite and hydrocarbon-like species), a common contaminant of oxide surfaces.

Regarding the annealed samples, the O1s spectra display asymmetric peaks; the main signals, at 529.7 eV, due to oxide species (O^{2-}) of the CeO_2 lattice, present only weak shoulders at the high binding energy side, while their C1s spectra show only traces of CO_3^{2-}. Consequently, the minor component in the O1s spectra must be assigned to hydroxyl groups. Finally, it must be noted that the intensity of the C1s signal due to surface contamination, at 285.3 eV, has strongly decreased in comparison with the as-grown sample.

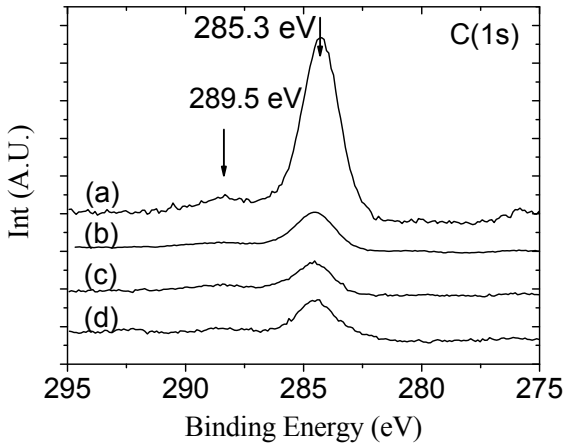

Fig. 6-11 C(1s) spectra from the CeO_2/YSZ samples: as-grown film (a), and after annealing in $Ar/H_2/H_2O$ (b), in Ar/H_2 (c) and under O_2 (d).

In summary, XPS analysis proves the existence of significant amounts of Ce^{3+} and CO_3^{2-} species, in the as-deposited CeO_2 films, very likely, as a consequence of the characteristics of the deposition method (Ar content atmosphere) [182]. Since these Ce^{+3} species have not been oxidized to Ce^{+4} during the exposition of the samples to the atmosphere, it must be concluded that they are not located at the surface or, alternatively, that CO_3^{2-} groups proved stabilization of Ce^{+3}. Regarding the annealed samples, the surface analysis by XPS have shown that the three treatments remove CO_3^{2-} species and most of contaminants, and it provides a fully hydroxilated-oxidized surface, with only residual traces of Ce^{3+}.

This surface chemical composition has been attributed to exposure the sample to air after processing treatment. At the same time it impeded to detect if existed any distinctive feature for the ceria processed in $Ar/H_2/H_2O$, in O(1s) spectra or in Ce(3d) spectra, which would assess its special role in stabilization of the required (001) ceria surface [195].

To conclude, it was demonstrated that CeO_2 surface can be tuned by post deposition processing. XRD data showed improved in-plane and out-of-plane texture for all processed films. AFM and RHEED measurements confirm the feasibility of $Ar/H_2/H_2O$ processing atmosphere to enhance flat terraced ceria surface (>80%), and thus, it is a route to be further explored when growing on metallic tapes, as will be discussed below. Cracks are observed in the as-grown sample and rougher surface for Ar/H_2 atmosphere. By XPS measurements we estimated the percentage of Ce^{3+} on different ceria surface and unexpectedly we found that as-grown ceria surface was partially reduced with some carbonate groups adsorbed on it. Annealing treatments enhances desorption of that carbonate groups and the conversion of Ce^{3+} to Ce^{4+} sites. No singular chemical composition was appreciated for $Ar/H_2/H_2O$ processed sample to be correlated with its surface planarity (001)-faceted.

Once all these substrates have been fully characterized we should remark that all these processing conditions have been made for a unique scope: develop optimal ceria surface to enhance epitaxial growth of YBCO film on top. Therefore, we turn to study the accommodation of the superconducting oxide on the different substrates.

6.4 Preparation of TFA-YBCO films on processed sputtering-CeO_2/YSZ model system

6.4.1 Microstructural and morphological characterization

TFA-YBCO, with a total thickness of ~275 nm, was grown on the different annealed CeO_2/YSZ substrates studied above. The conditions followed in the TFA-YBCO -coating process on $LaAlO_3$ single crystal [34] were applied to the fabrication of TFA-YBCO on CeO_2

cap layer. Thus, all of the samples were subjected to a pyrolysis (see 3.1.3) and high temperature heat treatment (3.1.4). To limit the undesired reactivity between YBCO and CeO_2 previously reported [139], samples were grown at 780ºC for 180 minutes and partial pressures of 0.6 kPa for water and 0.02 kPa for oxygen, see Fig. 6-12.

The grain alignment, microstructure and surface morphology of the TFA-YBCO on sputtering-CeO_2/YSZ model system were investigated for as-grown and annealed substrates. Although oxygen processed CeO_2/YSZ substrate has been useful as a reference specimen in the study of surface evolution, in the study of YBCO film, we focused on as-grown, Ar/H_2 and $Ar/H_2/H_2O$ processed CeO_2/YSZ sample, because O_2 processing conditions could not be transferred to Ni metallic substrate for further CC fabrication.

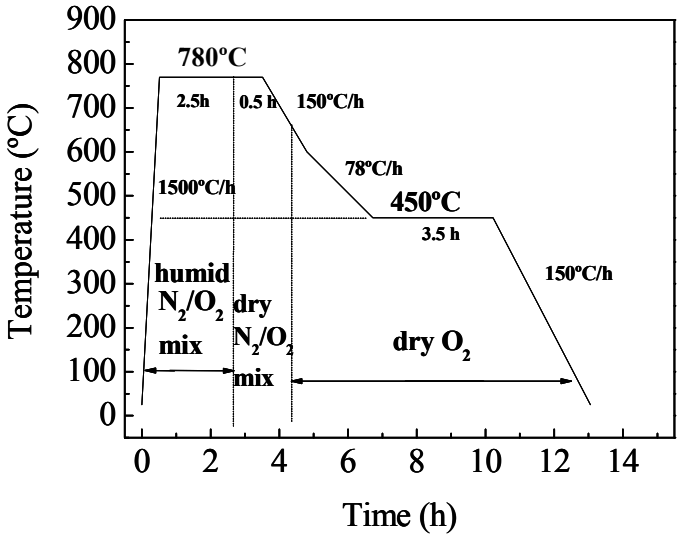

Fig. 6-12 Heating profile for the high-temperature anneal of TFA-YBCO on CeO_2/YSZ . Humidified gas is introduced at 100ºC. 0.02 kPa oxygen mixed gas is used in the firing profile with a maximum temperature of 780ºC. YBCO film is annealed below 500ºC to become YBCO superconductor.

XRD θ-2θ scans were performed systematically on all YBCO films. Typical θ-2θ scans are shown in Fig. 6-13. Qualitatively, no significant differences where observed among them. Main reflections detected in this scan are the (00*l*) from the YBCO and (*h*00) from CeO_2 and YSZ indicating a strong c-axis normal preferred orientation. $BaCeO_3$ (BCO) phase is also detected with two different orientations (100) and (110). This confirms chemical reactivity in the interface between YBCO and CeO_2 [198] and will be further supported by TEM analysis. Indeed, the presence of large amounts of $BaCeO_3$ in YBCO/CeO_2 interface has also been reported by other authors [39,199,200].

As a general trend for this system (YBCO/CeO_2/YSZ), we also detected $Ba_{1-x}Y_xF_{2+x}$ (BYF) and CuO phases. We remark that the most intense reflection of CuO have not been indexed in the θ-2θ scan due to it overlaps with (200)YSZ Bragg line reflection.

The presence of BYF, as we introduced in section 1.2.3.1.4.1 and also observed in MOD-perovskite system described in chapter 5, it is a clear indication that precursors have not been completely converted to YBCO film [71]. On the other hand, CuO appeared due to YBCO pathway conversion [71] and also due to the lack of Ba^{2+} for the formation of $BaCeO_3$ (BCO). Y_2O_3 phase is also expected to be present as a consequence of the interface reaction, however, its most intense reflections are also overlapped with other reflection peaks like (110) $BaCeO_3$.

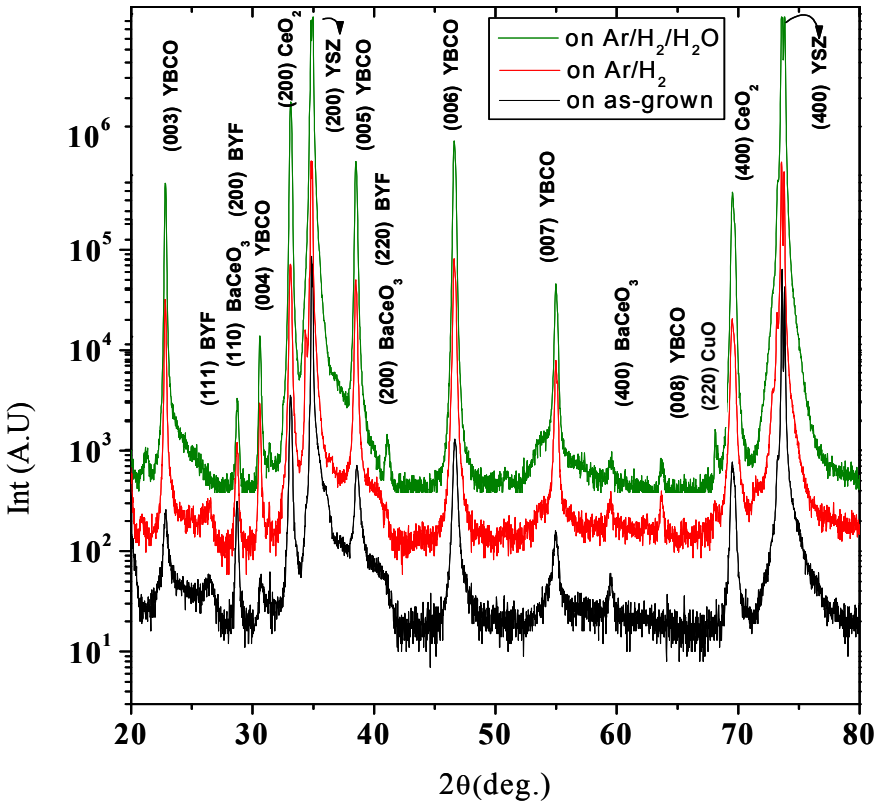

Fig. 6-13 XRD θ-2θ scan for 275 nm thick TFA- YBCO film growth on as received CeO_2/YSZ substrate (in black), on Ar/H_2 processed substrate (in red) and on Ar/H_2/H_2O processed substrate (in green).

For this system it is quite difficult to estimate the amount of $BaCeO_3$ formation from XRD data since 2θ values match with BYF reflections and (200) BCO peak could not be integrated because appeared as shoulder in (005) YBCO peak. However, recent work from Wesolowski and Cima describes an alternative method (destructive) based on ICP analysis (see

2.2.5) for $BaCeO_3$ quantification besides XRD texture analysis [201] which could be interesting to be used in future work.

In Table 6-II are listed the results of XRD texture analysis performed in the as- mentioned substrates.

Table 6-II Summary of XRD data of TFA-YBCO film grown on vacuum deposited CeO_2 buffered YSZ.

	$^{TFA}YBCO/^{sputt}CeO_2/YSZ$	
Cap layer Processing atmosphere	Δω(005) YBCO (º) (±0.1)	Δϕ(103) YBCO(º) ±(0.1)
As-grown	1.2	2.4
Ar/H,	1.3	1.9
$Ar/H_2/H_2O$	0.7	1.4

We detected that in YBCO film grown on $Ar/H_2/H_2O$ processed CeO_2/YSZ substrate, the overall texture and crystallinity have been improved. Out-of-plane and in-plane texture data for this sample (YBCO/($Ar/H_2/H_2O$)CeO_2/YSZ) are Δϕ (103) YBCO=1.4º and Δω (005) YBCO = 0.7º, as is shown in Fig. 6-14. Therefore, the degree of grain alignment and crystallinity of YBCO layer was improved by a factor two when CeO_2 surface displays atomically flat terraced surface. From this result two comments are in order. First, it remarks the special and important role of water on CeO_2 surface conditioning and on the other hand, we have the first indication that percentage of atomically flat area is the key parameter that controls the subsequent TFA-YBCO growth, rather than rms average roughness value.

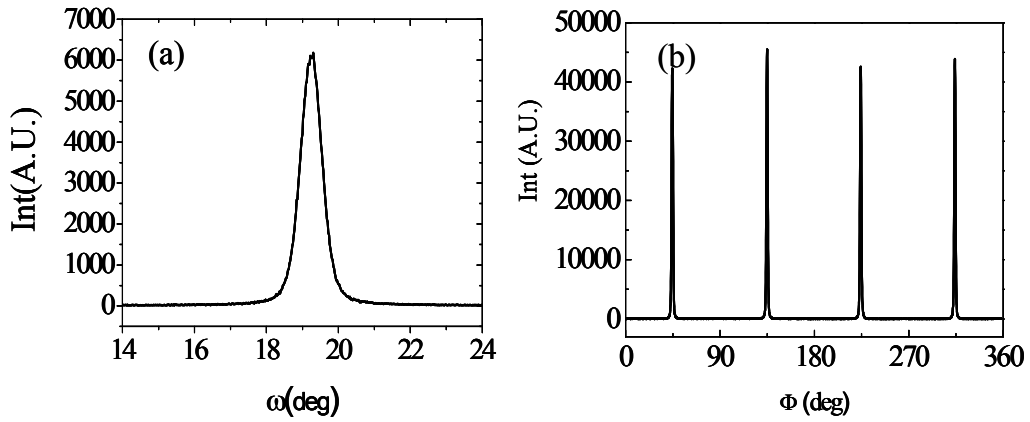

Fig. 6-14 (a) ω-scan taken through the (005) YBCO reflection, Δω= 0.7º (b) ϕ-scan taken through the (103) YBCO reflection, Δϕ= 1.4º, corresponding to the YBCO/CeO_2/YSZ where cap layer was processed under $Ar/H_2/H_2O$ atmosphere.

It is interesting to note that in-plane orientation of YBCO, retained the orientation of the buffer layer, $\Delta\phi$ (111) CeO_2 = 1.2º. The in-plane alignment for the c-axis growth is [100] YBCO|| [110] CeO_2. A 45º in-plane rotation of the orthorhombic YBCO with respect to the cubic CeO_2 achieving a lattice mismatch of 0.5 % (see Table 1-I).

Scanning electron microscopy (SEM) was used to analyse the surface morphology of the YBCO films. We have compared YBCO surface morphology of the film grown on as-received substrate, Fig. 6-15(a), with YBCO film grown on $Ar/H_2/H_2O$ processed CeO_2 cap layer, Fig. 6-15(b) since it displays the best film texture. In the YBCO surface of the first case, a number of regularly distributed cracks with some associated porosity can be observed. On the other hand, YBCO grown on $Ar/H_2/H_2O$ processed CeO_2, presented a very different film surface. This discloses a homogenous structure, a dense film, crack–free and with many $BaCuO_2$ particles on the surface [99]. We would like to remark that this phase has not been previously detected in XRD due to its most intense reflection matches with $BaCeO_3$ reflections. However, its nature was investigated by μ-Raman spectroscopy in preliminary studies of the group [121]. It is interesting to note that neither of them presents a-axis grains, contrasting with TFA-YBCO film on MOD-$SrTiO_3$ cap layer (chapter 5).

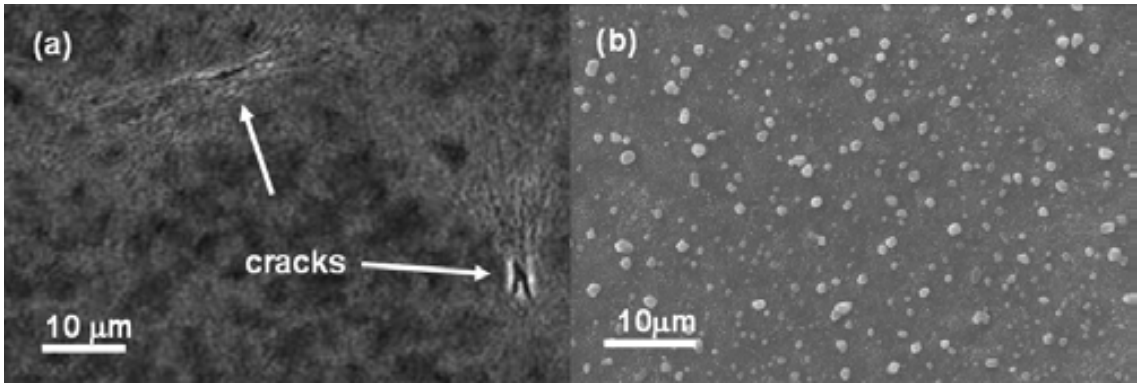

Fig. 6-15 SEM image of the TFA -YBCO layer grown on sputt-CeO_2 /YSZ substrate (a) as-grown and (b) processed in $Ar/H_2/H_2O$ atmosphere.

To confirm microstructural changes on YBCO layer caused by the texture and morphology of ceria cap layer, we have carried out TEM observations. All YBCO films have been examined in cross section. Fig. 6-16 showed complete c-axis orientation of YBCO films through-out the thickness. However, interfacial reaction has been also identified in some extent in all these samples here analysed. The reaction phase identified by EDX mapping is $BaCeO_3$ [117], being in well agreement with XRD data. Notice that for as-grown and Ar/H_2 processed CeO_2 cap layers see Fig. 6-16 (a,c), $BaCeO_3$ phase covers almost all CeO_2 film whereas for processed in $Ar/H_2/H_2O$ we have identified isolated $BaCeO_3$ particles, see Fig. 6-16 (b). Interestingly,

$Ar/H_2/H_2O$ processed CeO_2 cap layer displayed higher percentage of atomically flat area (84%) than the other two samples (46% for as-grown and 18% for Ar/H_2 processed).

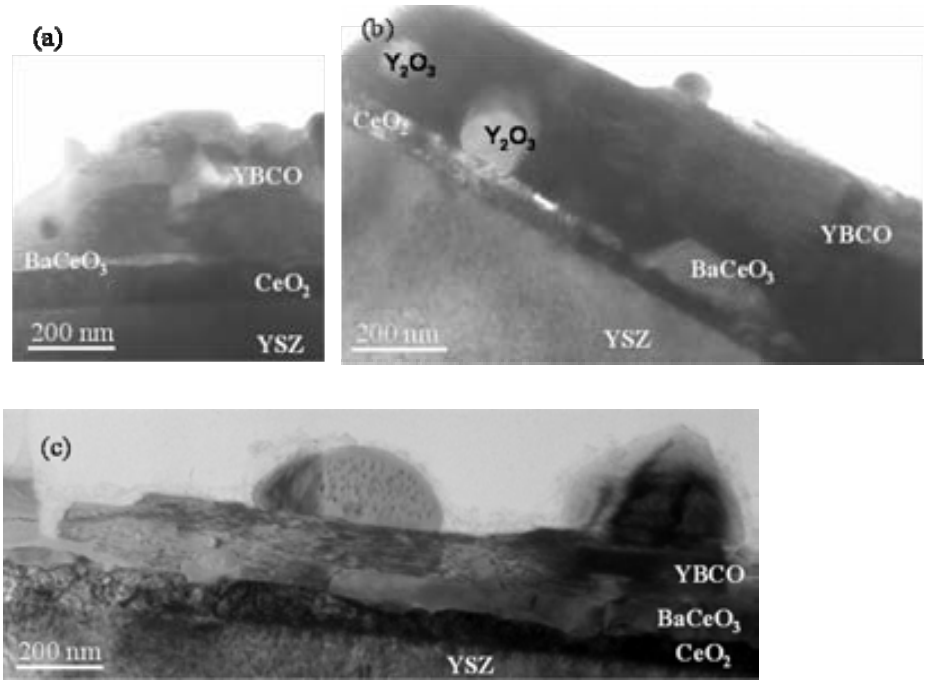

Fig. 6-16 Cross sectional TEM images of YBCO films derived from differently processed CeO_2/YSZ substrates (a) as-grown (b) processed in $Ar/H_2/H_2O$ and (c) processed in Ar/H_2 atmosphere.

For TFA-YBCO film grown on as-received CeO_2 cap layer, Fig. 6-16 (a), we have also detected local misalignment of the YBCO film, as can be seen in Fig. 6-17(a) and its diffraction pattern, Fig. 6-17 (b). Slashed line displays the as-mentioned local misalignment of YBCO (~14º). It is in that sample where we have observed by SEM (Fig. 6-15(a)) that some porosity and microcracks have been developed. It could be bound with mismatches between the $c_\perp$ and misaligned grains.

In TFA-YBCO film grown on $Ar/H_2/H_2O$ processed cap layer we have identified Y_2O_3 particles embedding the YBCO matrix attributed to interface reaction subproduct. The nature of hemispherical particles detected on YBCO surface in Fig. 6-16(b) and (c) could not be identified.

Although the mechanism for $BaCeO_3$ formation is not well established, the most reasonable proposal is that takes place a topotactic reaction between Ba^{2+} and CeO_2 [199,201]. Moreover, by considering the c-axis orientation of YBCO films throughout the film thickness we assume that YBCO film has been nucleated on CeO_2 surface and interface reaction occurs

after YBCO nucleation. In fact, lattice mismatch between YBCO and $BaCeO_3$ is much higher (ε= ~14%) than between YBCO and CeO_2 (ε= -0.52%) and YBCO film will not grow epitaxially on $BaCeO_3$ film. Therefore these findings suggested us that atomically flat area in CeO_2 might have a bigger role in determining the YBCO film quality than interfacial reaction. However, further exploration and discussion on this mechanism will be given in chapter 8.

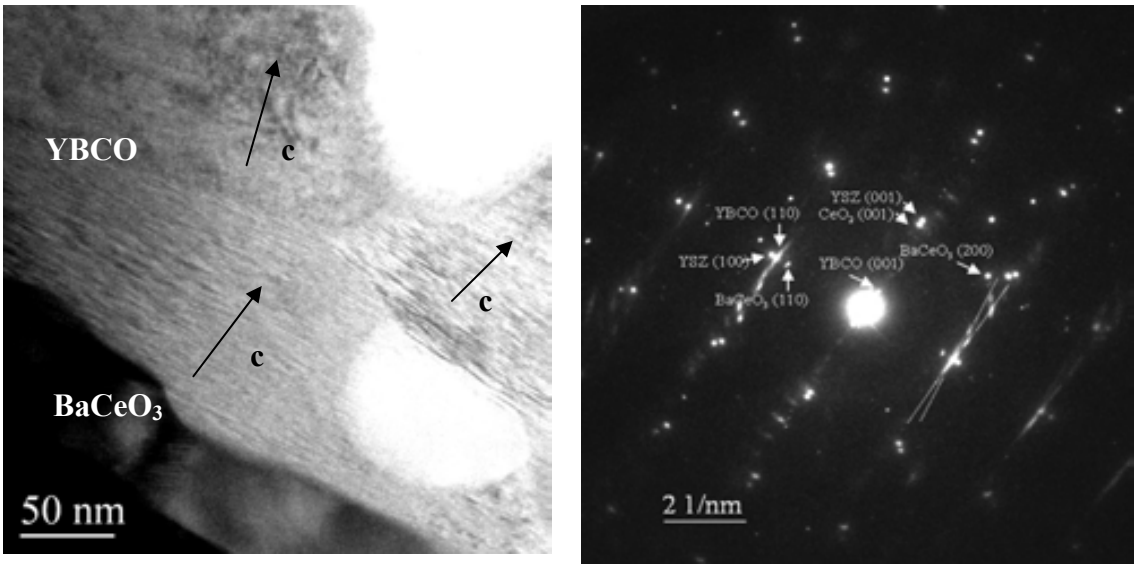

Fig. 6-17 (a) Low magnification cross-sectional TEM image viewed along the <100> direction of YBCO /as-grown CeO_2/YSZ showing the YBCO [010] // CeO_2 [110] // YSZ [110] orientation relationship.(b) Corresponding SAD pattern (selected area diffraction).

In conclusion, from the microstructural point of view we have appreciated that as-deposited or processed in Ar/H_2 samples (rough surface morphology governed by rounded grains) show higher interface reactivity and poor degree of YBCO film texture. It has been suggested that CeO_2 with rougher surface favours the accommodation of misoriented YBCO nuclei. Moreover, higher surface roughness involves higher surface-to-volume ratio and thus greater surface area exposed to YBCO film. Therefore it is hardly surprising that those films presented higher interface reactivity.

On the other hand, atomically flat (80%) and highly textured surface ceria enhance epitaxial YBCO growth and reduces the interface reactivity. Thus, microstructural characterization also supports the hypothesis that what really determines the TFA-YBCO epitaxial growth is high percentage of atomically flat area in CeO_2 cap layer, not the average roughness.

A possible reason for this experimental observation is that the internucleus spacing of YBCO on CeO_2 is surprisingly large, tens of μm. Taking into account that the distance between two terraces are smaller (~50 nm), it is not surprising that the bigger contribution to rms roughness, deep hillock, become negligible. These results are corroborated by recent work of Solovyov and coworkers[202] who studied the nucleation of YBCO on buffered metallic

substrates by the BaF_2 process. They also stress the strong dependence of YBCO nucleation on substrate material. In particular, they noted the difficulty of growing YBCO on vacuum-CeO_2 cap layer than $SrTiO_3$ substrate.

In summary, cap layer defects influence the growth of the YBCO film. It has been found that the growth of the YBCO film changes to accommodate these defects [203]. These changes may be reflected in a change in alignment, generation of structural defect in the YBCO film, or the occurrence of an interfacial reaction phase.

6.4.2 Superconducting and electrical properties

The superconducting properties of the YBCO layers grown on sputt-CeO_2 /YSZ substrate were measured inductively by SQUID. The influence of substrate quality can also be clearly detected through J_c measurements, shown in Fig. 6-18. We observe that the critical current density at 77K of YBCO film grown on $Ar/H_2/H_2O$ processed substrate is almost two times higher (J_c >1.5MA cm^{-2}) than the J_c at 77K of YBCO grown on processed in Ar/H_2 or as-grown CeO_2/YSZ sample (J_c (77K)<10^4 Acm^{-2}). Lower J_c values are correlated with higher interface raction an d with CeO2 cap layer displaying rougher and cracked surface morphology. However, based on TEM analysis we propose that the critical parameter to obtain high quality YBCO growth is the development of atomically flat area in CeO_2 cap layer and therefore, interface reaction does not preclude the attainment of highly epitaxial film.

We note that the observed critical currents in this multilayer systems are quite low in comparison to YBCO films grown by TFA in $LaAlO_3$ single crystal substrate (3MA/cm^2 at 77K) [34]. According to XRD investigations in which we detected intermediate phases, we suggest that it is necessary to improve YBCO film growth on CeO_2 cap layer. Actually, more recent investigations of the influence of growth conditions on the microstructure and final critical currents of TFA-YBCO films [99] suggest that modifying reaction kinetics of YBCO formation ($P(H_2O)$ and gas flow rate) or annealing time could lead to enhanced superconductor performances [99,88].

Since highest J_c and film quality has been observed for YBCO film grown on $Ar/H_2/H_2O$ processed substrate, electrical resistivity was measured for this film and compared to as-grown substrate. Results are displayed in Fig. 6-19. Even though both samples exhibit a sharp transition T=90K, a large difference exists in ρ(300K) and ρ(0K). In YBCO film grown on $Ar/H_2/H_2O$ processed substrate residual resistivity remains essentially zero and the room temperature resistivity around 300 μΩcm. By contrast, YBCO on as-grown substrate displays ρ(0)>100 μΩcm and ρ(300K) is enhanced to 800 μΩcm. Whereas the former results are typical of high quality, in-plane aligned YBCO film [128].The second reflects a film with poor

connectivity between grains and porosity [174]. Therefore, these results correlate well with texture and microstructural investigations presented earlier establishing a strong relationship between J_c, resistivity measurements and surface buffer layer quality.

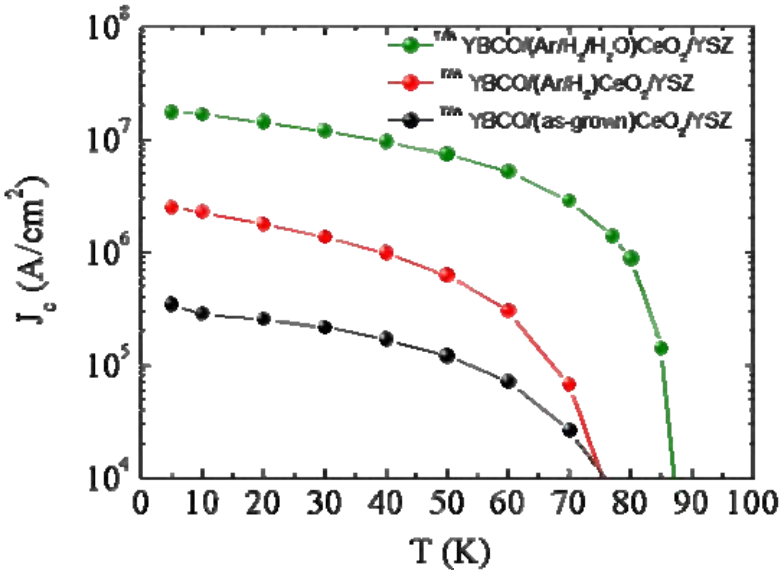

Fig. 6-18 Temperature dependence of J_c for TFA-YBCO multilayers have been obtained in as-grown (black trace), processed in Ar/H_2 (red trace) and processed in $Ar/H_2/H_2O$ atmosphere CeO_2 cap layer (green trace).

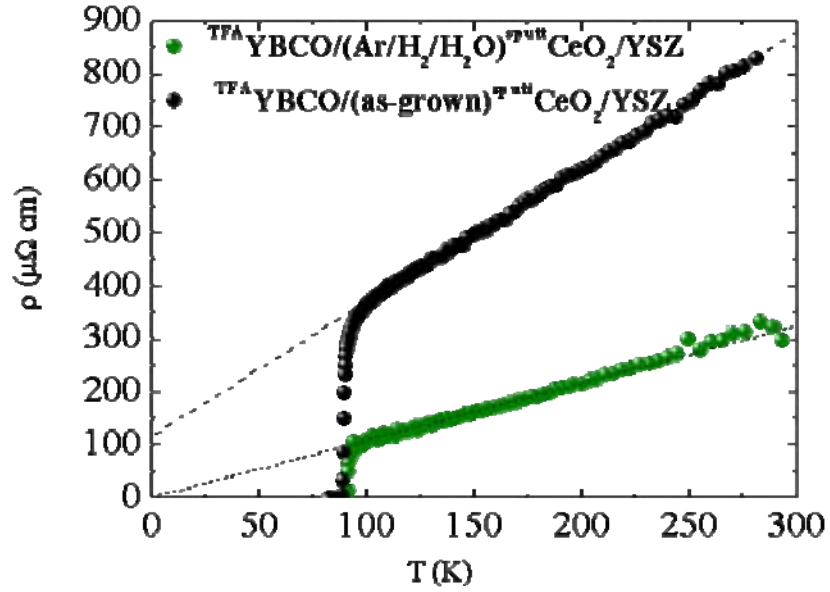

Fig. 6-19 Temperature dependence of the normal state resistivity of YBCO film grown on as-received CeO_2/YSZ substrate (in black), and on $Ar/H_2/H_2O$ processed CeO_2/YSZ substrate (in green).

In conclusion, we systematically studied the structural and superconducting properties of the YBCO thin film grown on the as-grown and annealed CeO_2 cap layers covering YSZ substrates. Our study shows a clear correlation between the crystalline quality and surface morphology of the CeO_2 cap layers with microstructure, texture and J_c in the superconducting YBCO thin films establishing atomically flat terraced surface as a controlling parameter for high quality YBCO growth.

We have shown that high critical current density >1.2 $MAcm^{-2}$ (77K) can be achieved in superconducting YBCO thin film grown by trifluoroacetate route on processed CeO_2/YSZ sample under $Ar/H_2/H_2O$ atmosphere. For this sample, XRD and TEM investigations showed YBCO high crystallinity, improved epitaxy and sharp interface between YBCO and CeO_2 with some $BaCeO_3$ particles. These excellent results were attributed to the special role of H_2O which favored highly textured and atomically flat (~80%) CeO_2 cap layer, as revealed XRD, RHEED and AFM analysis. On the contrary, a decrease of superconducting properties associated to poor epitaxy and high interface reactivity were obtained for YBCO films grown on as-grown or Ar/H_2 processed CeO_2/YSZ sample. In these cases, CeO_2 buffer layer presented granular and heterogeneous surface.

6.5 Metallic substrates

To confirm the viability of this new processing treatment in wet atmosphere, we have to transfer it on metallic substrates. The main routes to produce YBCO CCs are ion beam assisted deposition (IBAD) and rolling assisted biaxially textured substrates (RABiTS), as already commented in chapter 1. Here we describe processing surface conditioning of vacuum deposited CeO_2 cap layer and the results of YBCO deposition by TFA-MOD on two metallic substrates: (a) sputtering-CeO_2 / evaporated-YSZ / evaporated- CeO_2 /Ni, supplied by Cryoelectra and (b) PLD-CeO_2 /IBAD-YSZ / Stainless steel supplied by the University of Göttingen.

6.5.1 CeO_2/YSZ/CeO_2 /Ni architecture

This template was composed by nickel substrates with a purity of 99.95% and a thickness of 80 μm. Then metallic Ce was deposited from thermal evaporator in water vapor atmosphere resulting in the formation of CeO_2. As a second layer 600 nm of YSZ was grown by rf sputter. As the next step 75 nm of CeO_2 was deposited as a cap layer [182].

Tapes were cut into pieces of about 5 mm x 5 mm, and each piece was carefully cleaned in an ultrasonic bath with acetone and methanol to remove contaminations. A typical X-ray diffraction θ-2θ scan for this tape, as-received, is shown in Fig. 6-20 (a). It is interesting to note

that it is free of undesired secondary phases as NiO and (111) CeO_2 Bragg line reflection. Detailed XRD results from ϕ scan (shown in Fig. 6-20 (b)) revealed good in-plane epitaxial texturing, Δϕ(111) CeO_2 = 6.7-7.4º. It is remarkable that the intensity of the 4 peaks is not constant due to the rectangular geometry of nickel substrate and its inevitable curvature. On the other hand, ω-scan for (200) CeO_2 has a FWHM of ≈ 6.1º.

The tape was introduced into the furnace for processing under 95%Ar/5%H_2 in 2.2% of H_2O atmosphere (Ar/H_2/H_2O) following the heat treatment profile described in section 6.3.1 in order to study a possible improvement on CeO_2 film quality.

XRD analysis showed that annealed CeO_2 films retained the orientation of the as-deposited films. The FWHM of the ω–scan at the CeO_2 (200) reflection was 6.1º, the same as for the as-deposited film and FWHM of ϕ-scan of CeO_2 (111) refection was 6.2-7.2º.

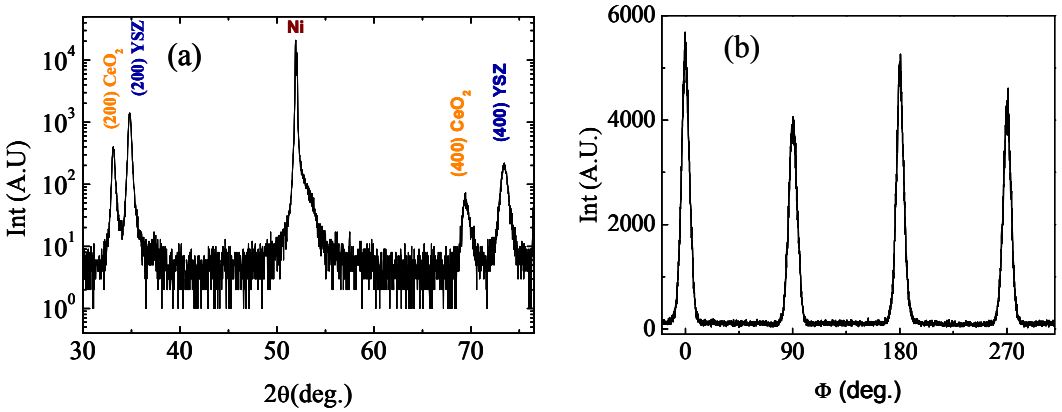

Fig. 6-20 (a) XRD θ-2θ scan for a 75 nm thick sputtered CeO_2 film on an e-beam YSZ and CeO_2-buffered Ni substrate. Both CeO_2 and YSZ films have a preferred c-axis orientation (b) In-plane-texture Δϕ(111) CeO_2 = 6.7-7.2º.

AFM analysis revealed a different surface structure for the as-grown and annealed in Ar/H_2/H_2O atmosphere CeO_2 cap layer. Whereas the substrate as-grown showed microcracks with some impurities, Fig. 6-21(a), processed ceria showed a homogeneous flat surface with no cracks, Fig. 6-21(b). This different topography is better understood if we carefully inspect the line profile performed in each AFM topographic image. Representative cross section analyses are shown at the bottom of Fig. 6-21. Looking at the as-grown substrate, Fig. 6-21 (a), smoother regions are delimited by ~ 50 nm deep microcracks. Note that the background of the profile scan is inclined due to the as-mentioned metallic substrate curvature. Ar/H_2/H_2O processed substrate shows no evidence of cracks but some outgrowths of 20 nm height are uniformly distributed on the surface (mosaic pattern). They can be appreciated in the inset of Fig. 6-21(b). Even though these small orthogonal platelets have been observed frequently when

CeO_2/YSZ/CeO_2/Ni substrate was processed in wet atmosphere, its nature could not be identified in the previous XRD analysis.

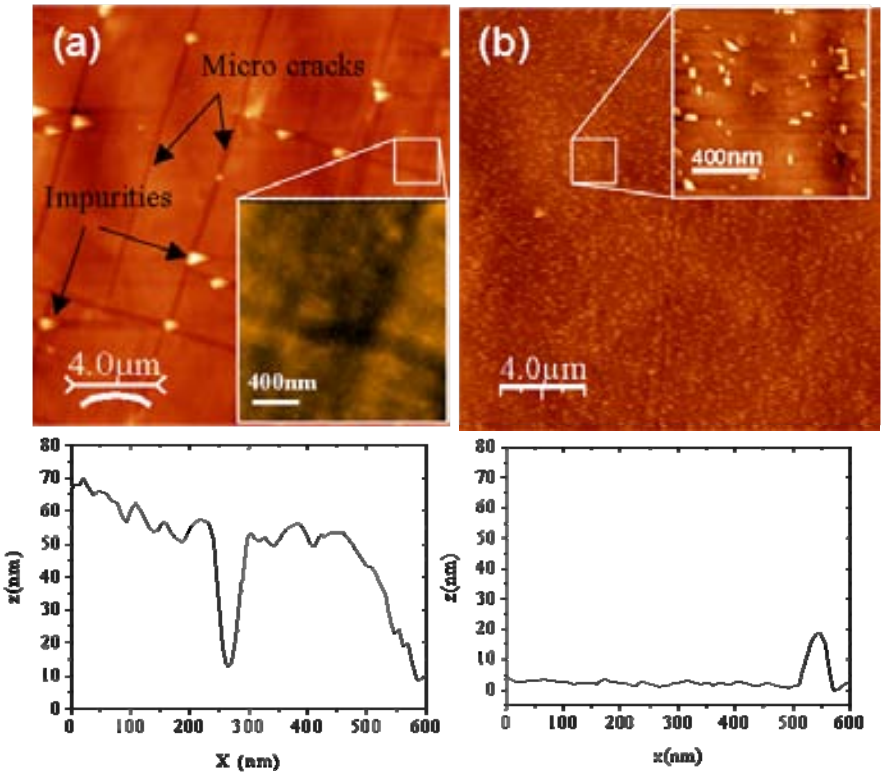

Fig. 6-21 AFM images obtained for CeO_2 /YSZ/CeO_2/Ni on (a) as-grown , rms= 3.7 nm and (b) annealed under Ar/H_2/H_2O atmosphere (rms= 3.6 nm). Profile scans have been performed on 2 x 2 µm scans, shown as inset.

Due to the fact that the metallic substrate is inclined, estimation of the atomically flat surface of large scans was not easy and it was carried out in 2 x2 µm scans, Fig. 6-22 (a-b). Even so, its curvature is clearly appreciated in binary images.

As grown CeO_2 film displays around 30% of atomically flat area and processed CeO_2 displays around 50%. Based on the results obtained in the previous section, orthogonal platelets have been subtracted from the final compute of atomically flat area (procedure described in 2.3). Finally, it is very interesting to remark that rms (average roughness) for as-grown and processed substrate are nearly the same, but atomically flat area has increased from ~30% to ~50% after processing CeO_2 template. In summary, Ar/H_2/H_2O processing atmosphere further enhance surface reconstruction, similarly to the experimental results obtained on CeO_2/YSZ model system but in this case, it has not developed terraced surface morphology.

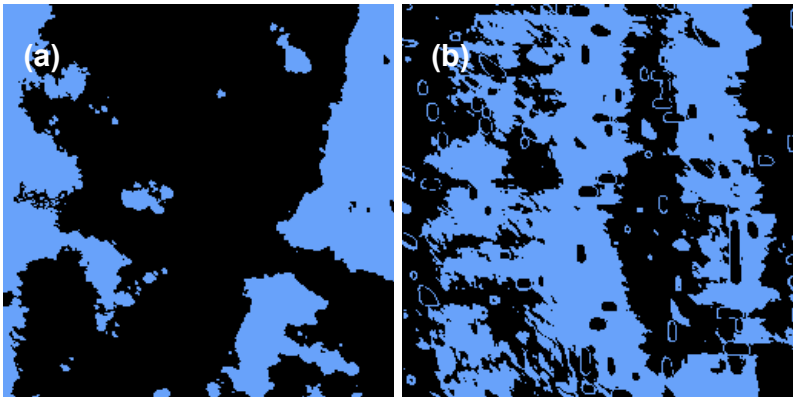

Fig. 6-22 Binary images of 2 x 2 μm scan of (a) as grown CeO_2/YSZ/CeO_2/Ni (b) Ar/H_2/H_2O processed CeO_2/YSZ/CeO_2/Ni substrate

6.5.2 TFA-YBCO on CeO_2/YSZ/CeO_2 /Ni architecture

6.5.2.1 Structural and morphological characterization

We proceeded to grow YBCO by the TFA route on top of annealed ceria cap layer. Deposition and growth conditions for YBCO are well described in section 3.1 and Fig. 6-12.

Comparison of X-ray diffraction pattern from the multilayer structure grown on as-deposited and on processed CeO_2/YSZ/CeO_2/Ni substrate is shown in Fig. 6-23. Similar patterns are obtained. The major peaks in the pattern correspond to the (00*l*) reflections of the superconducting oxide phase, indicating strong c-axis normal preferred orientations. The observations of the most intense Ba-Y-F reflection points out that intermediate phases are not fully converted to YBCO film [71]. High amount of NiO detected in θ-2θ scan indicates that during YBCO conversion, Ni has been partially oxidized. However, subsequent buffer layers (YSZ and CeO_2), blocked effectively further interdiffusion to upper layers and (00*l*) oriented has been retained.

$BaCeO_3$ phase is also detected in the θ-2θ scan confirming the reactivity between YBCO and CeO_2 cap layer like in CeO_2/YSZ model system. Further evidence for the convenient CeO_2 processing cap layer in Ar/H_2/H_2O atmosphere might be observed from YBCO texture analysis.

For the same YBCO film thickness (~275 nm), grown at the same conditions, Bragg line intensities of YBCO, CeO_2, YSZ and $BaCeO_3$ on metallic substrate have much less intensity than on YSZ single crystal. This is a clear indication that the quality of the film is poorer.

Δω(005) of YBCO film decreased from 5.1º on as-grown metallic substrate down to 4.5º for processed substrate. Δϕ (103) evolutes from [7.8-10]º to [7.6-9.2]º when YBCO was grown on

processed metallic substrate. We recall that on metallic tape we present two FWHM for ϕ-scan due to specimen geometry. In Fig. 6-24 it is shown ω-scan and ϕ-scan for the improved YBCO film. It is noticeable that in plane texture it is very similar to the underlying buffer layer (Δϕ CeO_2 ~6.2-7.2º). Consistent with low Bragg line intensities observed earlier in XRD θ-2θ scan, FWHM values on metallic substrate are higher than on single crystal. The principal reason for broader Δϕ and Δω values is the grain boundary network propagated from the Ni substrate into the YBCO film by the epitaxial growth [96]. This issue will be further discussed in section 6.5.2.2.

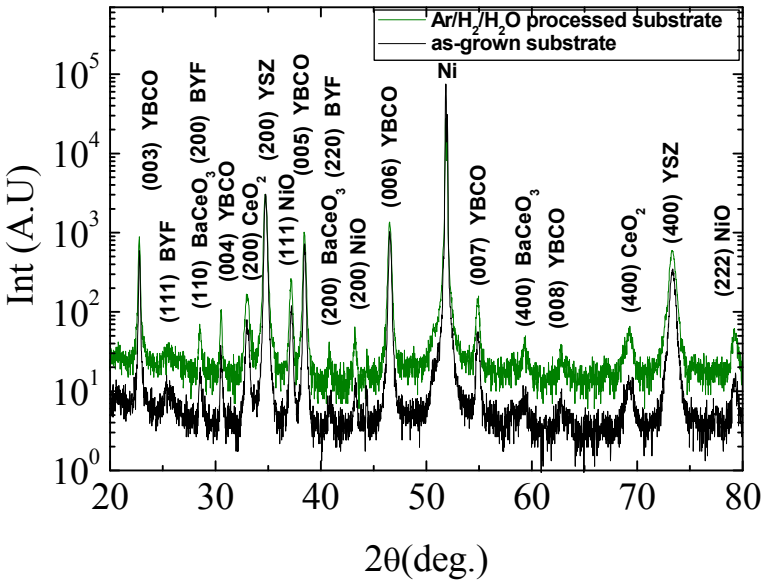

Fig. 6-23 XRD θ-2θ scans obtained for a 275 nm thick TFA-YBCO film on as-grown and processed in $Ar/H_2/H_2O$ atmosphere CeO_2 /YSZ/CeO_2/ Ni-RABiTS.

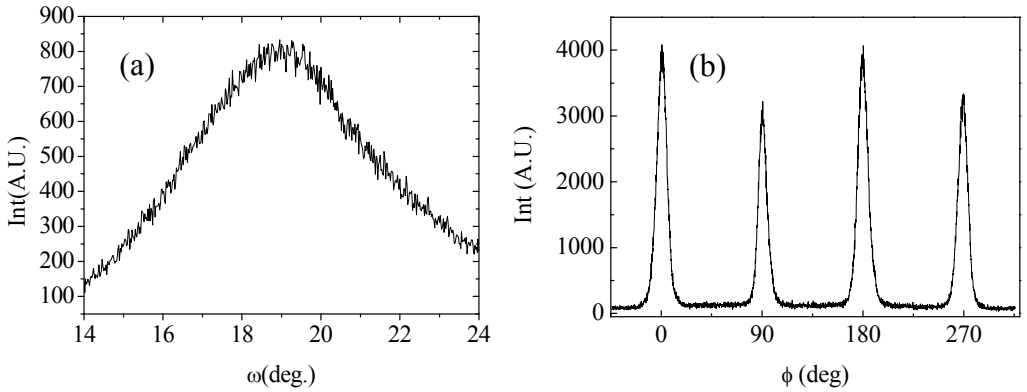

Fig. 6-24 Texture measurement for TFA-MOD YBCO on processed under wet atmosphere CeO_2/ YSZ/ CeO_2 /Ni substrate (a) Δω(005) YBCO = 4.5º, (b) Δϕ(103) YBCO = 7.6- 9.2º.

Surface morphologies of final films are shown in Fig. 6-25. YBCO film on as-grown substrate results in a surface with large density of porous and c-axis oriented microstructure, see Fig. 6-25 (a). YBCO film grown on $Ar/H_2/H_2O$ processed CeO_2 /YSZ substrate, exhibits a uniform and crack free morphology with some $BaCuO_2$ precipitates decorating the surface, Fig. 6-25 (b).

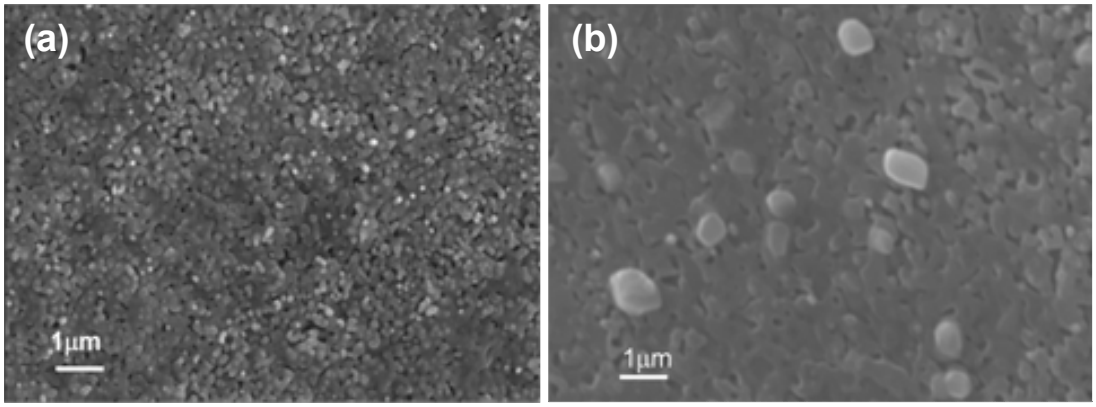

Fig. 6-25 SEM micrograph of a TFA-YBCO film grown on (a) as-recieved CeO_2/YSZ/CeO_2/Ni substrate (b) $Ar/H_2/H_2O$ processed CeO_2/YSZ/CeO_2/Ni substrate.

6.5.2.2 Superconducting and electrical properties

Due to the magnetic response from nickel is more intense than our superconducting film, it hinders data processing. Therefore, critical current density for these samples was measured at two isolated temperatures, 5K and 77K at which the magnetical signal from the substrate was subtracted following a complex procedure previously analyzed in the group [204]. YBCO film on as-grown substrate carried a J_c of only 2.8 x 10^4 A cm^{-2} at 5K and at 77K J_c fell down to 10^4 A cm^{-2}. Film grown on $Ar/H_2/H_2O$ processed substrate results in 2.6MA cm^{-2} at 5K and 0.3 MA cm^{-2} at 77K. Again, high percentage of atomically flat area of CeO_2 film correlates with a strong improvement in J_c values of YBCO films. This points out that, percentage of atomically flat area parameter is more appropriate to predict the surface quality of CeO_2/YSZ/CeO_2/Ni substrate in view of subsequently growth of TFA-YBCO film.

Comparing these J_c values with the ones we obtained on CeO_2/YSZ model system it is interesting to note that here we obtained lower J_c values which is well consistent with low intensity XRD 2θ Bragg line intensity.

It is well known that J_c values are strongly linked to grain boundaries in the YBCO film and therefore strongly linked to the YBCO in-plane texture. Based on the study of Dimos and coworkers [16] who correlated the in-plane alignment with critical current density, we plotted

J_c versus Δϕ(YBCO). To do that, in the same graph we included preliminary results from our group of TFA-YBCO grown on LAO single crystal [34] and bibliographic data in which YBCO film was grown by vacuum techniques (PLD [36], co-evaporation[88]) and by TFA route [205] on CeO_2 cap layer, see Fig. 6-26.

From this figure we observed that after processing ceria cap layer, the behavior of our samples, compared to YBCO films grown by TFA and related methods either on single crystal or CeO_2 cap layer, are consistent with Dimos prediction [16]. Taking into consideration our YBCO in-plane texture values, constraint by CeO_2 buffer layer texture, it is easily understood that YBCO on CeO_2/YSZ substrate leads higher J_c values than YBCO on CeO_2/YSZ/CeO_2/Ni because of YBCO in-plane texturing. Thus, to further improve J_c values, first the in-plane texture of YBCO film has to be improved which in turn strongly depends on the CeO_2 texture and texture of the underneath metal tape.

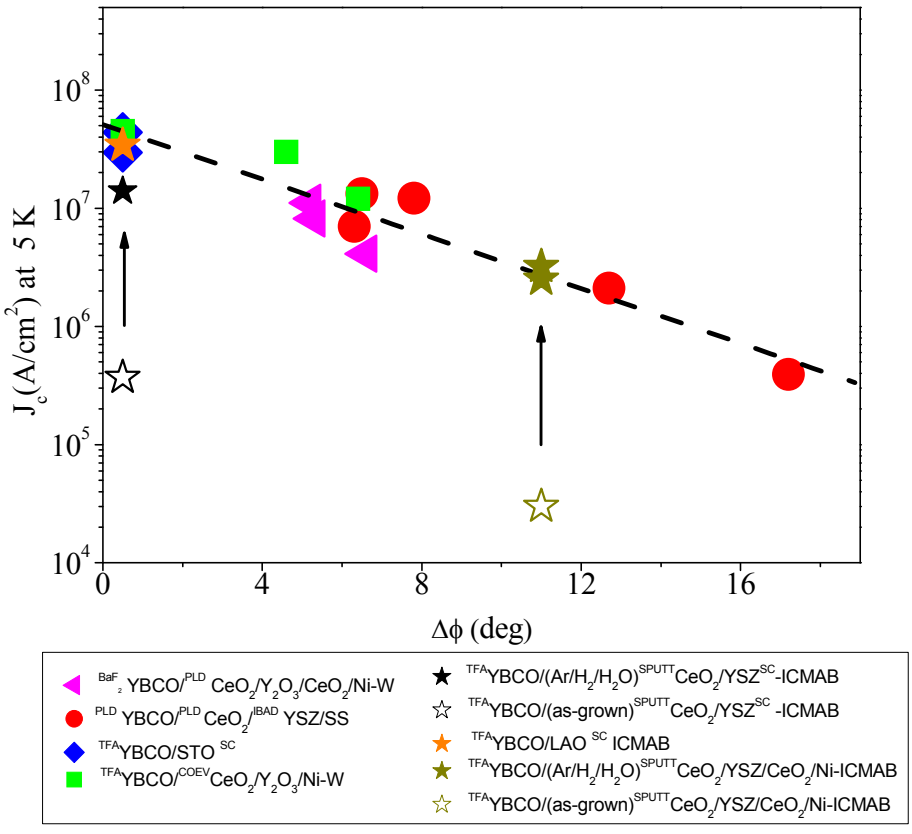

Fig. 6-26 J_c property dependence on FWHM Δϕ of YBCO (103) for several systems. : YBCO on LAO, on sputt-CeO_2/YSZ, on sputt-CeO_2/YSZ/CeO_2 /Ni and on PLD-CeO_2/IBAD-YSZ/SS.

On the other hand, the temperature dependence on electrical resistivity was also measured for YBCO grown on as-deposited and $Ar/H_2/H_2O$ processed $CeO_2/YSZ/CeO_2/Ni$ tape. Fig. 6-27 shows sharp transition and T_c= 90K for YBCO on processed substrate, indicative of an optimal state doping. By contrast, YBCO film on as-grown substrate shows a relatively broader transition and a slightly lower T_c. The temperature dependence of the electrical resistivity varies with the processing CeO_2 cap layer. Whether film grown on as-received $CeO_2/YSZ/CeO_2/Ni$ tape showed higher residual and room temperature resistivity, YBCO grown on processed $CeO_2/YSZ/CeO_2/Ni$ showed smooth surface characterized by a uniform, c-axis highly oriented microstructure [16,96]. Based on [174] this correlates well with SEM investigations which showed high porous density for YBCO on as-grown substrate and denser film for YBCO film on processed substrate.

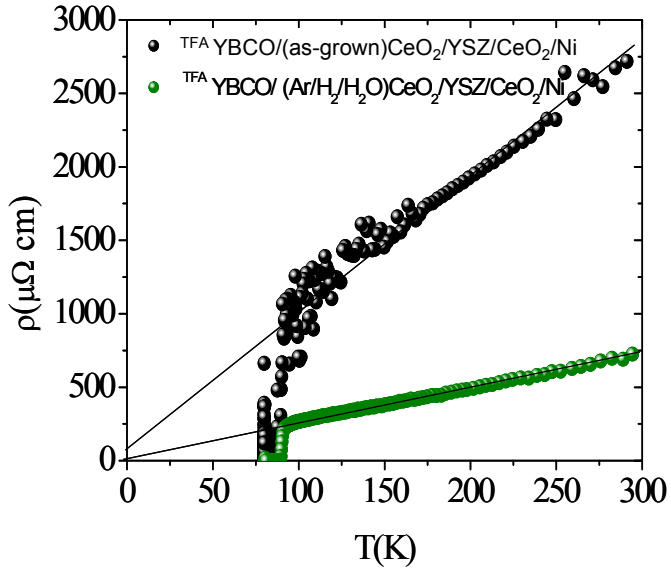

Fig. 6-27 Temperature dependence on the electrical resistivity for YBCO films grown on differently processed substrates. In black it is shown YBCO film on as-grown substrate and in green YBCO film on $Ar/H_2/H_2O$ processed substrate.

In conclusion, we successfully transferred optimal buffer layer conditioning of CeO_2 /YSZ model system to $CeO_2/YSZ/CeO_2/Ni$ substrate. The potentiality of this wet processing treatment to get high quality YBCO coated conductors has been confirmed for sputtering CeO_2 cap layer. We have suggested that it is due to the enhancement of atomically flat surface in CeO_2 cap layer. It is noteworthy that critical current density on Ni tapes has been reduced from YSZ single crystal substrate due to poor connectivity between grains (in-plane texturing) as we expected from the quasi-universal Dimos plot. It indicates that there is still room for further

improvement of YBCO film quality if we get better in-plane texture of both the underneath layers and consequently the YBCO film.

6.5.3 CeO_2/YSZ /SS architecture

We turn now to the second conductor architecture that has been widely considered as a candidate for the production of low cost coated conductors: YSZ deposited by IBAD on polycrystalline stainless steel (SS) substrate [206,36]. The biaxial texture of YSZ deposited by IBAD is fundamental to obtain an optimum template to deposit the YBCO superconductor film.

We should remind at this stage that for a certain number of applications a better mechanical strength of the conductor is a crucial requirement. It has been proved that polycrystalline SS substrates exhibit excellent mechanical responses to both axial stress and bending process [36].

Similarly to the previous systems, (CeO_2/YSZ and CeO_2/YSZ/CeO_2/Ni), with the purpose to enhance YBCO film quality, CeO_2 has been submitted to surface conditioning. However, since stainless steel substrate should not be oxidized under pure oxygen atmosphere we work under oxygen atmosphere because as we earlier observed (see section 6.3 and ([38])) oxygen atmosphere should be as good as $Ar/H_2/H_2O$ atmosphere. Therefore, we studied the influence of oxygen atmosphere on ceria surface quality.

CeO_2/YSZ/SS substrate was processed in pure O_2 atmosphere following the experimental procedure described in 6.3.1.

XRD θ-2θ scan of as-received and processed substrate are shown in Fig. 6-28. As-grown substrate, in black, exhibits (*h*00) reflections for the YSZ and CeO_2 and two peaks at 2θ = 43.68 and 49.38º. These reflections could be assigned to SS substrate. Furthermore, very weak off-axis (111) CeO_2 peak was also present, which is dramatic for the eptiaxial YBCO growth. Processing this film in oxygen we favored the elimination of (111) CeO_2 reflection. No other orientations or secondary phases are observed confirming that oxidizing atmosphere does not oxidize SS substrate. XRD texture for as-grown substrate are $\Delta\omega(200)CeO_2$ = 5.1 º and $\Delta\phi(111)$= 9.6º -7º. Processed CeO_2 substrate has FWHM value of $CeO_2(200)$ ω scan = 5.5 º and the average FWHM value for $CeO_2(111)$ ϕ scans is 9.1-6.6 º. Fig. 6-29 shows ω-scan and ϕ-scan for O_2 processed substrate. Note that no significant texture improvement has been occurred after processing CeO_2 /YSZ/SS substrate.

In this system, peak intensity of ϕ-scan is not constant due to the substrate geometry as previously observed for Ni tape. Moreover, both ω-scan and ϕ-scan are influenced by YSZ deposition by the IBAD technique because the incident ion bombardment comes into contact with the substrate in a preferential direction [139,36]

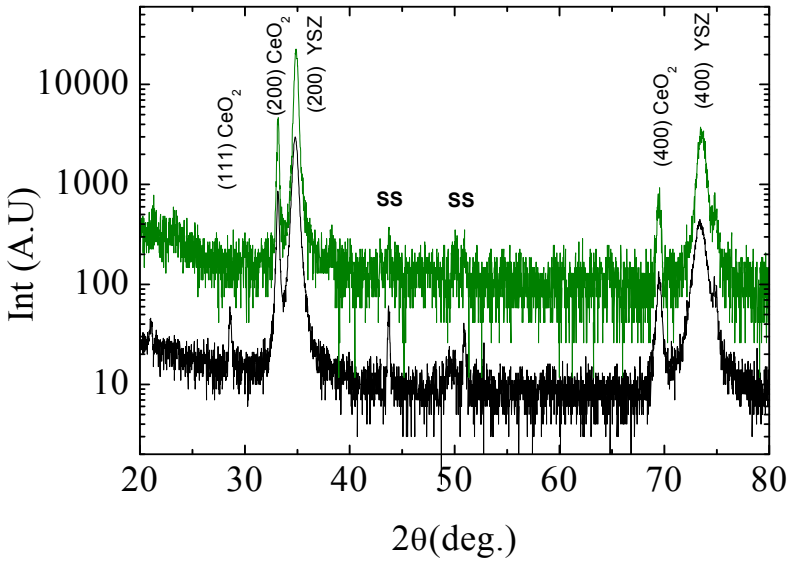

Fig. 6-28 XRD θ-2θ scan of a CeO_2 /YSZ/SS as received (in black) and processed under oxygen at 900ºC for 4 hours (in green).

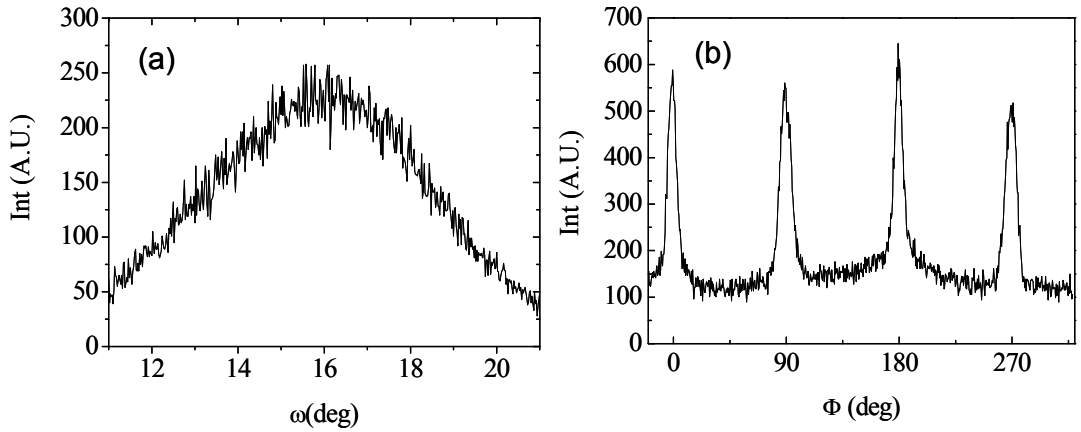

Fig. 6-29 XRD texture analysis of processed CeO_2/YSZ/SS substrate (a) ω-scan of (200) CeO_2 reflection with FWHM = 6.2º (b) Δϕ(111) CeO_2 =9-6.6º.

AFM topographic images and its corresponding profile scan of as-grown and processed under oxygen CeO_2 cap layer are shown in Fig. 6-30(a) and (b) respectively. As-grown ceria exhibits granular and heterogeneous topography with rms ≈ 7.6 nm. It is noticeable that no cracks are detected in comparison to as-grown CeO_2 on Ni substrate, Fig. 6-21. Therefore, this PLD-CeO_2 layer is favourable for long conductor fabrication from the viewpoint of prevention crack formation. On the other hand, oxygen processed ceria reveals a homogeneous and smoother surface, rms ≈ 5.2 nm .

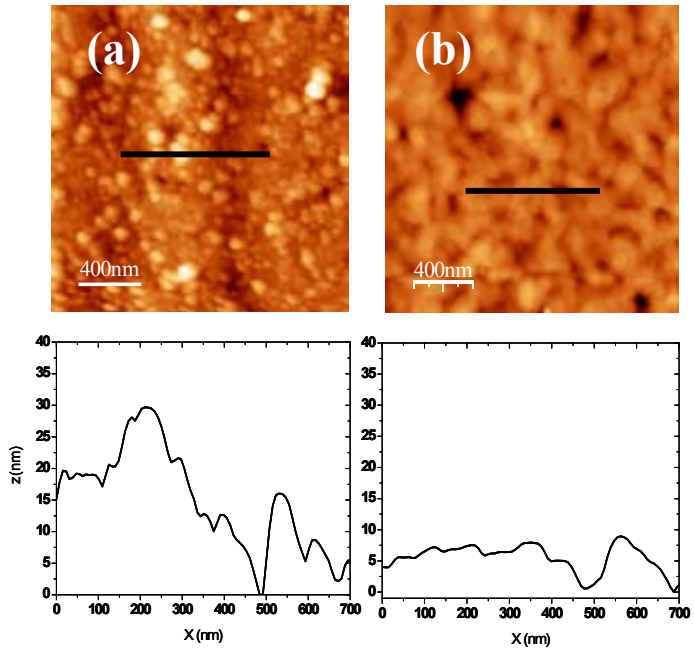

Fig. 6-30 AFM image of 2 x 2 μm of PLD-CeO_2 cap layer (a) as-grown with a rms :7.6 nm and (b) post processed under O_2 for 4 hours at 900ºC with a rms : 5.2 nm

Percentage of atomically flat surface has been calculated for these films. We obtained 12% of atomically flat area for as-grown substrate and 67% for processed substrate (see Fig. 6-31). In this case, after processing CeO_2/YSZ/SS substrate, atomically flat area has been increased more than a factor 3.

These results indicate that by processing PLD-CeO_2 film under pure oxygen atmosphere we have successfully improved its surface morphology. XRD analysis supports a film reconstruction since we detected that after thermal processing it has been eliminated the undesired (111) CeO_2 contribution.

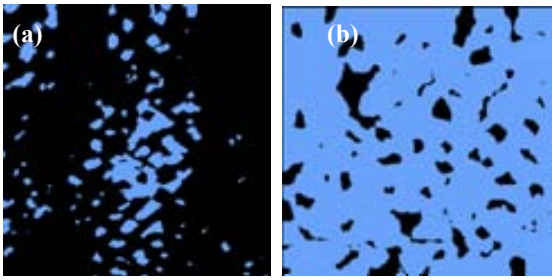

Fig. 6-31 Binary image (2x2μm) of CeO_2/YSZ/SS substrate (a) as grown (b) processed in O_2.

6.5.4 TFA-YBCO on CeO_2 /YSZ/SS architecture

The TFA-YBCO film was deposited on as-grown and processed in O_2 CeO_2/YSZ/SS substrate in the same growth conditions and heating profile as previous CeO_2 systems, Fig. 6-12.

On as-grown substrate resulted in a delamination of the superconducting layer. The main cause for the delamination is unknown at this time but stresses by different thermal expansion coefficients. Therefore we investigated the phase development for the YBCO film on processed substrate. XRD θ-2θ scan was performed, as is shown in Fig. 6-32. Only the (00*l*) YBCO reflections were observed. Peaks from substrate, buffer layer and reaction product such as the peak of (200) and (400) of YSZ and CeO_2 , and the peak of (110) $BaCeO_3$ were also observed. It is interesting to note that on PLD-CeO_2, YBCO has not reacted extensively with CeO_2 and only one orientation for $BaCeO_3$ was observed. Once more, it is noticeable overall low intensity of Bragg line intensity in XRD θ-2θ. This is an indication of poor degree of YBCO epitaxial fraction as we previously observed on CeO_2/YSZ/CeO_2/Ni substrates. Out of plane and in – plane texture of YBCO were further investigated by ω-scan and ϕ-scan. As shown in Fig. 6-33 the FWHM data for ω-scan of (005) YBCO = 3.3º and ϕ-scan of the (103) YBCO =7.5-12.5º.

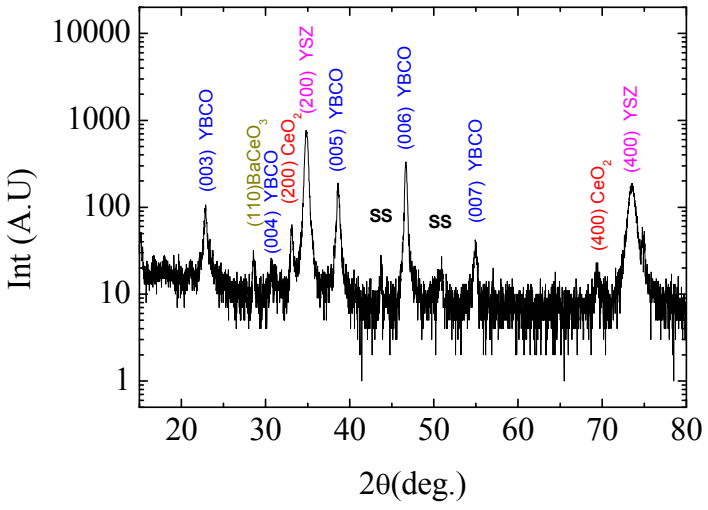

Fig. 6-32 XRD θ-2θ scan of 275 nm TFA-YBCO on processed CeO_2/YSZ/SS substrate.

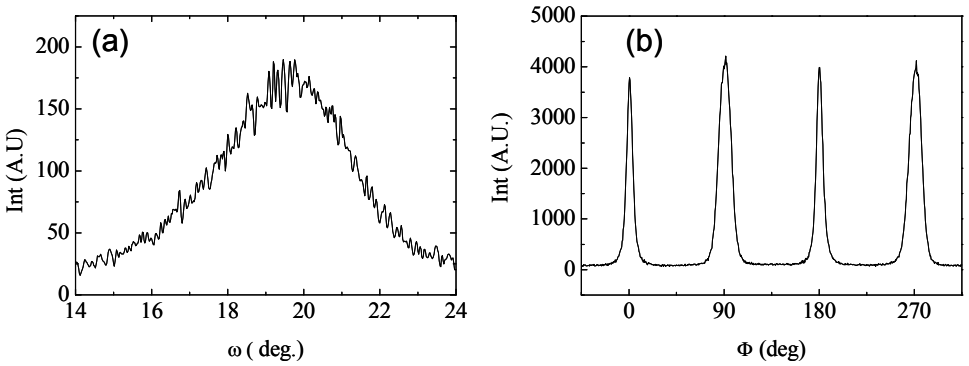

Fig. 6-33 ω- and ϕ-scans (CuKα) of YBCO grown on CeO_2 /YSZ/SS system deposited by TFA-MOD process (a) Δω(005) YBCO= 3.3º, (b) Δϕ(103) YBCO=7.5-12.5º.

Surface morphology of the YBCO films was studied by scanning electron microscopy (SEM). Fig. 6-34 reveals a homogeneous surface free of precipitates for the YBCO film.

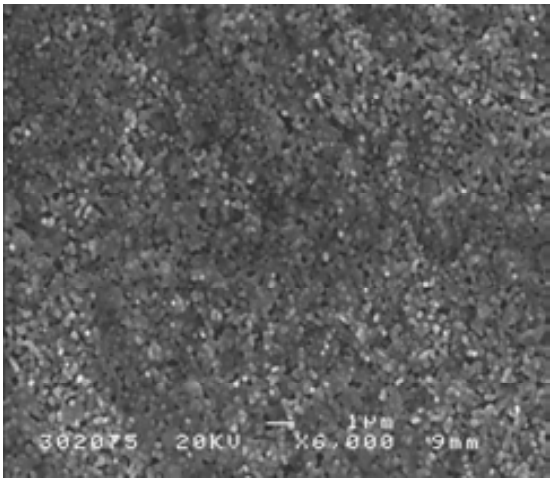

Fig. 6-34 SEM micrograph of TFA-YBCO film deposited on O_2 processed CeO_2/YSZ/SS.

Superconducting properties of processed YBCO sample at 5K and 77K was measured in a dc SQUID magnetometer. J_c (5K)= 2.5 M A cm^{-2} and J_c(77K) = 9.2×10^4 A cm^{-2}. Considering the correlation proposed by Dimos [16] (see Fig. 6-26), we find that SS substrate follows similar trend in J_c versus mosaic spread of the YBCO thin films. Our J_c value corresponds roughly well to that expected for the observed in-plane texture (Δϕ ~12º).

Temperature dependence of the normal state resistivity for YBCO deposited using TFA route on PLD-CeO_2/YSZ/SS sample shows that $\rho(0) \approx 150$ μΩcm and $\rho(300) \approx 600$ μΩcm, i.e. an anomalous high resistivity [99]. These results further support our SEM images which showed high density of porous and bad connectivity between grains .

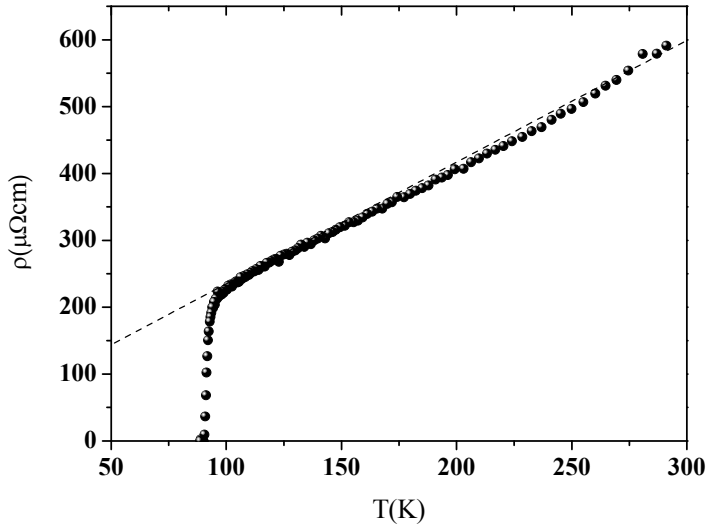

Fig. 6-35 Temperature dependence of the normal state resistivity of a TFA-YBCO deposited on O_2 processed CeO_2 (PLD)/YSZ-IBAD/SS

So we proved that TFA- YBCO can also grow epitaxially on oxygen annealed PLD-CeO_2/IBAD-YSZ/SS substrate leading to c-axis oriented superconducting layer. Processing substrate improves flat surface morphology leading to higher degree of homogeneity (67 % atomically flat). However, in this case to improve the superconducting properties of TFA-YBCO films, besides to enhance the flatness of the surfaces, it is strongly required to achieve good in-plane texturing of YBCO and thus also of the CeO_2 cap layer.

6.6 Conclusions

In this chapter we have analyzed the importance of controlling the interface quality between YBCO thin films deposited by the trifluoroacetate route and CeO_2 cap layer deposited by vacuum techniques (sputtering or pulsed laser deposition) to obtain high quality superconducting films.

As a first approach we have investigated the influence of thermal processing on sputtering-CeO_2 surface on YSZ single crystal substrate and then, optimal results have been transferred to

sputtering-CeO_2/coevaporated-YSZ/coevaporated-CeO_2/Ni and PLD-CeO_2/IBAD-YSZ/SS metallic substrates.

We have observed that CeO_2/YSZ single crystal substrate originally presents a surface morphology characterized by small rounded grains with some cracks and a partially reduced oxide at the surface (18% Ce^{3+}) attributed to deposition conditions. Thermal processing under Ar/H_2, $Ar/H_2/H_2O$ or O_2 atmospheres modify both chemical surface composition and surface morphology. AFM analysis revealed that $Ar/H_2/H_2O$ and O_2 processing atmospheres enhance the development of (001) atomically flat terraces (80% of flat surface area) whereas Ar/H_2 atmosphere leads to rough and heterogeneous surface (18% grains atomically flat). We have proposed that O_2 and $Ar/H_2/H_2O$ atmospheres enhance CeO_2 mobility but they follow different mechanism to reconstruct the initial CeO_2 surface morphology. It is likely that in $Ar/H_2/H_2O$ atmosphere hydroxyls group plays a special role in stabilizing the (001)-polar CeO_2 surface.

XPS investigations indicated that CeO_2 surface has been fully oxidized in all cases, and we have not detected any distinct feature on the chemical composition between these treatments due to samples exposition to air after thermal processing,

We have successfully deposited TFA-YBCO on the referred cap layers obtaining good structural ($\Delta\phi$(103)YBCO = 1.4º and $\Delta\omega$(005)YBCO=0.7º) and superconducting properties (J_c(5K)=20 $MAcm^{-2}$) when cap layer has been processed under $Ar/H_2/H_2O$ atmosphere. On the contrary, we have found that TFA-YBCO film quality deposited on as-grown and Ar/H_2 processed cap layers has been strongly degraded and additionally we have identified by TEM analysis higher interfacial reaction, i.e., $BaCeO_3$ formation.

Even further exploration is required we propose that interface reaction did not preclude the attainment of high quality YBCO film because it occur after the nucleation of the YBCO film. We propose that other factors (percentage of atomically flat area) have stronger influence on the epitaxial growth of YBCO film. In addition, it appears that rms roughness parameter is not useful to evaluate the atomically flat area when cap layer surface morphology presents artifacts like outgrowth, voids or hillocks. In these cases, we have found that the percentage of atomically flat area is the optimal parameter since allows us to exclude these contributions.

We have transferred wet processing atmosphere on CeO_2/YSZ/CeO_2/Ni architecture and we have also observed a very high atomic surface mobility, inducing a flat morphology for the CeO_2 surface (50% of atomically flat area versus 30% of as-received substrate). This interface evolution appears as a very promising processing treatment allowing the growth of high-quality TFA-YBCO layer with high superconducting performances. Indeed, we have demonstrated that TFA-YBCO film can epitaxially grow on this processed metallic template but both grain alignment and superconducting properties have been strongly reduced (~2 MA cm^{-2} at 5K) in comparison to CeO_2/YSZ single crystal substrate. This difference has been attributed to the poor connectivity between YBCO grains ($\Delta\phi$(103)YBCO=7.6-9.2º) induced by CeO_2 texture

which in turn depends on the metal. Therefore, in order that TFA-YBCO/CeO_2/YSZ/CeO_2/Ni could be used as feasible architectures for coated conductors, it is strongly required the improvement of in-plane alignment of the underneath layers.

By processing PLD-CeO_2/IBAD-YSZ/SS substrate under pure oxygen atmosphere we have promoted the mobility in CeO_2 films resulting an epitaxial film with smoother surface. TFA-YBCO film can effectively grow on this processed substrate contrasting with on non-processed in which YBCO delaminates. J_c values at 5 K are around 2.5MA cm^{-2} as we expected from the in-plane grain alignment ($\Delta\phi$(103)YBCO= 7.5-12.5º). In this case, similarly to Ni substrate, the room of TFA-YBCO improvement is strongly constraint by the quality of the substrate (grain alignment and surface morphology).

We may conclude, then, that the development of high-quality, flat interfaces should constitute an essential practice for the preparation of all-chemical coated conductors constraint by the in-plane alignment of the underneath layers being stressed for metallic substrates. Nevertheless, the selection of the optimum growth and processing thermal treatments will actually be conditioned to the stability of the metallic substrate under oxidizing atmospheres and hence the optimum process differed for each substrate.